cGMP Imaging Uncovers New Roles and Therapeutic Implications of NO/cGMP Signaling in the Kidney and in Melanoma

Dissertation

der Mathematisch-Naturwissenschaftlichen Fakultät

der Eberhard Karls Universität Tübingen

zur Erlangung des Grades eines

Doktors der Naturwissenschaften

(Dr. rer. nat.)

vorgelegt von

Daniel Stehle

aus Balingen

Tübingen

2022

Gedruckt mit Genehmigung der Mathematisch-Naturwissenschaftlichen Fakultät der Eberhard Karls Universität Tübingen.

Tag der mündlichen Qualifikation:	22.06.2022
Dekan:	Prof. Dr. Thilo Stehle
1. Berichterstatter:	Prof. Dr. Robert Feil
2. Berichterstatter:	PD Dr. Hannes Schmidt
3. Berichterstatter:	Prof. Dr. Moritz Bünemann

Zusammenfassung

Die Biosynthese von zyklischem Guanosinmonophosphat (cGMP) durch die NO-sensitive Guanylylzyklase (NO-GC) ist in die Regulation vieler physiologischer Prozesse involviert. Daher ist es nicht weiter verwunderlich, dass sich die pharmakologische Modulation des NO/NO-GC/cGMP-Signalwegs als Möglichkeit etabliert hat, verschiedene Krankheiten wie Herzinsuffizienz und Bluthochdruck zu behandeln. In einigen dieser Krankheiten zählen oxidativer Stress und eine verringerte NO-Bioverfügbarkeit zu den pathophysiologischen Merkmalen. Sogenannte NO-GC-*Stimulatoren* stimulieren die NO-GC synergistisch mit NO, wodurch die cGMP-Bildung trotz verringerter NO-Bioverfügbarkeit aufrechterhalten werden kann. Oxidativer Stress kann jedoch zur Oxidation des Häm-Kofaktors der NO-GC führen, was im Folgenden eine Stimulation durch NO verhindert. Die sogenannten NO-GC-*Aktivatoren* aktivieren spezifisch diese Häm-oxidierte NO-GC. Das Ziel dieser Studie war, die Funktion des NO-GC/cGMP-Signalwegs in der Niere und im Melanom zu untersuchen und herauszufinden, wie NO-GC in diesen Geweben als Angriffspunkt für Therapien genutzt werden könnte.

Dazu wurde cGMP in lebenden Zellen und Gewebeschnitten mithilfe eines Förster-/Fluoreszenz-Resonanzenergietransfer (FRET)-basierten cGMP-Biosensors in Echtzeit sichtbar gemacht. Zum ersten Mal konnten cGMP-Signale hervorgerufen durch NO, die NO-GC-Stimulatoren Riociguat und BAY 41-2272, sowie den NO-GC-Aktivator BAY-543 in der Niere und im Melanom mit hoher räumlicher und zeitlicher Auflösung untersucht werden. In diesem Zusammenhang wurde bestimmt, in welchen anatomischen Strukturen und unter welchen Bedingungen diese Substanzen wirksam sind. Die Ergebnisse dieser hochmodernen cGMP-Bildgebung wurden mit klassischen immunhistologischen Färbungen sowie Western Blots validiert. Weiterhin wurde das Tumorwachstum in gewebespezifischen NO-GC-Knockout-Mäusen verfolgt, um die pathophysiologische Relevanz des NO-GC/cGMP-Signalwegs im Melanom zu untersuchen.

NO führte zur Erhöhung der cGMP-Konzentration in den Glomeruli von Nierenschnitten *ex vivo*. Der NO-GC-Stimulator verstärkte diese NO-induzierte cGMP-Biosynthese. Nach Oxidation der NO-GC durch den Inhibitor ODQ konnten NO und der NO-GC-Stimulator keine cGMP-Bildung mehr hervorrufen, während der NO-GC-Aktivator die glomeruläre cGMP-Konzentration stark erhöhte. In Zusammenarbeit mit spezialisierten Laboren konnte gezeigt werden, dass diese Effekte von NO-GC-Aktivatoren in der Niere mit der Dilatation von glomerulären Arteriolen sowie einer Verbesserung des Blutflusses in der Niere einhergehen. Im Melanom wurde NO-induzierte cGMP-Bildung ausschließlich in perivaskulären Zellen – vermutlich Perizyten – des Tumorstromas beobachtet. Der NO-GC-Stimulator verstärkte diese NO-induzierte cGMP-Biosynthese in den Perizyten der Tumorgefäße, ganz ähnlich zu seiner Wirkung in der Niere. Bemerkenswerterweise war in männlichen Mäusen mit Cre/loxP-vermitteltem NO-GC-Knockout in den Perizyten der Tumorgefäße das Tumorwachstum stark verringert, vermutlich bedingt durch eine schlechtere Durchblutung der Tumoren.

Insgesamt wurde gezeigt, dass die NO-GC in der Niere und im Melanom ein wichtiger Regulator von (patho-)physiologisch relevanten Prozessen ist. In beiden Geweben verstärkten NO-GC-Stimulatoren die NO-induzierte cGMP-Biosynthese. NO-GC-Aktivatoren hingegen hatten keine Effekte unter basalen Bedingungen, riefen aber in der Gegenwart von ODQ cGMP-Bildung in den renalen Glomeruli hervor. Diese Ergebnisse stützten die gegenwärtige Hypothese, dass die Wirkstoffklasse der NO-GC-Modulatoren für die Behandlung von Krankheiten mit fehlreguliertem NO/NO-GC/cGMP-Signalweg geeignet ist.

Summary

Generation of cyclic guanosine monophosphate (cGMP) via nitric oxide (NO)-sensitive guanylyl cyclase (NO-GC) has been implicated in the regulation of many physiological processes. Therefore, it is not surprising that pharmacological modulation of the NO/NO-GC/cGMP pathway has been proposed for treatment of several diseases like heart failure and hypertension. The pathophysiological conditions in some of these diseases involve increased oxidative stress and decreased NO bioavailability. Pharmacological NO-GC *stimulators* counteract decreased NO bioavailability, as they can stimulate NO-GC synergistically with NO. Oxidative stress, however, might lead to oxidation of NO-GC's heme cofactor, making it unresponsive to NO. NO-GC *activators* specifically activate this heme-oxidized NO-GC. The present study aimed to identify the role of the NO-GC/cGMP signaling pathway in the kidney and in melanoma, and to explore how NO-GC could be utilized as drug target in these tissues.

To address these questions, cGMP was visualized in real time in live cells and tissues using a Förster/fluorescence resonance energy transfer (FRET)-based cGMP biosensor. For the first time, the spatiotemporal dynamics of cGMP signals induced by NO, the NO-GC stimulators riociguat and BAY 41-2272, as well as the NO-GC activator BAY-543 were analyzed in the kidney and in melanoma. Thereby, it was determined in which anatomical structures and under which conditions these drugs exert their effects. The cGMP imaging results were validated with classical immunostaining of tissue sections and Western Blot. Furthermore, the pathophysiological relevance of the NO-GC/cGMP signaling pathway in melanoma was investigated by analyzing the *in vivo* tumor growth in tissue-specific NO-GC knock-out mice.

NO increased the glomerular cGMP levels in kidney slices *ex vivo*. NO-GC stimulator potentiated this NO-induced cGMP generation. After ODQ-mediated NO-GC oxidation, however, NO as well as NO-GC stimulator were no longer able to induce cGMP generation, whilst NO-GC activator strongly increased glomerular cGMP levels. In collaboration with specialized labs, these renal effects of NO-GC activator were shown to correlate with dilation of glomerular arterioles and improved blood flow in the kidney. In primary melanoma, NO-induced cGMP generation was selectively detected in

perivascular cells of the tumor stroma, most likely pericytes. NO-GC stimulator potentiated the NO-induced cGMP generation in these tumor pericytes, similar to its effect in the murine kidney. Remarkably, Cre/loxP-mediated NO-GC knock-out in the tumor pericytes resulted in reduced tumor growth in male mice, probably via an impaired tumor perfusion.

Taken together, in the murine kidney and in melanoma, NO-GC was found to be involved in (patho-)physiologically relevant processes. In both tissues, NO-GC stimulators potently increased the NO-induced cGMP generation in the vasculature. NO-GC activators were ineffective under basal conditions but induced robust cGMP generation in renal glomeruli in the presence of ODQ. These results supported the hypothesis that the growing line-up of NO-GC modulators can be utilized for the treatment of diseases involving dysregulated NO/NO-GC/cGMP signaling.

Table of contents

List of abbreviations

ABC	avidin-biotin complex
ANP	atrial/A-type natriuretic peptide
APS	ammonium persulfate
AUC	area under the curve
BNP	brain/B-type natriuretic peptide
BSA	bovine serum albumin
CAG	cytomegalovirus early enhancer/chicken β-actin/β-globin
cAMP	cyclic adenosine monophosphate
Cat-#	catalog number
CCD	charge-coupled device
CFP	enhanced cyan fluorescent protein
cGi500	cGMP indicator with an EC_{50} of 500 nM
cGK	cGMP-dependent protein kinase (see also PKG)
cGMP	cyclic guanosine monophosphate
CIH	chromogenic immunohistochemistry
CKD	chronic kidney disease
CMOS	complementary metal-oxide-semiconductor
CMV	cytomegalovirus
CNG channel	cyclic nucleotide-gated ion channel
CNP	C-type natriuretic peptide
Cre	cyclization recombination
CTLA-4	cytotoxic T-lymphocyte-associated protein 4
DAB	3,3’-diaminobenzidine
DEA/NO	diethylamine NONOate
DMEM	Dulbecco’s modified eagle’s medium
DMF	dimethylformamide
DMSO	dimethyl sulfoxide
DNA	deoxyribonucleic acid
ECL	enhanced chemiluminescence
ECM	extracellular matrix
EDTA	ethylenediaminetetraacetic acid
EM-CCD	electron-multiplying charge-coupled device
eNOS	endothelial nitric oxide synthase
ER	estrogen receptor
FBS	fetal bovine serum
flox/floxed/fl	flanked by loxP sites
FPLC	fast protein liquid chromatography
FRET	Förster/fluorescence resonance energy transfer
GC	guanylyl cyclase
GFR	glomerular filtration rate
HEPES	4-(2-hydroxyethyl)-1-piperazineethanesulfonic acid
IB	imaging buffer
ICB	immune checkpoint blockade
IF	immunofluorescence
iNOS	inducible nitric oxide synthase

ko	knock-out
L-NAME	N(G)-nitro-L-arginine methyl ester
loxP	locus of X-over P1
MAPK	mitogen-activated protein kinase
mT	membrane-targeted tandem dimer (td)Tomato
nNOS	neuronal nitric oxide synthase
NO	nitric oxide
NO-GC	NO-sensitive guanylyl cyclase (see also sGC)
NOS	nitric oxide synthase
NP	natriuretic peptide
NPR	natriuretic peptide receptor (see also GC)
ODQ	1H-[1,2,4]oxadiazolo[4,3-a]quinoxalin-1-one
PBS	phosphate-buffered saline
PCR	polymerase chain reaction
PD-1/PD-L1	programmed cell death protein 1 and its ligand
PDE	phosphodiesterase
PFA	paraformaldehyde
pGC	particulate guanylyl cyclase
PKG	protein kinase G (see also cGK)
PMSF	phenylmethyl-sulfonyl fluoride
R (cGMP)	CFP/YFP ratio (representing cGMP concentration)
RAAS	renin-angiotensin-aldosterone system
RBB	ringer bicarbonate buffer
rcf	relative centrifugal force
RFP	red fluorescent protein
ROS	reactive oxygen species
RPMI	Roswell park memorial institute
SDS	sodium dodecyl sulfate
sGC	soluble guanylyl cyclase (see also NO-GC)
SGLT2i	sodium-glucose-cotransporter 2 inhibitor
SMA	α-smooth muscle actin
TAE	Tris-acetate-EDTA buffer
TAM	tumor-associated macrophage
TBE	Tris-borate-EDTA buffer
TBS	Tris-buffered saline
$T_{d/a/e}$	temperatures of denaturation, annealing and extension cycles
TEMED	tetramethylethylenediamine
tg	transgenic
UV	ultraviolet
VEGF	vascular endothelial growth factor
VSMC	vascular smooth muscle cell
X-Gal	5-bromo-4-chloro-3-indolyl-β-D-galactopyranoside
YFP	enhanced yellow fluorescent protein

1 Introduction

1.1 The cGMP signaling pathway

Cyclic guanosine monophosphate (cGMP) is a second messenger central to many physiological processes (**Figure I1**) (reviewed by Hofmann, 2020). For example, cGMP induces vascular smooth muscle cell (VSMC) relaxation and thereby controls the vascular tone (reviewed by Lincoln et al., 2001), and it can modulate phenotypic characteristics and enhance growth and survival of several cell types including VSMCs (Weinmeister et al., 2008; Wolfsgruber et al., 2003) and melanoma cells (Arozarena et al., 2011; Dhayade et al., 2016).

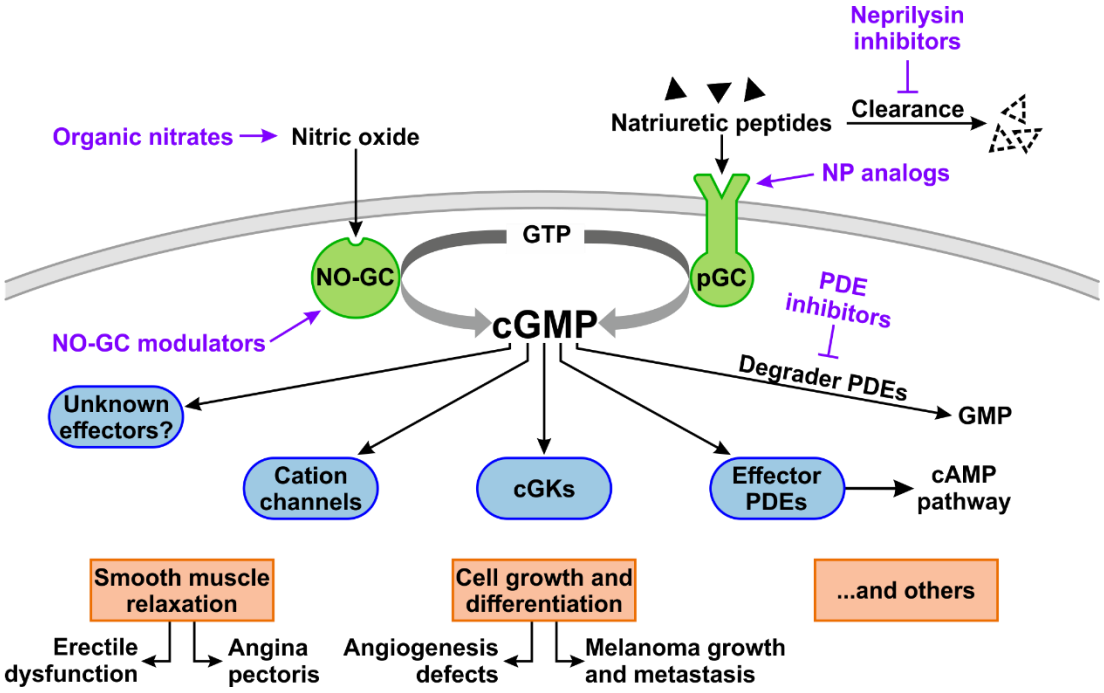

Figure I1: The cGMP signaling pathway. The second messenger cGMP is generated from guanosine triphosphate by GCs (**green**) upon stimulation with their respective ligands, nitric oxide or natriuretic peptides. Downstream of cGMP, its effects are mediated via a set of effector proteins (**blue**), including cyclic nucleotide-gated cation channels, cGKs, and PDEs. cGMP's physiological effects (**orange**) include smooth muscle relaxation and control of cell growth and differentiation, and dysregulation these cGMP-controlled physiological effects is associated with several diseases. Therefore, many drugs have been developed that modulate the cGMP pathway at key positions. Selected drug classes are highlighted as **purple text** (adapted from R. Feil & Kemp-Harper, 2006). NP, natriuretic peptide; NO-GC, NO-sensitive guanylyl cyclase; pGC, particulate guanylyl cyclase; GTP, guanosine triphosphate; cGMP, cyclic guanosine monophosphate; cAMP, cyclic adenosine monophosphate; cGK, cGMP-dependent protein kinase; PDE, phosphodiesterase.

Consequently, cGMP emerged as drug target in diseases involving dysregulation of these (patho-)physiological processes in the past decades (reviewed by Schlossmann & Schinner, 2012). For example, angina pectoris (a type of acute or chronic chest pain caused by occlusion of blood vessels supplying the heart muscle) is treated with substances releasing nitric oxide (NO), which elevates the VSMCs' cGMP levels and thereby triggers relaxation of the occluded blood vessels. It is increasingly recognized that the efficacy of cGMP-modulating drugs is not restricted to cardiovascular diseases. In recent years, many publications suggested their usage in, for example, chronic kidney disease (CKD) (reviewed by Shen et al., 2016), cancer (reviewed by Mintz et al., 2021), and liver fibrosis (Knorr et al., 2008).

1.1.1 cGMP generators and their ligands

cGMP is generated from guanosine triphosphate by two distinct guanylyl cyclase (GC) families: (1) Transmembrane particulate GCs (pGCs) that are activated by various extracellular stimuli including natriuretic peptides (NPs), and (2) NO-sensitive ("soluble") GC (NO-GC) (**Figure I1**) (reviewed by Potter, 2011a). Enzymes of the pGC subfamily are homodimeric and consist of an extracellular ligand binding region, a short ~20 amino acid transmembrane domain, and an intracellular region containing a catalytic GC domain. In mammals, the pGC subfamily has 7 members termed GC-A through GC-G that differ greatly with regard to their ligand and tissue specificity. GC-A generates cGMP upon stimulation with atrial (A-type) NP (ANP) and brain (B-type) NP (BNP). A major role of ANP/GC-A signaling was described in the kidney, vasculature, endothelium and heart, where it regulates natriuresis, blood pressure and cardiac remodeling, respectively (reviewed by Kuhn, 2003). GC-B is stimulated by C-type NP (CNP). CNP/GC-B signaling is present in many different tissues. The most well-described functions of CNP/GC-B are in the bone, nervous system and oocytes, where it regulates endochondral ossification, dorsal root ganglion axon bifurcation and oocyte maturation, respectively (Potter, 2011a). Several studies also have analyzed CNP/GC-B in the cardiovascular system. In contrast to ANP/GC-A signaling, it seems to be less involved in blood pressure regulation, but more in vascular regeneration, cardiomyocyte growth and other disease-relevant processes (Kuhn, 2003). GC-C is stimulated by some heat-stable enterotoxins as well as the intestinal peptides guanylin and uroguanylin, and is expressed in the kidney and

intestinal epithelium. The GC-C enzyme controls intestinal electrolyte/water balance and epithelial cell growth and differentiation. Retinal GCs (GC-E and GC-F) are stimulated by Ca^{2+}/Mg^{2+}, and olfactory GCs (GC-D and GC-G), which are considered pseudogenes in the human, sense different molecular cues including peptide ligands, CO_2, pheromones, and low temperatures (reviewed by Kuhn, 2016).

Finally, there is the NP receptor (NPR)-C, also termed “clearance receptor”, that lacks the intracellular catalytic GC domain. NPR-C is thought to bind and internalize NPs and thereby enable their degradation in various cells and tissues including platelets, VSMCs, glomeruli and adrenal glands (reviewed by Potter, 2011b). In addition to the described NP-clearing effect, NPR-C might exhibit cGMP-independent signaling via coupling to the cyclic adenosine monophosphate (cAMP) signaling pathway (reviewed by Anand-Srivastava, 2005).

As mentioned earlier, GC-A and GC-B are activated by NPs. These peptide ligands share a common, well-conserved 17 amino acid disulfide ring structure but have variable C-terminal and N-terminal tails (He et al., 2006). ANP and BNP are generated mainly in the cardiac atria and ventricles, respectively, and act in an endocrine manner on their target tissues. CNP, on the other hand, is currently regarded to act in an auto- and paracrine manner after local generation, e.g., by endothelial cells. In addition to their clearance via NPR-C, NPs are degraded by the proteases neprilysin and insulin-degrading enzyme (Potter, 2011b).

NO-GC, sometimes also referred to as soluble GC (sGC), forms heterodimers consisting of an α- and a β-subunit (reviewed by Derbyshire & Marletta, 2012). Two functional NO-GC isoforms are present in mammals that are distinguished by their α-subunit, termed NO-GC1 (α1β1) and NO-GC2 (α2β1). Homology analysis also identified a β2-subunit, but it is regarded a pseudogene due to the lack of catalytic activity and gene expression. Both NO-GC1 and NO-GC2 are stimulated by NO, but differ with regard to their expression and interaction partners. Whereas NO-GC2 is mainly detected in the nervous system, NO-GC1 is expressed in a vast number of different cell types including (vascular) smooth muscle cells and platelets. NO-GC1 regulates a plethora of physiologic functions,

including the vascular tone, gastrointestinal motility, and platelet reactivity (reviewed by Friebe & Koesling, 2009; Friebe et al., 2018).

NO-GC is structured in three regions: A ligand binding region, a coiled-coil linker region, and a catalytic GC region. The ligand binding region contains a prosthetic heme-cofactor, which is complexed by histidine 105 of the enzyme's β-subunit. Binding of the endogenous ligand NO is thought to weaken this complex and ultimately induce a conformational change of the coiled-coil and, in turn, catalytic region that activates the enzymatic activity (**Figure I2**) (Horst et al., 2019; Kang et al., 2019). Importantly, the Fe^{2+} in the prosthetic heme group of NO-GC is oxidation-prone. This oxidation to Fe^{3+}-heme does not only interfere with the binding of NO, but also weakens the heme-histidine 105 complex. As a consequence, the enzyme might lose the heme group entirely which results in its heme-free state, apo-NO-GC (reviewed by Krishnan et al., 2018). Since heme-oxidized and apo-NO-GC are no longer activated by NO, oxidation of NO-GC is associated with impaired NO/NO-GC/cGMP signaling, which is considered to play a role in the progression of cardiovascular and renal diseases (Sandner et al., 2021).

In vivo, NO is generated from arginine by nitric oxide synthases (NOS) (reviewed by Forstermann & Kleinert, 1995). There are three different NOS isoforms: neuronal NOS (nNOS or NOS1), inducible NOS (iNOS or NOS2), and endothelial NOS (eNOS or NOS3). eNOS generates NO in endothelial cells. From there, NO diffuses into VSMCs and activates their cGMP generation, leading to vasodilation. nNOS is mainly expressed in neurons, but also in some non-neuronal tissues such as skeletal muscle. The activity of both eNOS and nNOS is dependent on calcium/calmodulin. iNOS is associated with immune response and is found mainly in macrophages, neutrophils, and microglia. In contrast to the other NOS isoforms, iNOS activity is not regulated by calcium but by modulation of its expression. Although NO-GC/cGMP is considered the most important mediator of NO-induced effects, NO can also exert cGMP-independent functions via nitrosylation of metal centers and cysteine residues of proteins (reviewed by Hess et al., 2005).

1.1.2 cGMP effectors and degraders

cGMP's physiological effects are mediated via three classes of downstream effector proteins: (1) cyclic nucleotide-gated (CNG) ion channels, (2) cGMP-dependent protein kinases (cGKs), and (3) bispecific phosphodiesterases (PDEs) (**Figure I1**). CNG channels are non-selective cation channels that allow current of Na^+, K^+, Ca^{2+} and Mg^{2+} upon activation via binding of cyclic nucleotides, i.e., cGMP and cAMP (reviewed by Matulef & Zagotta, 2003). The CNG holoprotein is a heterotetramer formed by varying compositions of different α- and β-subunits. The exact composition determines the cyclic nucleotide selectivity and sensitivity as well as their interaction partners. CNG channels are mainly expressed in rod photoreceptors (mainly cGMP-controlled) and olfactory neurons (mainly cAMP-controlled), where they play a pivotal role in sensation. Expression of CNG channels is also observed in several non-sensory tissues like the kidney, heart, brain, and colon. However, their physiological function in these tissues is not well-understood, and thus far there is no evidence for an involvement of CNG channels in the regulation of blood pressure or blood flow.

cGKs, sometimes also referred to as protein kinase G (PKG), are homodimeric serine/threonine kinases that mediate most of the cGMP-induced effects, for example, in the cardiovascular system (reviewed by R. Feil et al., 2003). The two known cGKs in mammals are cGKI, which has two different isoforms (cGKIα and cGKIβ) differing only in their N-terminal region, and cGKII. The different cGK enzymes and isozymes vary in expression, cGMP affinity, cyclic nucleotide selectivity, substrate specificity, and subcellular distribution. cGKI is a cytosolic protein and is expressed in a vast amount of different cell types. Usually, cGKI α- and β-isozymes are co-expressed, but their relative proportions can vary between cell types. Similar to NO-GC, cGKI plays a major role in the cardiovascular system, gastrointestinal tract, platelets and the brain, where it regulates vascular tone, gastrointestinal motility, platelet reactivity and learning, respectively. Of note, cGKI also has a pro-angiogenic function (Yamahara et al., 2003). This concurrence of expression patterns and physiological effects indicates that NO-GC/cGMP signaling is mainly transduced via cGKI. In contrast to cGKI, cGKII is anchored to the plasma membrane via an N-terminally attached myristoyl group. A function of cGKII is described,

for example, in the kidney, bone, and brain. Given its weak expression in VSMCs, a function of cGKII in the cardiovascular system has not yet been postulated.

PDEs compose a superfamily of enzymes hydrolyzing cyclic nucleotides, i.e., cGMP and cAMP (reviewed by Bender & Beavo, 2006). The PDE superfamily consists of 11 members, PDE1 to PDE11, most of which have several subtypes and/or isoforms specified with a suffix letter and number, respectively. They differ in their expression patterns, ligand selectivity, and substrate specificity. There is also some evidence that PDEs might control distinct “cGMP pools”, meaning that specific PDEs restrict the subcellular distribution of cGMP generated by different GCs. With respect to specificity, PDEs 4, 7 and 8 are cAMP-specific, whereas PDEs 5, 6 and 9 are cGMP-specific. All other PDEs (1, 2, 3, 10 and 11) are bispecific and can bind both cGMP and cAMP. In addition to their common cyclic nucleotide-degrading function (“degrader PDEs”), these bispecific PDEs might also mediate downstream signaling by establishing a cGMP/cAMP crosstalk (“effector PDEs”). A pivotal role of PDEs was described, for example, in the brain and the cardiovascular system, where they regulate pain processing, learning and memory, cardiac contractility, cardiomyocyte growth and survival, as well as vessel relaxation. However, given the vast number of different PDE subtypes, their involvement in physiological processes is complex and diverse, and PDE inhibitors often have several physiological effects (Bender & Beavo, 2006).

1.1.3 Pharmacological relevance of cGMP

As indicated in the previous sections, the cGMP signaling pathway plays a central role in a plethora of physiological processes. Therefore, it is not surprising that components of the cGMP signaling pathway are readily utilized as drug targets in several diseases. In **Figure I1**, selected classes of cGMP-modulating drugs that are currently used for therapy or gained popularity in recent years are highlighted (purple text). In the next paragraphs, the clinical significance of these drug classes will be discussed briefly.

Perhaps the most famous cGMP-targeting drug is sildenafil, best known under the trade name Viagra®. Sildenafil is a PDE5 inhibitor used to treat erectile dysfunction (reviewed by Baillie et al., 2019). PDE5 is the major calmodulin-independent cGMP-hydrolyzing PDE in VSMCs (reviewed by Polson & Strada, 1996). Its inhibition amplifies the

stimulation of the cGMP signaling pathway via endogenous NO and ANP. In the context of erectile dysfunction, this facilitates swelling of the corpora cavernosa during sexual arousal (reviewed by Francis & Corbin, 2005). The effect of PDE5 inhibition is not limited to VSMCs in the penis. Hence, sildenafil is also an approved drug for therapy of pulmonary arterial hypertension. However, as mentioned above, this broad efficacy combined with limited selectivity of PDE inhibitors culminates in many adverse effects. For instance, sildenafil can induce photophobia and blurred vision due to off-target inhibition of retinal PDE6 (reviewed by Auso et al., 2021). Furthermore, the mode of action of PDE inhibitors (i.e., inhibition of cGMP degradation) requires endogenous cGMP generation to be effective, which might not be given under all disease conditions. Nonetheless, today's repertoire of PDE inhibitors comprises non-selective as well as selective inhibitors for almost all PDE superfamily members.

A different approach is to target cGMP generation instead of its degradation. With regard to NP/pGC/cGMP signaling, drugs exist that (1) inhibit NP degradation or (2) stimulate pGCs in an agonistic manner. A compound from the first drug class is sacubitril, an inhibitor of the NP-degrading endopeptidase neprilysin. This inhibition of NP degradation results in elevated NP levels and thus increased cGMP. In chronic heart failure, an imbalance of NP/pGC/cGMP and angiotensin II signaling, two pathways that have inverse effects on cardiac contractility, is considered a major cause and driver of the disease. The cGMP system is thought to have a preserving effect on heart function, whereas excess angiotensin II signaling might be harmful. Consequently, the combination drug sacubitril/valsartan (an angiotensin receptor inhibitor) (McMurray et al., 2014) (reviewed by Gori et al., 2021) has been approved under the trade name Entresto® for the treatment of chronic heart failure in 2015. Given the prominent role of cGMP in VSMC relaxation, it is not surprising that hypotension is among sacubitril's adverse effects.

Like sacubitril, pGC agonists also augment the pGC-dependent cGMP signaling. Thus far, the success of pGC agonists is limited, most likely due to their poor *in vivo* stability and pharmacokinetic profiles. Nonetheless, the stable CNP analog vosoritide, also referred to as BMN-111, recently has successfully passed its phase III clinical trial for treatment of achondroplasia (Savarirayan et al., 2019; Savarirayan et al., 2020). This

disease is caused by an impairment of chondrocyte proliferation and extracellular matrix generation via increased fibroblast growth factor receptor 3 signaling. GC-B/cGMP signaling counteracts this pathological phenotype and significantly accelerates skeletal growth of the achondroplasia patients. The development of additional pGC agonists might give access to completely new therapeutic approaches, given the issues with their pharmacokinetics can be overcome.

NO-GC provides an opportunity to pharmacologically intervene in the NO/cGMP signaling pathway. Historically, NO-releasing nitrates like nitroglycerin are used to treat angina pectoris (Murrell, 1879). In this disease, the occlusion of blood vessels in the heart limits the oxygen supply to the heart muscle. Stimulation of the NO/cGMP pathway in VSMCs of these cardiac vessels triggers vasodilation, and thereby restores oxygen supply and heart function. However, these “traditional” NO-releasing compounds have major drawbacks including severe adverse effects (i.e., “Sunday heart attacks” and “Monday disease”) (Marsh & Marsh, 2000), development of drug tolerance and dependence, and insufficient efficacy under certain disease conditions (i.e., oxidative stress) (Sandner et al., 2021). To overcome these drawbacks, NO-independent modulators of NO-GC have been developed that are described in more detail in the following section.

1.1.4 NO-GC stimulators and activators

NO-GC stimulators and activators (sometimes summarized under the term “NO-GC modulators”) both induce generation of cGMP by NO-GC, but via different mechanisms (reviewed by Sandner, 2018; Sandner et al., 2021). NO-GC *stimulators* bind allosterically to the NO-GC β-subunit, which induces a conformational change stabilizing the enzyme’s activated state (**Figure I2**) (Liu et al., 2021). NO-GC stimulators not only increase NO-GC’s basal cGMP generation in the absence of NO, but also have a strongly synergistic effect by reducing the NO concentration required to achieve full enzymatic activity. However, as mentioned in 1.1.1, NO-GC is prone to oxidation of its heme cofactor (**Figure I2**). Heme oxidation weakens the NO-GC/heme complex, which can result in its dissociation and formation of the heme-free apo-NO-GC state. Both heme-oxidized and heme-free NO-GC are unresponsive to the endogenous ligand NO as well as to NO-GC stimulators. NO-GC *activators* fill this niche: They can replace the weakly bound

Fe^{3+}-heme of heme-oxidized NO-GC and bind to the unoccupied heme pocket of apo-NO-GC, thereby inducing cGMP generation (**Figure I2**) (Liu et al., 2021).

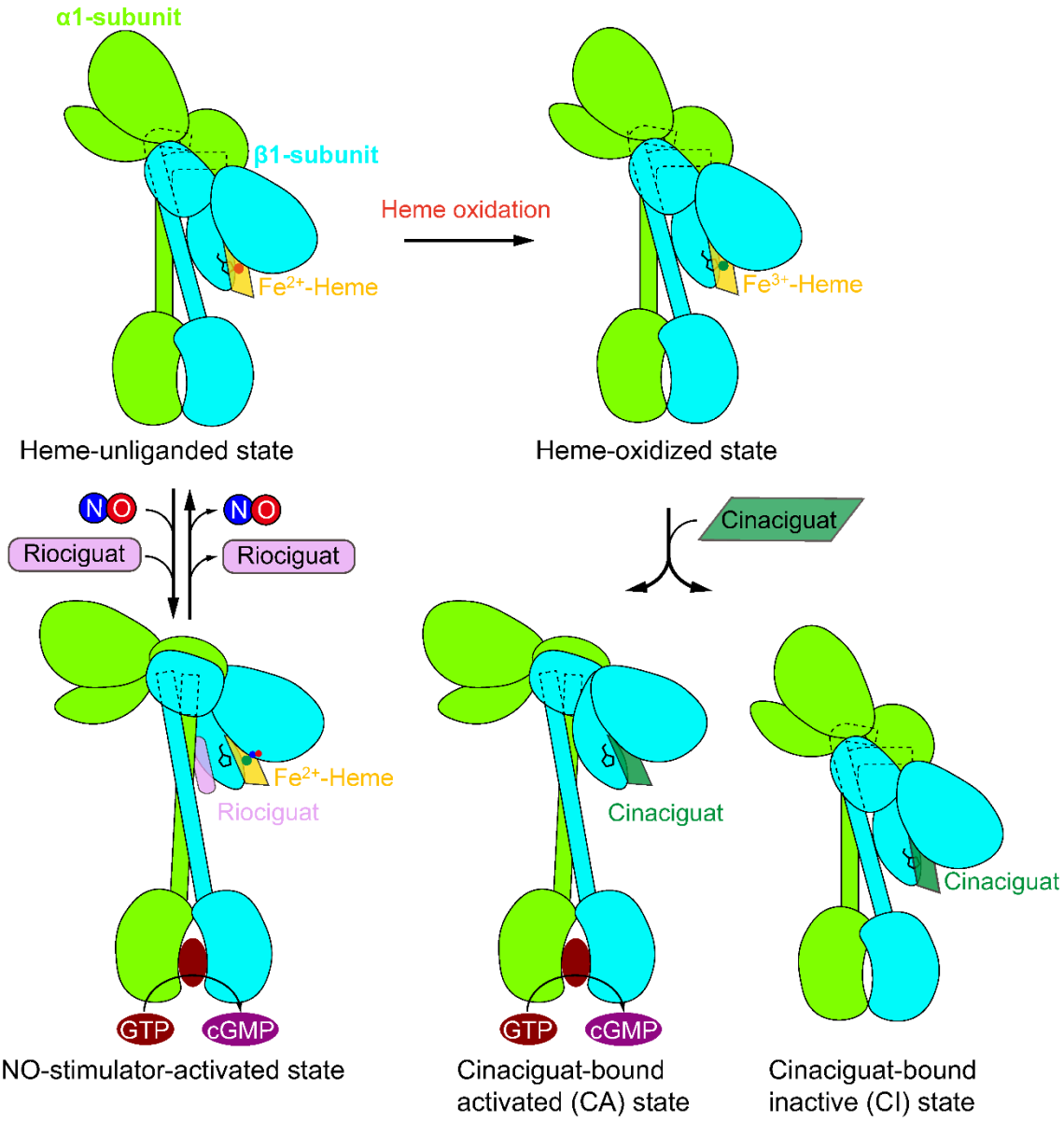

Figure I2: NO-GC stimulator and activator modes of action. In its native, Fe^{2+}-heme-containing state, NO-GC binds to and is activated by NO. This native state as indicated is also allosterically bound by NO-GC stimulators like riociguat, which thereby increase the enzyme's catalytic activity. Oxidative stress might lead to oxidation of NO-GC's heme cofactor, impairing its enzymatic function. While heme-oxidized NO-GC can no longer be activated by NO or NO-GC stimulators, NO-GC activators like cinaciguat can replace the weakly bound Fe^{3+}-heme, which might result in formation of NO-GC's activated state (adapted from Liu et al., 2021).

Together, NO-GC stimulators and activators provide powerful tools to restore NO-GC/cGMP signaling under pathological conditions of reduced NO bioavailability and/or oxidative stress. For example, NO-GC modulators have pharmacological implications in the cardiovascular system, kidney, and fibrosis (Sandner et al., 2021). Consequently, the first NO-GC stimulator (riociguat) has been approved for the treatment of pulmonary hypertension in 2013. Additional preclinical and clinical studies are in progress for heart failure, erectile dysfunction, type 2 diabetes, cystic fibrosis, CKD and liver disease. The latter three disorders are associated with fibrosis, which commonly goes hand in hand with oxidative stress (reviewed by Parola & Robino, 2001). This is where NO-GC activators shine most, as they selectively stimulate the disease-related heme-oxidized and heme-free NO-GC to generate cGMP without interfering with NO-GC/cGMP signaling in healthy ("non-oxidized") tissue. Together, NO-GC stimulators and activators seem to be able to promote cGMP signaling in a broad range of diseases and it is likely that future studies as well as next-generation NO-GC modulators will enable even more applications.

1.1.5 cGMP imaging with fluorescent biosensors

cGMP concentrations conventionally are measured via antibody-based assays with lysed and homogenized tissue or cell samples. Although these immunoassays have their place as methods to quantify absolute cGMP levels, recent advances in the cGMP field highlight the importance of measuring cGMP at the (sub-)cellular level. Different cells from the same tissue greatly vary with regard to their cGMP signaling, and even within the same cell, cGMP might be distributed in an inhomogeneous manner (reviewed by R. Feil et al., 2021). For this reason, genetically encoded cGMP biosensors have been developed that enable *in situ* cGMP visualization in live single cells and tissues and in real time using modern microscopy techniques.

To date, the most used cGMP biosensors are based on the principle of Förster/fluorescence resonance energy transfer (FRET). They consist of a FRET donor fluorophore, a FRET acceptor fluorophore and a linker region containing a cGMP binding domain derived from either cGKs or PDEs. FRET relies on the proximity- (~2-6 nm) and orientation-dependent energy transfer from the excited donor to the acceptor fluorophore.

Binding of cGMP leads to a conformational change of the sensor protein that affects the FRET efficiency. In case of cGi500 (cGMP indicator with an EC_{50} of 500 nM; this cGMP biosensor was used in in the present study), the tandem cGMP binding domain of cGKI is flanked by enhanced cyan fluorescent protein (CFP) and enhanced yellow fluorescent protein (YFP) (**Figure I3**) (Russwurm et al., 2007). In basal state (i.e., when the cGMP concentration is low), FRET takes place from CFP to YFP. Binding of cGMP (i.e., high cGMP concentration) results in a conformational change leading to decreased FRET efficiency. Therefore, the CFP/YFP ratio (referred to as "R (cGMP)" herein) correlates with the cGMP concentration and can be used as an output parameter.

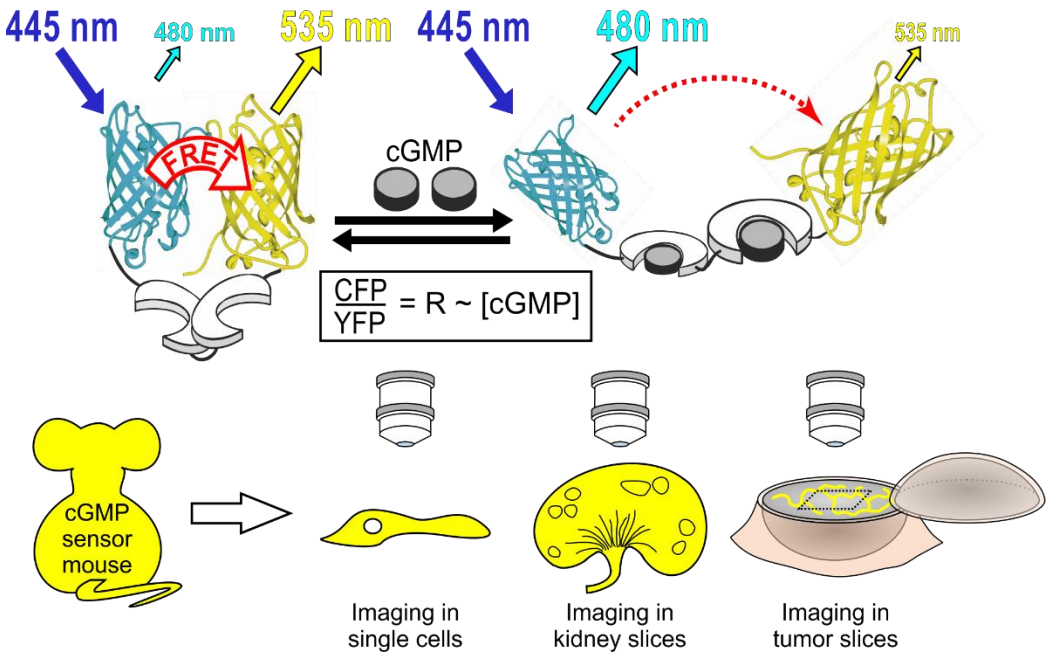

Figure I3: Working principle of the FRET-based cGMP sensor cGi500. cGi500 consists of CFP and YFP linked by the tandem cGMP binding domain of bovine cGKI. In basal state (low [cGMP]), FRET takes place from CFP to YFP. Binding of cGMP (high [cGMP]) results in a conformational change that leads to reduced FRET. Therefore, the CFP/YFP ratio R correlates with the cGMP concentration. cGMP sensor mice expressing cGi500 either globally or in distinct cell populations can be used to isolate primary cells and intact tissues for *in situ* cGMP visualization (adapted from Thunemann, Wen, et al., 2013).

To accomplish ease of use and eligibility for *ex vivo* and *in vivo* studies, Thunemann, Wen, et al. (2013) have generated transgenic mice stably expressing cGi500 globally (cGi-L1) or allowing its cell type-specific expression (mT/cGi-L2). Both cGMP sensor constructs are inserted into the *Rosa26* gene locus and driven by the strong ubiquitous cytomegalovirus early enhancer/chicken β-actin/β-globin (CAG) promoter.

Cell type-specificity of the mT/cGi-L2 construct is achieved via the cyclization recombination (Cre) / locus of X-over P1 (loxP) system. Cre is a site-specific recombinase from bacteriophage P1 that recognizes pairs of homologous loxP sequences (R. Feil, 2007). Depending on the orientation of the two loxP sites, Cre executes inversion, deletion, integration, or translocation of DNA segments. Transgenic animal models predominantly utilize Cre-mediated deletion due to the highly efficient and almost irreversible character of this reaction. Commonly, a target DNA sequence is flanked by loxP sites of the same orientation ("floxed"). Active Cre excises these floxed sequences. While the implication for gene knock-out (ko) is obvious, it can also be used to *induce* gene expression in a controlled manner. To do so, a floxed gene or stop cassette is inserted between the promoter and the Cre-controlled gene. In mT/cGi-L2 mice in particular, a floxed membrane-targeted *tdTomato* (*mT*) gene separates CAG promoter and *cGi500* gene (**Figure I4**) (Thunemann, Wen, et al., 2013).

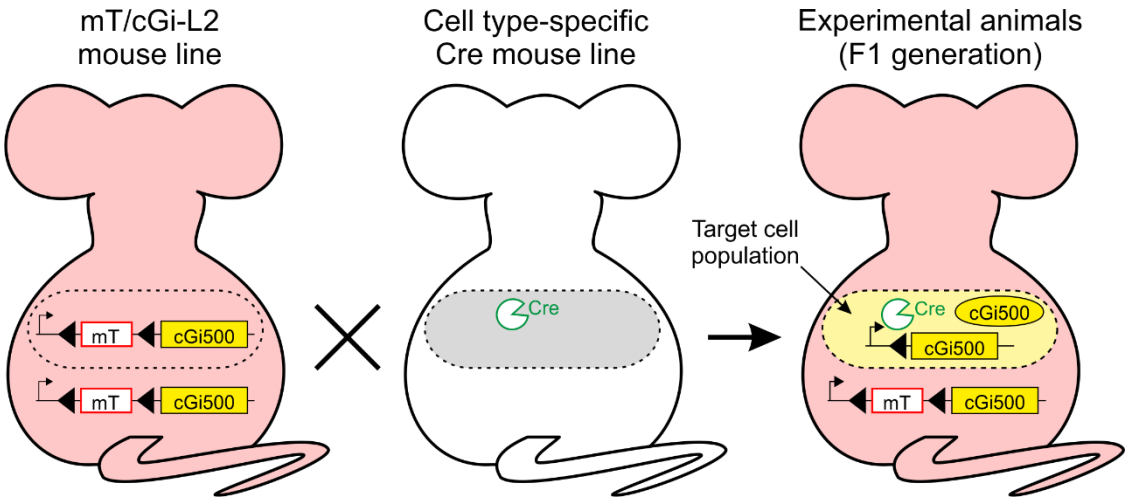

Figure I4: Generation of cell type-specific cGMP sensor mice. mT/cGi-L2 mice carry a transgene in the *Rosa26* locus consisting of the strong ubiquitous CAG promoter (black bent arrows), a floxed *mT* gene, and the *cGi500* gene. Prior to Cre recombination, mT is expressed in all cells (red coloring). When these mT/cGi-L2 mice are crossbred with mice expressing Cre under a cell type-specific promoter (gray coloring), the *mT* gene is specifically removed in the target cell population of experimental animals. Removal of the *mT* gene results in cGi500 expression specifically in the recombined target cells (yellow coloring). Black arrowheads indicate location and orientation loxP sites.

Cre expression usually is driven by a cell type-specific promoter to limit recombination to the target cell population. The pool of transgenic Cre mouse lines with varying expression patterns – sometimes referred to as "Cre zoo" – has grown substantially over the years.

Today, Cre mouse lines exist for almost any tissue within the murine body including the endothelium (e.g., *Cdh5* and *Tek* promoters) and smooth muscle/pericytes (e.g., *Acta2* and *Tagln* promoters). Some Cre mouse models utilize modified versions of the Cre enzyme which are fluorescent (e.g., GFP-Cre), codon-optimized (iCre), split into an N- and a C-terminal fragment (split-Cre), or inducible (CreERT2) (Addgene, 2019) (reviewed by Tian & Zhou, 2021). In the CreERT2 construct, Cre is fused to a modified estrogen receptor (ER) that no longer binds its endogenous ligand estrogen, but the partial ER agonist 4-hydroxytamoxifen, a metabolite of the synthetic drug tamoxifen. Upon binding of 4-hydroxytamoxifen, the CreERT2 fusion protein translocates into the nucleus where it can execute recombination (S. Feil et al., 2009). This sophisticated model enables tissue-**and** time-controlled recombination. Since the recombination is irreversible, marked cells will retain their reporter gene expression even if Cre is no longer active. Thereby, time-restricted administration of tamoxifen enables tracking of marked cell populations during developmental processes and disease progression ("fate-mapping") (S. Feil et al., 2014).

1.2 The kidney and its (patho-)physiology

Kidneys are crucial for body homeostasis: They excrete toxins and metabolites while keeping water and salts in balance, and they regulate other organ's function via secretion of various hormones. Anatomically, the kidney is structured in cortex, medulla and pelvis (**Figure I5**) (Silbernagl, 2005), surrounded by the tough fibrous renal capsule. Unfiltered blood enters the kidney via the renal artery and is transported to the glomeruli inside the renal cortex. Glomeruli constitute the first part of the nephrons, the functional units of the kidney. Renal glomeruli consist of a very dense and highly permeable network of capillaries that allows water and other small molecules to leave the blood stream and enter the renal tubular system as primary urine (~90 l/d per human kidney; also referred to as glomerular filtration rate (GFR)). The GFR is one of the most important measures of renal function. However, primary urine is heavily processed within renal tubules. Depending on the physiological circumstances, substances can be resorbed or actively secreted by peritubular capillaries. All renal tubules culminate in the ureter, which transports the processed secondary urine (~0.75 l/d per human kidney) to the bladder for final excretion.

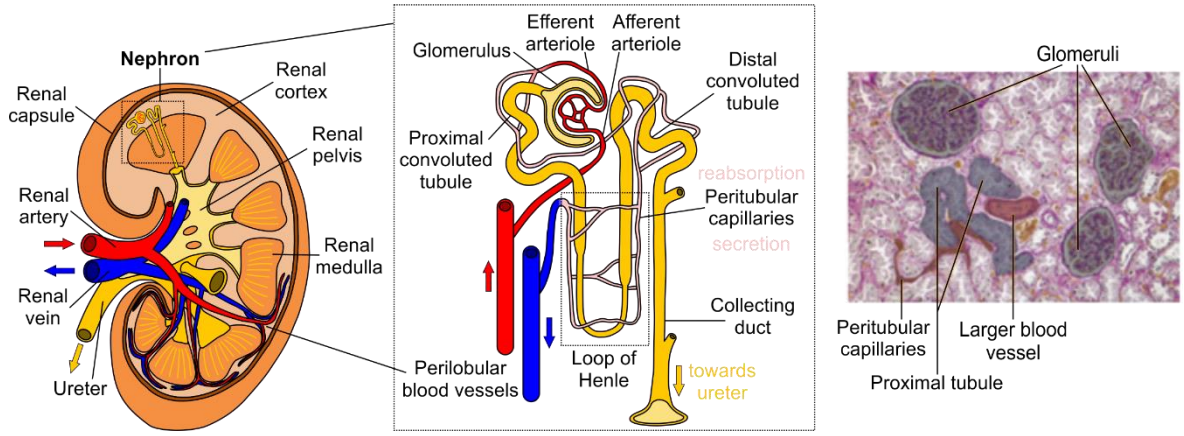

Figure I5: Kidney anatomy and its functional unit, the nephron. Blood from perilobular arteries enters the nephron via afferent arterioles. These branch into the dense glomerular capillary network from which the primary urine is drained. The contraction of these intraglomerular capillaries is controlled by specialized pericytes called mesangial cells. The primary urine enters the renal tubular system consisting of proximal convoluted tubules, the straight loop of Henle, and distal convoluted tubules which are connected with the glomerulus via the so-called juxtaglomerular apparatus. Filtered secondary urine is then transported towards the ureter via the collecting duct. The glomerular capillaries merge into efferent arterioles which again branch into a capillary network, the peritubular capillaries. Over the whole length of the tubules, these peritubular capillaries reabsorb substances from (e.g., H_2O, ions) and secrete substances into (e.g., metabolites) the tubules. The histological image on the right was taken from Silbernagl (2005) and shows a hematoxylin-eosin staining of the renal cortex. Labelled structures are highlighted in light gray for clearer distinction.

1.2.1 Chronic kidney disease (CKD) and its therapies

Given the kidneys' important role for body homeostasis, high continuous stress and close integration in systemic processes, it is not surprising that kidney disease is one of the leading causes of death (Ritchie & Roser, 2018). Kidney failure is often preceded by CKD and its main risk factors, cardiovascular disease, diabetes, obesity, and renal inflammation. Many of these risk factors are associated with elevated blood pressure, specifically in glomerular resistance vessels. Sustained high blood pressure induces glomerular damage and thereby affects GFR and proteinuria, which are the main measures of kidney function (reviewed by Johnson et al., 2004a; Johnson et al., 2004b). In a compensatory feedback loop, the undamaged glomeruli secrete more renin which in turn leads to hyperactivation of the renin-angiotensin-aldosterone system (RAAS). RAAS hyperactivation is associated with vasoconstriction, which elevates the systemic blood pressure and induces further glomerular damage (reviewed by Ku et al., 2019).

Consequently, current first-line CKD treatments mainly target the RAAS. Although these therapies reduce the systemic blood pressure and improve kidney function in patients with renal disease, the effects often are not maintained in chronic therapy (reviewed by Breyer & Susztak, 2016) and in patients with type 2 diabetes (Schievink et al., 2016). An emerging therapeutic alternative to RAAS inhibitors is sodium-glucose-cotransporter 2 inhibitors (SGLT2i), which were recently approved for type 2 diabetes treatment. SGLT2i reduce the blood pressure, presumably via induction of natriuresis and reduction in sympathetic tone (reviewed by Briasoulis et al., 2018; Vallon & Thomson, 2017), and ameliorate the long-term GFR decline in CKD patients (Lin et al., 2019; Muskiet et al., 2017). However, several studies have reported an initial GFR decrease under SGLT2i (Sugiyama et al., 2020) (reviewed by Szalat et al., 2018), demanding caution when patients at danger of acute renal injury are treated. Thus, there is still need for new CKD therapies with different molecular modes of action that complement the currently used drugs in patients at acute risk of kidney failure.

1.2.2 cGMP in the healthy and diseased kidney

The cGMP pathway is a central regulator of kidney function (reviewed by Chen & Burnett, 2018; Krishnan et al., 2018) and as such might provide a suitable target for novel CKD therapies. Physiologically, cGMP has natriuretic (Na^+ excretion) and diuretic (H_2O excretion) effects (Burnett et al., 1984; Weidmann et al., 1986) through modulation of aquaporins and ion channels. Furthermore, cGMP increases the GFR and overall renal blood flow (C. L. Huang et al., 1986), presumably by regulating VSMC and mesangial cell contraction and thus controlling the tone of glomerular arterioles and capillaries. Finally, cGMP might exert renoprotective effects by preventing renal fibrosis and inflammation (Kumar et al., 2017; Yoshihara et al., 2015), and by negatively regulating the RAAS (Burnett et al., 1984) via a reduction of renin release from juxtaglomerular cells. There is evidence that cGMP in the kidney can be produced via ANP/GC-A, CNP/GC-B and NO/NO-GC. Consistently, NO-GC gain of function is associated with an improved GFR and a lower risk for CKD (Emdin et al., 2018).

Although cGMP's pivotal role in the regulation of renal function is evident, the underlying molecular and cellular mechanisms are not well-characterized. To date, most studies

focused on the physiological effects of cGMP-stimulating drugs on the kidney rather than on signal transduction. However, expression analysis revealed differences in renal GC distribution and activity. Theilig et al. (2001) reported NO-GC expression in some interstitial fibroblasts as well as in contractile cells of the kidney, including arteriolar VSMCs, pericytes of the peritubular capillary network, and glomerular mesangial cells. Podocytes and endothelial cells, on the other hand, were demonstrated to be NO-GC-negative by immunohistochemical staining. Importantly, both cultured podocytes (Theilig et al., 2001) and glomerular endothelial cells (Green et al., 1994) generated cGMP in response to ANP as determined *in vitro* via immunoassay. Therefore, at least some of their physiological effects might be specific for ANP and NO, respectively, since they target different cell populations.

Recent studies have highlighted that oxidative stress triggered by common comorbidities in CKD, like hypertension, diabetes and obesity, could be one of the drivers of kidney function decline during CKD (Samarghandian et al., 2017) (reviewed by Coppolino et al., 2018; Sinha & Dabla, 2015; Su et al., 2019). Oxidative stress can disrupt the NO-GC/cGMP pathway by scavenging NO (Huie & Padmaja, 1993) and oxidizing NO-GC (Stasch et al., 2006), and thereby it might interfere with the physiological regulation of kidney function by NO. Therefore, NO-GC modulators might prove useful for restoring kidney function in CKD patients.

1.3 The skin, melanocytes, and melanoma

1.3.1 Function and structure of the skin

The skin is one of the primary barriers of the mammalian body. It consists of the epidermis, basement membrane and dermis, and is connected via the subcutis to other tissues like skeletal muscle (**Figure I6**) (Kolarsick et al., 2011; D. J. Tobin, 2011).

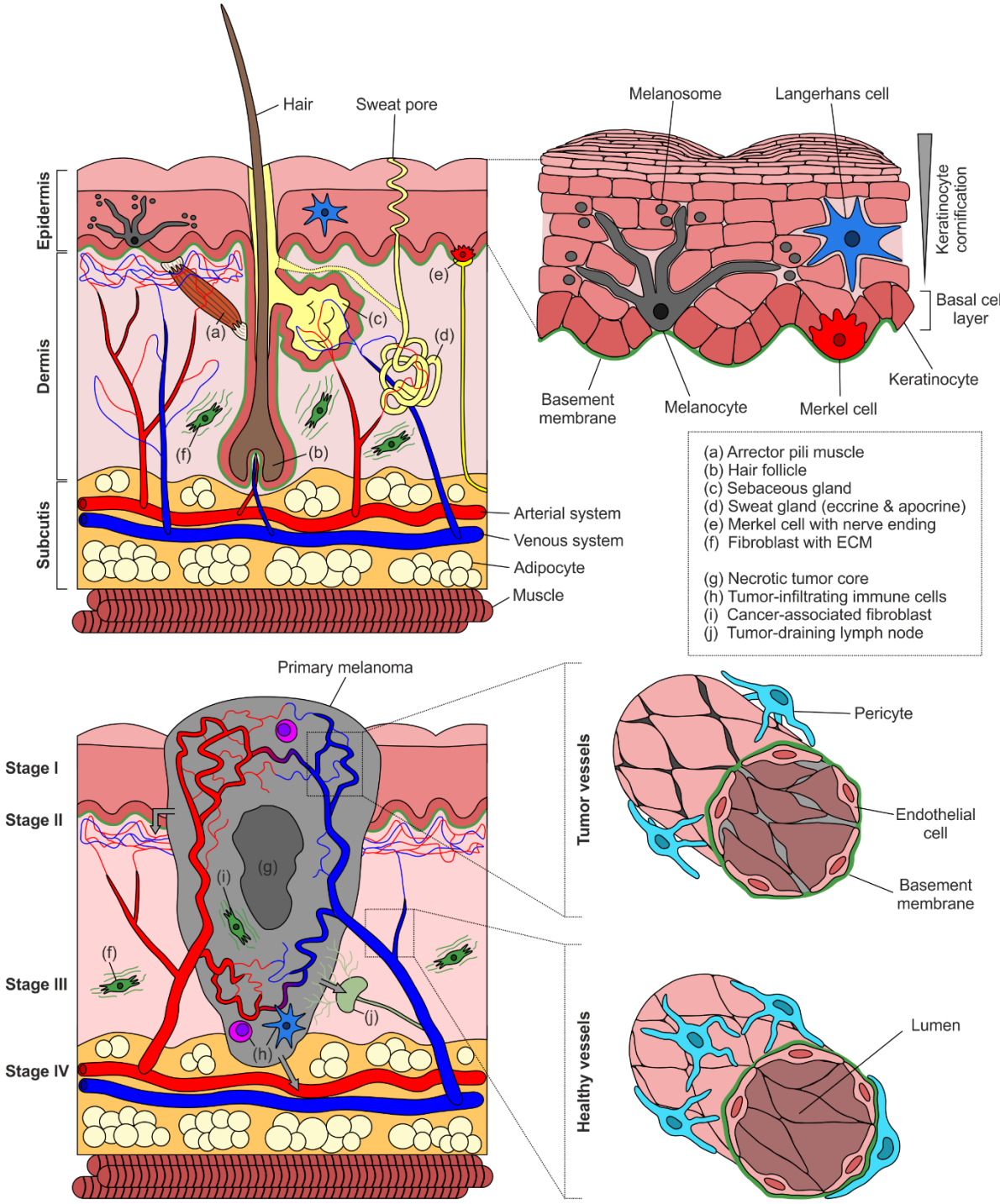

Figure I6: Structure of the skin without (top) and with (bottom) a primary melanoma. The outer layer of the skin (the epidermis; detailed view in the top right) can be subdivided into several layers differing in keratinocyte cornification. The deepest layer (basal cell layer) is directly connected to the basement membrane and contains melanocytes (melanin/melanosome generation and secretion into keratinocytes), Merkel cells (touch sensation), and keratinocytes some of which are highly proliferative ("basal keratinocyte stem cells"). Keratinocytes newly formed from these stem cells are pushed outwards, where they start to produce high amounts of keratin. As they continue to move outwards, they eventually reach their fully cornified final differentiation state, in which they are dead, flattened out and surrounded by a barrier-like

envelope. The inner skin layer (the dermis) is less dense and mainly contains ECM-producing fibroblasts and larger structures including blood vessels, hairs and glands. Two distinct types of sweat glands exist in mammals: Eccrine sweat glands that secrete via sweat pores onto the skin surface and apocrine sweat glands that secrete into hair follicles (indicated here with dashed lines). The tissue beneath the skin (the subcutis) consists of adipose tissue as well as nerve fibers and large blood vessels, which innervate and ensure blood supply for the skin, respectively. Cancer can arise from several cells within the skin including keratinocytes, Merkel cells and melanocytes. Malignancy of melanocytes is called melanoma. Depending on size, ulceration and spreading, it is classified into 4 stages. In stage I, the tumor stays within the boundary of the epidermis where it first occurs. As soon as melanoma ulcerates through the basement membrane or reaches a certain size, it is classified stage II. Late-stage melanoma finally involves spreading to the lymph nodes (stage III) or distant organs (stage IV). Melanoma mostly metastasizes to the lungs, probably through the vascular system. All mentioned major migration events are indicated with gray arrows. As tumors grow larger, they start to massively recruit blood vessels, resulting in an abnormal, barely functional vascular system within the tumor. Some key aspects of tumor vessels as compared to healthy vessels (exemplified by small arterioles/venules) are depicted on the bottom right. In healthy vessels, endothelial cells are closely connected through tight and adherens junctions, ensuring impermeability for large molecules as well as steady blood flow. Small arterioles and venules are surrounded by a dense network of pericytes that regulate the vessel diameter and thereby the blood flow. Tumor vessels, on the other hand, have fewer pericytes that are loosely or not at all connected to the endothelium, and are abnormally dilated and leaky. Vessel leakage is associated with reduced vascular perfusion. Hence, blood flow in tumors is impaired despite heavy angiogenesis. Together, this leads to insufficient oxygen and nutrient supply especially in the tumor core, which often is necrotic. ECM, extracellular matrix.

The epidermis (**Figure I6**, top right) is the outermost skin layer and thus directly exposed to environmental threats including extreme temperatures, ultraviolet (UV) radiation, and pathogens. Cells of the epidermis therefore are specialized to counteract these damages. Keratinocytes, which constitute at least 80 % of all epidermal cells, are characterized by strong expression of the intermediate filament protein keratin and increasing cornification over their cellular lifespan. Finally, they form a cornified envelope that prevents environmental damage to the proliferative deeper tissues as well as excess loss of body liquids through the skin. After their terminal cornification, keratinocytes are shed off and replaced by stem cells located in the epidermal proliferation units next to the basement membrane. Melanocytes constitute another 5-10 % of cells in the basal layer of the epidermis (Venus et al., 2011). Their main function is to generate the black pigment melanin from tyrosine with the help of the enzyme tyrosinase. Melanin absorbs UV light and thereby protects sub-epidermal tissues from UV radiation-induced deoxyribonucleic acid (DNA) damage. Other epidermal cell types include Merkel cells (touch sensation) and Langerhans cells (skin-resident macrophages).

The second, inner skin layer is called dermis and is separated from the epidermis by the basement membrane (**Figure I6**, top left). It mainly consists of macrophages, mast cells

and fibroblasts, as well as a vast amount of extracellular matrix produced by fibroblasts. In addition, the dermis is pervaded by many structures including a dense vascular network, hairs and hair follicles, sebaceous glands, sweat glands, the corresponding excretory ducts, and (mainly sensory) nerves (D. J. Tobin, 2011). The dermis merges into the subcutis (also termed hypodermis), which connects the skin with underlying tissues. This loose connective tissue is rich in adipocytes and contains larger vessels as compared to the dermis.

1.3.2 Melanoma

Melanoma is a malignancy of the epidermal melanocytes (**Figure I6**, bottom). It might not be the most common type of cancer, but it is one of the deadliest. Patients with advanced melanoma have a disillusioning 5-year survival rate of only about 27 % (Halpern et al., 2021). Consistent with the sun-exposed localization of melanocytes, UV radiation is considered an important cause of cutaneous melanoma (Elwood & Gallagher, 1998).

Most human melanomas carry activating mutations in proto-oncogenes of the mitogen-activated protein kinase (MAPK) signaling cascade and inactivating mutations in tumor suppressor genes. Most frequently, the *BRAF* (63 % of melanoma patients), *NRAS* (26 %), *TP53* (19 %) and *PTEN* (12 %) genes are affected (Hodis et al., 2012). Preclinical studies in mice as well as clinical observations in cancer patients have suggested that formation of cancers, including melanoma, requires several mutations in proto-oncogenes and tumor suppressor genes (Dankort et al., 2009; Vogelstein & Kinzler, 1993).

Melanoma can be classified into stages I to IV depending on tumor size, ulceration, lymph node spreading (stages III-IV) and metastasis (only stage IV) (**Figure I6**, bottom left) (The American Cancer Society, 2019). Early intervention is associated with a good prognosis, since the skin is an easily accessible tissue and the tumor can be simply removed by surgery. However, melanoma is a highly invasive cancer and as soon as it enters stages III-IV, the 5-year survival goes down substantially from 99 % (stage I) over 66 % (stage III) to 27 % (stage IV) (Halpern et al., 2021). For late-stage melanoma, more advanced therapies like those specified in the following paragraph are necessary.

1.3.3 Late-stage melanoma therapies

Since the MAPK cascade is mutated in most human melanoma patients, it has been recognized early that therapies targeting the respective oncogenes have high potential. This has led to the development of drugs like vemurafenib (BRAF inhibitor) and trametinib (MAPK kinase inhibitor) (reviewed by Zeiser et al., 2018). Vemurafenib (also referred to as PLX-4032) selectively inhibits the predominant BRAF mutants, $BRAF^{V600E/K}$. Patients with $BRAF^{V600E/K}$ mutation have a very solid initial response rate to vemurafenib with around 50 % (Czirbesz et al., 2019; Roche Pharma AG, 2012). However, targeted therapies often fail to achieve long-lasting effects due to the development of clinical resistance. In case of vemurafenib, a preclinical study has observed drug-tolerant microenvironments with increased integrin β1/FAK signaling compensating for the lost MAPK signaling (Hirata et al., 2015). Independent of the exact mechanism, the high melanoma recurrence rate in targeted therapies remains an important clinical problem.

Recent advances have profoundly improved the efficacy of immunotherapy in melanoma treatment. The most striking advance has been the development of immune checkpoint blockade (ICB) (reviewed by Ito et al., 2015; Topalian et al., 2015). This approach makes use of inhibitors of the so-called immune checkpoint proteins, which normally prevent the immune system from overshooting. One of the hallmarks of cancer is immune evasion, which at least in part is due to an overactivity of the immune checkpoint system in tumors (reviewed by Vinay et al., 2015), leading to an inhibition of the natural immune response of the body against the cancer. Melanoma is no exception to this mechanism. Although melanomas often generate high amounts of eligible T cell antigens like proteins involved in melanin biosynthesis and melanosome formation (e.g., tyrosinase) (Cormier et al., 1998), ICB is necessary for a robust anti-tumor immune response (Hodi et al., 2010). Today, physicians have access to several antibodies inhibiting immune checkpoint proteins, most importantly programmed cell death protein 1 (PD-1; i.e., nivolumab and pembrolizumab) and its ligand PD-L1 (i.e., atezolizumab), as well as cytotoxic T-lymphocyte-associated protein 4 (CTLA-4; i.e., ipilimumab). These antibodies can be administered alone or in combination with immune stimulation (e.g., with tumor antigen therapy (Hodi et al., 2010) or cytokine therapy (Davar et al., 2018)) to induce a strong anti-tumor immune response. Preclinical studies suggest that combination of ICB with

adoptive T cell transfer (Shi et al., 2019) might also be effective in melanoma patients. Importantly, cancer immunotherapy is independent of the above-mentioned common mutations in melanoma. Still, the objective response rates of ICB therapies are suboptimal, varying between 5 and 40 % depending on the used antibody and the type of co-therapy (Ito et al., 2015).

Targeted therapies and immunotherapy can be combined with each other or with common anti-cancer treatments like radio- and chemotherapy (e.g., dacarbazine, cisplatin, and paclitaxel). These combination therapies, especially those involving ICB, are heavily researched and the clinical data looks promising (Robert et al., 2011) (reviewed by Karachaliou et al., 2017; Ko & Formenti, 2018). However, some studies have reported serious adverse effects and drug-related toxicities of ICB combination therapies (Carretero-Gonzalez et al., 2019; Yamazaki et al., 2015), and many late-stage melanoma patients still do not or only partially respond to the established combination therapies. A better understanding of the mechanisms underlying melanoma development and progression as well as additional drug targets might therefore further improve treatment efficacy and overall survival of melanoma patients.

1.3.4 Vascular modulation in cancer therapy

The tumor vasculature is a potential drug target. Sustained angiogenesis has been defined as a hallmark of cancer a long time ago (reviewed by Hanahan & Weinberg, 2000). This abnormal sustained angiogenesis is necessary to meet the nutrient requirements of proliferative neoplastic tissues. It is mediated via high concentrations and uncontrolled distribution of pro-angiogenic factors like vascular endothelial growth factor (VEGF)-A. Consequently, tumor vessels often are unstructured and barely functional. Blood flow and oxygen supply are impaired, and the vessel wall is leaky (**Figure I6**, bottom right) (reviewed by De Bock et al., 2011).

Inhibition of the deregulated tumor angiogenesis is already used for treatment of various cancers (reviewed by Vasudev & Reynolds, 2014). The most commonly used drugs are VEGF/VEGF receptor inhibitors like bevacizumab (Avastin®), an anti-VEGF-A antibody (Roche Pharma AG, 2009). However, anti-angiogenic tumor therapy has double-edged sword character. High dose treatment has the potential to prune the tumor vasculature

and hinder the formation of new blood vessels in the primary tumor as well as in metastases. Thereby, high dose anti-angiogenic treatment limits nutrient supply to the tumor cells, which can lead to tumor cell death. However, it also creates an immunosuppressive tumor microenvironment and limits drug delivery as well as immune cell infiltration into the tumor tissue (**Figure I7**) (De Bock et al., 2011). As a result, the efficacy of most co-therapies apart from radiotherapy is decreased. Low dose anti-angiogenic treatment, on the other hand, can improve the functionality of the tumor vasculature (summarized in the concept of “vascular normalization”) (reviewed by Goel et al., 2011; R. K. Jain, 2005). At first glance, this improved tumor vessel function might even promote tumor growth. At the same time, however, vascular normalization is thought to improve drug and immune cell infiltration into the tumor tissue, which might increase the efficacy of co-therapies that are dependent on these parameters (**Figure I7**). This concept emphasizes that the dosage of anti-angiogenic drugs in cancer therapy should be specified depending on the respective goal and the type of co-therapy.

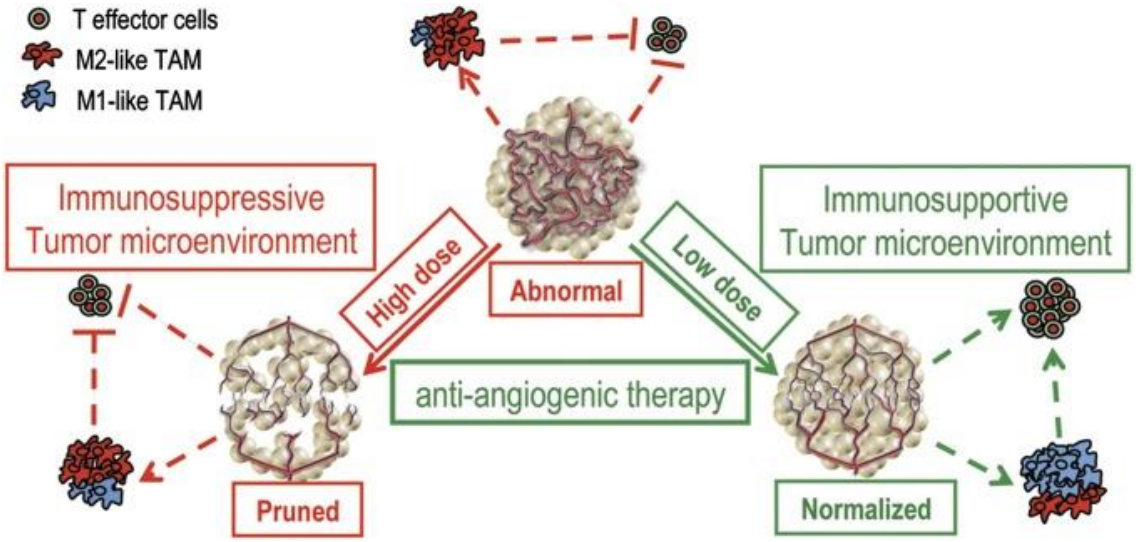

Figure I7: The “double-edged sword character” of anti-angiogenic therapy. Due to the high abundance of pro-angiogenic factors like VEGF-A, the tumor vasculature is abnormal consisting of unfunctional, disorganized, dilated and leaky vessels. This leads to a hypoxic, immunosuppressive tumor microenvironment containing primarily immune-inhibitory M2-like TAMs. High dose anti-angiogenic therapy prunes the tumor vasculature, cutting down nutrient supply and inducing local tumor cell death. However, it also increases hypoxia, restricts T cell infiltration, and still is immunosuppressive. Low dose anti-angiogenic therapy, on the other hand, normalizes the tumor vasculature and generates a more homogenous network of functional vessels. This promotes T cell infiltration and redirects TAMs to an immune-stimulatory M1 phenotype. Low dose anti-angiogenic therapy fails to induce tumor cell death on its own, but co-therapies, especially immunotherapy, might be supported by the improved tumor blood flow and microenvironment (taken from Y. Huang et al., 2012). TAM, tumor-associated macrophage.

1.3.5 cGMP in melanoma

Several studies have hinted towards an involvement of the cGMP signaling pathway in melanoma growth and progression: (1) Cohort studies have found a correlation between precedent sildenafil uptake and an increased risk for melanoma (W. Q. Li, Qureshi, et al., 2014), although subsequent meta-analysis could not deduce a causal relationship (Loeb et al., 2017). (2) Retrospective expression analysis of human melanoma material indicated that high cGKI expression in the tumor tissue correlates with a reduced 5-year survival (Dhayade et al., 2016). (3) Preclinical studies in mice observed a link between increased melanoma cell cGMP and accelerated tumor growth as well as increased invasion as detailed below (Arozarena et al., 2011; Dhayade et al., 2016).

The aforementioned preclinical studies by Arozarena et al. and Dhayade et al. have strongly improved our mechanistic understanding of cGMP's role in melanoma cells. Both studies independently observed a connection between cGMP and the growth-promoting MAPK signaling, which is known to play a pivotal role in melanoma development. The results indicated that increased MAPK signaling in melanoma cells inhibits PDE5, which increases the half-life of cGMP generated by GCs. Dhayade et al. (2016) have shown that melanoma cells express a functional CNP/GC-B/cGMP/cGKI pathway, which in turn stimulates the MAPK signaling cascade upstream of MAPK kinase. The authors concluded that melanoma cells contain a self-stimulating loop of MAPK and cGMP signaling (**Figure I8**). Consistently, Arozarena et al. and Dhayade et al. demonstrated with several pharmacological and genetic approaches (PDE5 inhibition with sildenafil, cGKI overexpression, and PDE5 overexpression) that upregulation of the cGMP pathway increases melanoma cell growth and migration *in vitro* as well as tumor growth and melanoma cell invasion *in vivo*, most likely via promotion of MAPK signaling.

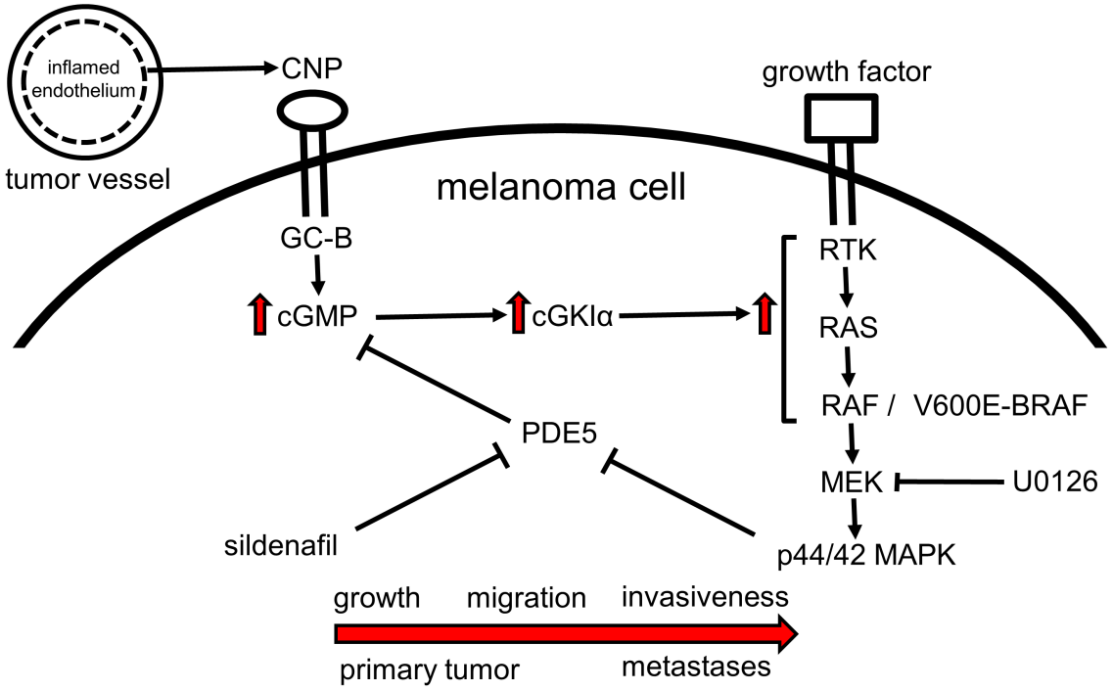

Figure I8: Model of the melanoma cells' cGMP signaling. Melanoma cells exclusively generate cGMP in response to CNP, which might be produced by the inflamed endothelium of tumor vessels. In melanoma cells, cGMP stimulates the MAPK pathway in a cGKI-dependent manner. This leads to inhibition of PDE5 expression and thereby even further elevates cGMP levels. This self-promoting loop of cGMP and MAPK signaling can be amplified by genetic (e.g., activating *BRAF/NRAS* mutation) or pharmacological (e.g., sildenafil) means and increases growth, migration and invasiveness of melanoma cells (taken from Dhayade et al., 2016)**.**

All the studies discussed above, however, focused on cGMP in the melanoma cells themselves. cGMP's effects during tumorigenesis on other structures and cells within the tumor stroma, i.e., blood vessels, tumor-infiltrating immune cells, and cancer-associated fibroblasts, remained less well-understood. Indeed, cGMP in other cell types was reported to have a cancer-protective role under certain conditions: (1) Stimulation of the cGMP pathway with the GC-C agonist linaclotide or the PDE5 inhibitor sildenafil reduced polyp formation from pre-neoplastic intestinal epithelium in a genetic mouse model of colorectal cancer (Sharman et al., 2018). (2) Using a *Ret*-transgenic melanoma mouse model, Meyer et al. (2011) described an anti-tumor effect of sildenafil. This effect was mediated via reduced NO production and immunosuppression by myeloid-derived suppressor cells and subsequent anti-tumor reactivity of $CD8^+$ T cells. Similar results were also obtained with syngeneic subcutaneous transplantation mouse models using colon carcinoma, mammary adenocarcinoma, and fibrosarcoma cells (Serafini et al., 2006). In contrast to

the study of Dhayade et al. (2016), Meyer et al. did not detect an effect of sildenafil on the tumor cells, most likely due to the lack of PDE5 expression in *Ret*-transgenic melanoma cells (Meyer et al., 2011) (reviewed by Umansky & Sevko, 2012). (3) Impairment of the perivascular NO gradient in melanoma with the NOS inhibitor N(G)-nitro-L-arginine methyl ester (L-NAME) inhibited the recruitment of perivascular cells towards the endothelium of tumor vessels and thereby impeded the establishment of a functional vascular network (Kashiwagi et al., 2005). Supporting the results from the melanoma study, restoration of the perivascular NO gradient in glioma by deletion of the glioma cells' NO production normalized the tumor vasculature (Kashiwagi et al., 2008). Since NO-GC was identified as the canonical NO receptor (see also 1.1.1), Kashiwagi et al. hypothesized that these NO effects on tumor perivascular cells are mediated via the NO-GC/cGMP cascade. Furthermore, they speculated that modulation of the perivascular NO signaling might provide a strategy for controlling tumor vessel structure and function, which could be utilized to potentiate anti-tumor therapies (see also 1.3.4).

Taken together, the role of cGMP in melanoma and other cancers appears to be diverse and varies between different cancer types and even cell types within the tumor. It might depend on the molecular mechanisms behind the respective cancer's development and progression. Therefore, a better understanding of where and under which conditions cGMP is generated within a tumor is necessary to enable precise manipulation of the tumor pathophysiology with cGMP-modulating drugs.

1.3.6 Melanoma mouse models

To allow for preclinical cancer research, several distinct mouse models have been developed over the years (Gould et al., 2015). These models include genetically engineered mice, xenotransplantation, and syngeneic transplantation. Genetic models utilize the fact that cancers are usually caused or driven by specific mutations. Advances in genetic engineering have made introduction of these mutations into the murine genome feasible. Combination with the Cre/loxP system (explained in 1.1.5) even enables cell type-specific and time-controlled induction of tumorigenesis. Dankort et al. (2009) have generated a genetic mouse model for melanoma. These mice carry the most common mutations in human melanoma, $Braf^{V600E}$ and $Pten^{-/-}$, controlled by the tyrosinase

promoter-driven 4-hydroxytamoxifen-inducible CreERT2 recombinase. Within a month after topical application of 4-hydroxytamoxifen to the skin, $BRAF^{V600E}$/$PTEN^{fl/fl}$/tyrosinase-CreERT2 mice form tumors that nicely reflect several aspects of human melanoma, including its metastasis pattern. Although these mice might be a good model for human patients carrying the respective mutations, the molecular mechanism of cancer development using a genetic approach severely limits the genetic heterogeneity that is usually observed in cancer.

Xenotransplantation models involve implantation of human tumor cells or tissues into experimental animals, i.e., mice. Naturally, these xenografts represent human cancer in the best possible way since samples can be collected from any desired spectrum of patients. However, the high immunogenicity of xenografts demands usage of immunodeficient mice which means that analysis or modulation of the anti-tumor immune response are not feasible with this approach. In addition, the method creates artificial contact sites between tissues of different species (i.e., human patient-derived tumor and murine host-derived stroma) (reviewed by Hammer, 1998).

Syngeneic transplantation, on the other hand, involves implantation of tumor cells or tissues into experimental animals, usually mice, of the same genetic background. Consequently, the host's immune response is rather low – most likely comparable to a natural anti-tumor immune response – resulting in an intact tumor microenvironment. The major drawback of this approach is that the genetic and phenotypic characteristics of murine cancer do not necessarily reflect the human disease (Overwijk & Restifo, 2001).

The most frequently used melanoma cell line for syngeneic transplantation in mice is the B16 cell line. These cancer cells originally were isolated from a spontaneously arisen melanoma in the ear of a C57BL/6 mouse in 1954. Shortly after, the B16 model evolved into a powerhouse of metastasis research. B16 cells subsequently isolated from metastases in these experiments were further maintained as increasingly aggressive variants. This was done for up to 10 inoculation cycles, culminating in the B16F10 cell line (Fidler, 1973, 1975). Experiments in the present study were carried out with B16F10 cells because syngeneic transplantation ensured an intact tumor microenvironment, and

the B16F10 model provided fast, reproducible tumor growth in mice with C57BL/6 background (i.e., cGMP sensor mice).

1.4 Aim of the work

What is already known? cGMP signaling is involved in a plethora of physiological processes including vascular relaxation, blood clotting, and cell growth and differentiation. Proteins of the cGMP pathway provide promising drug targets in many diseases. This has led to the development of a large line-up of cGMP-modulating drugs differing in their target proteins and cell types, as well as their molecular modes of action. Previous studies have demonstrated that among others, cGMP is involved in CKD and melanoma. However, our knowledge of the cellular and molecular mechanisms behind cGMP's actions within the kidney and melanoma is merely superficial.

What does this study add? Modern FRET-based cGMP live-cell imaging opens the door to analyze the cellular and molecular mechanisms of cGMP signaling in detail. In contrast to conventional cGMP immunoassays, cGMP biosensors allow us to follow cGMP generation in real time and in intact tissues *in situ*. This methodology has been combined with *in vitro* and *in vivo* approaches to analyze the role of cGMP in the kidney and in melanoma by addressing the following questions:

- Which cell types/structures generate cGMP in the respective tissues?
- Which GC ligands can induce cGMP generation in these cell types/structures?
- What is the physiological role of cGMP in these cell types/structures?
- Can particular drugs (i.e., NO-GC stimulators and activators) be utilized to modulate cGMP in the kidney and in melanoma?
- Do these drugs have certain preconditions (e.g., oxidative stress) for their action within the analyzed tissues?

Thus, the major aim of this study was to establish therapeutic indications of the cGMP signaling pathway as drug target in CKD and melanoma by analyzing the spatiotemporal changes of cGMP levels with cGMP biosensors as depicted above.

2 Materials and methods

In the following, all reagents, buffers and techniques used in the present study are described. The brands that are given for purchased materials can be matched with the corresponding companies in **Table S1**. Each protocol contains information about background and context of the respective technique, the required materials (listed under bullet points), and detailed instructions for the practical implementation (listed under capital letters). Percent values for preparation of solutions are given as weight/volume (w/v) in case of solid chemicals or as volume/volume (v/v) in case of liquids.

In general, solutions were prepared with H_2O from a Milli-Q® Biocel Water Purification System (Millipore; ≥ 18 MΩ.cm at 25 °C, total organic carbon value ≤ 5 ppb). Where specified, buffer pH was adjusted with 10 M and 1 M aqueous NaOH and HCl solutions. Whenever indicated, solutions were sterilized for 20 min at 121 °C with a DX-200 autoclave (Systec). Pipette tips, reaction tubes, and glass coverslips were sterilized under the same conditions. Centrifugation was performed with an Eppendorf 5417C/R centrifuge (1.5 ml and 2 ml tubes; Eppendorf) or an Eppendorf 5804R centrifuge (15 ml and 50 ml tubes; Eppendorf).

2.1 Common chemicals, reagents, and buffers

Table 1: Chemicals used in the present study.

Chemical	Brand	Chemical	Brand
Acetic acid	Sigma-Aldrich	KH_2PO_4	Merck
β-Escin	Sigma-Aldrich	2-Mercaptoethanol	Roth
6-Aminohexanoic acid	Roth	Methanol	Sigma-Aldrich
APS	Roth	$MgCl_2 \cdot 6H_2O$	Roth
Boric acid	CHEMSOLUTE	Milk powder	Roth
Bromophenol blue	Roth	Na_2HPO_4	Roth
$CaCl_2$, anhydrous	Roth	NaCl	Roth
cGMP	BiOLOG	NaH_2PO_4	Roth
Citric acid	Roth	$NaHCO_3$	Honeywell
$CuSO_4$, anhydrous	RanReac AplliChem	NaOH pellets	Roth
DMF	Roth	Nonidet P-40 substitute	Merck
DMSO	Roth	PFA	Roth
EDTA	Roth	Picric acid, 1.3 %	Sigma-Aldrich
Ethanol	Sigma-Aldrich	PMSF	Roth
D-Glucose	Fisher	SDS	Roth
Glycerol	Roth	Sodium citrate $\cdot 2H_2O$	Sigma-Aldrich
Glycine	Sigma-Aldrich	Sodium deoxycholate	Roth
H_2O_2	Roth	D-Sucrose	Roth
HCl, 37 % fuming	Roth	TEMED	Roth
HEPES	Roth	Tris (Trizma base)	Sigma-Aldrich
Isopropanol	Sigma-Aldrich	Triton X-100	Roth
$K_3Fe(CN)_6$	Merck	Trypan Blue, 0.4 %	GIBCO
$K_4Fe(CN)_6$	Roth	Tween-20	Roth
KCl	Sigma-Aldrich	Xylene cyanol	Roth

Footnotes: APS, ammonium persulfate; DMF, dimethylformamide; DMSO, dimethyl sulfoxide; EDTA, ethylenediaminetetraacetic acid; HEPES, 4-(2-hydroxyethyl)-1-piperazineethanesulfonic acid; PFA, paraformaldehyde; PMSF, phenylmethyl-sulfonyl fluoride; SDS, sodium dodecyl sulfate; TEMED, tetramethylethylenediamine.

- **cGMP-modulating drugs:**
    - Diethylamine NONOate (**DEA/NO**) diethylammonium salt (Axxora, CAS 372965-00-9) is an NO donor. Due to its short half-life time (~16 min at room temperature and pH 7.4), DEA/NO is well-suited to induce fast, transient cGMP increases during real-time cGMP imaging experiments. Store as 100 mM stocks in alkaline solution (10 mM NaOH in H_2O) at -20 °C and dilute in superfusion buffer immediately before application.
    - **ANP** (CAS 88898-17-3) and **CNP** (CAS 127869-51-6; both from Tocris) are peptide hormones. Store as 100 µM stock solutions in H_2O at -20 °C.
    - **BAY-41** (BAY 41-2272; Bayer, CAS 256376-24-6) (Stasch et al., 2001) and **riociguat** (BAY 63-2521; Sigma-Aldrich, CAS 625115-55-1) are NO-GC stimulators. **BAY-543** (Bayer) (Rühle et al., 2020), a close analog of runcaciguat, is a novel NO-GC activator. Store as 10 mM stock solutions in DMSO at -20 °C.

- 1H-[1,2,4]oxadiazolo[4,3-a]quinoxalin-1-one (**ODQ**; Axxora, CAS 41443-28-1) is an irreversible heme-site inhibitor of NO-GC. Store as 20 mM stock solution in DMSO at -20 °C.

- Dulbecco's modified eagle's medium (**DMEM**): DMEM high-glucose (4.5 g/l D-Glucose) GlutaMAX (containing the dipeptide L-alanyl-L-glutamine) +pyruvate (110 mg/l Na-pyruvate) (GIBCO, Cat-# 31966-021). If not stated otherwise, add 10 % fetal bovine serum (FBS; GIBCO, Cat-# 10270-106, Lot-# 41G6601K; heat-inactivated for 30 min at 57 °C), 100 U/ml penicillin and 100 µg/ml streptomycin (100x stock from GIBCO; Cat-# 15140122). Store at 4 °C.

- Imaging Buffer (**IB**): 140 mM NaCl, 5 mM KCl, 1.2 mM $MgCl_2$, 2 mM $CaCl_2$ and 5 mM HEPES in H_2O. Adjust pH to 7.4, autoclave and store at room temperature. Add 10 mM D-Glucose (from sterile-filtered 2.5 M stock) freshly before use.

- Phosphate-buffered saline (**PBS**): 135 mM NaCl, 3 mM KCl, 8 mM Na_2HPO_4 and 2 mM KH_2PO_4 in H_2O. Adjust pH to 7.4, autoclave and store at room temperature.

- **PBS-T:** 0.1 % Triton X-100 in PBS. Stir until dissolved and store at room temperature.

- Ringer bicarbonate buffer (**RBB**): 127 mM NaCl, 2.5 mM KCl, 0.5 mM $MgCl_2$, 1.1 mM $CaCl_2$, 20 mM D-Glucose, 1.1 mM NaH_2PO_4 and 26 mM $NaHCO_3$ in H_2O. Prepare freshly for each imaging session. Adjust pH by introducing carbogen gas (95 % O_2, 5 % CO_2; Mast) via gas frit 30 min before and during usage.

- Roswell park memorial institute (**RPMI**) 1640 medium: RPMI 1640 +L-glutamine (300 mg/l) +HEPES (6 g/l) (GIBCO, Cat-# 52400-025). If not stated otherwise, add 10 % FBS (GIBCO; Cat-# 10270-106, Lot-# 41G6601K; heat-inactivated for 30 min at 57 °C), 100 U/ml penicillin and 100 µg/ml streptomycin (100x stock from GIBCO; Cat-# 15140122). Store at 4 °C.

- **Tamoxifen** injection solution: 10 mg/ml tamoxifen (Sigma-Aldrich, CAS 10540-29-1) and 2 % ethanol in sunflower oil (THOMY). Pre-dissolve tamoxifen in ethanol (resulting in a turbid solution), then add sunflower oil to final volume. Ultrasonic at < 40 °C, until fully dissolved.

- Tris-buffered saline (**TBS**): 150 mM NaCl and 10 mM Tris in H_2O. Adjust pH to 8.0 and store at room temperature.

- **TBS-T:** 0.1 % Tween-20 in TBS. Stir until dissolved and store at room temperature.

- **Trypsin/EDTA:** 0.05 % trypsin and 0.5 mM EDTA (10x stock solution from GIBCO; Cat-# 15400-054) in PBS. Store for up to 3 months at 4 °C.

2.2 Melanoma cell culture

Although complex cell-to-cell interactions can only be studied in intact tissues and organisms, isolated primary cells and stable cell lines remain to be viable tools to analyze intracellular mechanisms without unnecessary interactions. In the present work, various cultured murine and human melanoma cell lines were characterized in terms of their cGMP signaling cascade on the molecular level. In addition, murine B16F10 melanoma cells were expanded in cell culture prior to their implantation into the mouse back skin for *ex vivo* and *in vivo* experiments.

B16F10 cells (kindly provided by Dr. Christoph Grießinger and Dr. Manfred Kneiling, Universitätsklinikum Tübingen) as well as genetically modified mCherry-expressing “red” (B16F10-R), amelanotic (B16F10-A) and amelanotic red (B16F10-AR) B16F10 clones together with their parental B16F10 cells (all kindly provided by Dr. Shweta Tikoo, Dr. Rohit Jain and Prof. Dr. Wolfgang Weninger, Medical University of Vienna) (Tikoo et al., 2021) were kept in DMEM. The human melanoma cell lines 1205Lu, A375, SKMel147, SKMel19, WM3211, WM35, WM852 and G361 were kindly provided by Prof. Dr. Meenhard Herlyn (The Wistar Institute, Philadelphia) or obtained from the American Type Culture Collection (ATCC) and cultured in RPMI medium. Both murine and human melanoma cells were cultured in a humidified CO_2 incubator (Heracell 150i, Fisher) at 37 °C and 6 % CO_2. Every two days, cells either received fresh medium (≤ 50 % confluence) or were passaged as specified below. Solutions were pre-warmed to 37 °C in a $CuSO_4$-supplemented WNB14 water bath (memmert). Sterile work was performed under a Herasafe KS18 clean bench (Thermo). Cells in culture were continuously monitored by eye and every few weeks, phase contrast pictures were recorded. The cell culture microscope setup consisted of an Axiovert 40C microscope (ZEISS) equipped with a halogen lamp for brightfield illumination, a long-distance condenser 0.2 with 3-position slider for brightfield and phase contrast microscopy, an air objective (LD A-Plan 20x/0.30; ZEISS) and a Cyber-shot DSC-W17 CCD (charge-coupled device) camera (SONY) with eyepiece adapter.

- Required **buffers** and chemicals: **PBS, DMEM** or **RPMI** medium (all pre-warmed to 37 °C), **Trypsin/EDTA,** and DMSO.

A. Wash cells 1x with PBS and detach them with trypsin/EDTA for 5 min at 37 °C and 6 % CO_2.

B. Stop the reaction by adding the respective medium (4x volume of the cell suspension), resuspend cells and centrifuge 5 min at 200 rcf at room temperature.

C. Discard supernatant and resuspend cell pellet in 1 ml medium per 12.5 cm^2 growth area. Seed cells in the desired density with splitting ratios of 1/3 to 1/15, depending on the cell line (see **Figure S2** for additional information).

D. Alternatively, add 10 % DMSO to the cell suspension from the previous step and prepare 1 ml aliquots.

E. Freeze aliquots in a Styrofoam box at -80 °C. After 24 h, transfer cells into liquid nitrogen for long-term storage.

F. Whenever needed, thaw frozen stocks quickly in a water bath at 37 °C. Pour over thawed cell suspension into 9 ml pre-warmed medium to dilute DMSO.

G. Centrifuge cells for 5 min at 200 rcf at room temperature, resuspend in fresh medium (without DMSO) and plate onto a T25 flask, if not indicated differently.

2.3 Transgenic mice

As indicated above, physiological processes cannot be analyzed with isolated cells because the conditions do not resemble the *in vivo* situation. A common approach to overcome this limitation is the use of animal models. The current study made use of transgenic mice that harbored knocked-in reporter genes and knocked-out genes of the cGMP pathway. These transgenic mice enabled localization and characterization of cell types with functional cGMP signaling within the studied tissues, as well as analysis of physiological consequences of altered cGMP signaling in these cells.

2.3.1 Animal ethics statement

All animal procedures were performed in accordance with the Directive 2010/63/EU, the German Tierschutz-Versuchstierverordnung, and the local authorities (Regierungs-präsidium Tübingen). Animal experiments involving injection of tumor cells (see 2.4) and, where applicable, tamoxifen (see 2.3.2) were approved as IB 3/18 and IB 02/19 G (“Rolle von cGMP und gekoppelten Signalwegen in Tumor- und Stromazellen im malignen Melanom”) by the local authorities. Mice used for kidney dissection (see 2.5.2.1) were covered by the report to the Regierungspräsidium Tübingen on November 25, 2016 (“Organentnahme bei Mäusen zur Analyse der cGMP Signaltransduktion (3)”).

2.3.2 Mouse lines

Mice were housed at 22 °C and 50-60 % humidity in a 12 h light / 12 h dark cycle with access to standard rodent chow (ssniff) and tap water ad libitum. Experimental animals were kept in groups of 3-6 mice per type III cage, and each cage was supplemented with a wooden tunnel, a plastic house, paper and standard wood bedding. Transgenic mice used in this study had been backcrossed on a C57BL/6NCrl (B6; charles river) genetic background for ≥ 10 generations. At an age of three weeks, mice were separated from their parents, ear-tagged, and genotyped as described in 2.3.3. All experiments were performed with 8-18-week-old mice with the genotypes detailed in **Tables 2 and 3**.

Table 2: Transgenic mouse lines used in the present study.

In-text name	Systematic name	Description	Ref.
B6	C57BL/6NCrl	Wildtype mice. All used mice were on B6 background.	[1]
cGi-L1	B6;129-Gt(ROSA)26Sor$^{tm1.1(ACTB-cGi500)Feil}$	Global expression of the cGMP biosensor cGi500.	[2]
mT/cGi-L2	B6;129-Gt(ROSA)26Sor$^{tm1(ACTB-tdTomato,-cGi500)Feil}$	Cre/loxP-controlled switch from mTomato to cGi500 expression.	[2]
SMA-CreERT2	B6-Tg(Acta2-cre/ERT2)51Pcn	CreERT2 expressed under control of the *Acta2* (SMA) promoter.	[3]
SM22-Cre	B6-Tg(Tagln-cre)1Her	Cre expressed under control of the *Tagln* (SM22) promoter.	[4]
CDH5-CreERT2	B6-Tg(Cdh5-cre/ERT2)1Rha	CreERT2 expressed under control of the *Cdh5* (CDH5) promoter.	[5]
TIE2-Cre	B6-Tg(Tek-cre)1Ywa	Cre expressed under control of the *Tek* (TIE2) promoter.	[6]
NO-GC$^{fl/fl}$	B6;129-Gucy1b3$^{tm1.2Frb}$	Floxed NO-GC gene for Cre/loxP-controlled NO-GC knock-out.	[7]
CNP-lacZ [11]	B6;129-Nppc$^{tm1.1Fgr}$	*lacZ* gene (β-gal.) knocked-in into the *Nppc*/CNP locus.	[8]
GC-B-lacZ [11]	B6;129-Npr2^{tm1Fgr}	*lacZ* gene (β-gal.) knocked-in into the *Npr2*/GC-B locus.	[9]
Ai14-L2	B6;129-Gt(ROSA)26Sor$^{tm14(CAG-tdTomato)Hze}$	Cre/loxP-controlled tdTomato expression.	[10]

Footnotes: Ref., first reference of respective mouse line; β-gal., β-galactosidase; [1]RRID:IMSR_CRL:027; [2]Thunemann, Wen, et al. (2013); [3]Wendling et al. (2009); [4]Holtwick et al. (2002); [5]Sorensen et al. (2009); [6]Kisanuki et al. (2001); [7]Friebe et al. (2007); [8]Schmidt et al. (2009); [9]Ter-Avetisyan et al. (2014); [10]Madisen et al. (2010); [11]Note that in heterozygous CNP-lacZ and GC-B-lacZ mice as used in the present study, the transgenic alleles do not lead to expression of functional CNP or GC-B protein. fl, flox.

Detailed information about cGi500 as well as the cGMP sensor mouse lines cGi-L1 and mT/cGi-L2 is given in 1.1.5. Briefly, cGi-L1 mice express the cGMP indicator cGi500 globally. In mT/cGi-L2 mice, cGMP sensor expression is controlled by the Cre/loxP

system. mT/cGi-L2, NO-GC$^{fl/fl}$ and Ai14-L2 mice in the present study were crossed with cell type-specific Cre mouse lines to obtain experimental animals with the desired "features". Some of the Cre mice used herein expressed the tamoxifen-inducible CreERT2 construct (model explained in 1.1.5). Experimental animals expressing CreERT2 were treated with 1 mg/d tamoxifen (tamoxifen injection solution is specified in 2.1) by intraperitoneal injection for 5 consecutive days at an age of 6 weeks, and (only in case of SMA-CreERT2) again at an age of ~10 weeks for 5 consecutive days, starting 5 days after implantation of B16F10 cells as described in 2.4. The genotypes and features of experimental animals obtained by intercrossing of several mouse lines are summarized in **Table 3**.

Table 3: Experimental animals investigated in the present study.

In-text name	Crossed mouse lines	Features
SMA-cGi	SMA-CreERT2 x mT/cGi-L2	Smooth muscle/pericyte-specific inducible expression of cGi500.
SM22-cGi	SM22-Cre x mT/cGi-L2	Smooth muscle/pericyte-specific expression of cGi500.
CDH5-cGi	CDH5-CreERT2 x mT/cGi-L2	Endothelial cell-specific inducible expression of cGi500.
TIE2-cGi	TIE2-Cre x mT/cGi-L2	Endothelial cell-specific expression of cGi500.
NO-GCsmko	SMA-CreERT2 x NO-GC$^{fl/fl}$ x mT/cGi-L2	Smooth muscle/pericyte-specific inducible NO-GC knock-out and cGi500 expression.
NO-GCctrl	SMA-CreERT2 x NO-GC$^{fl/wt}$ x mT/cGi-L2	Heterozygous control for NO-GCsmko* and smooth muscle/pericyte-specific inducible cGi500 expression.
SMA-Ai14	SMA-CreERT2 x Ai14-L2	Smooth muscle/pericyte-specific inducible expression of tdTomato.

Footnotes: *Recombined cells in NO-GCctrl mice carry one functional and one defective NO-GC allele. fl, flox; wt, wildtype.

Cell type-specificity of Cre-mediated recombination in tumors and efficiency of NO-GCsmko in experimental animals were validated via immunofluorescence (IF) staining (**Figures S6, S7 and S8**) and Western Blot (**Figure S9**), respectively.

2.3.3 Genotyping

When using transgenic mice as a model, the genetic status of experimental animals must be carefully monitored. Incorrect assignment of a certain genotype can lead to misinterpretation of the acquired data. For this reason, the genotype of all experimental

animals with regard to the genes of interest was determined at the age of three weeks, and again verified after termination of the experiment wherever applicable.

Genotyping was performed with polymerase chain reaction (PCR) according to the protocol listed below. In all cases, the primer design made it possible to distinguish between wildtype and transgene conditions. This could either be deduced from differences between the sizes of amplified DNA fragments or by the absence of a DNA fragment in wildtype or transgenic animals (see also **Table 4**).

- **DNA extraction buffer:** 1 mg/ml proteinase K (Genaxxon, CAS 39450-01-6) in 1x “complete II KCl” reaction buffer (from 10x stock solution, BIORON).
- **BIORON master mix:** 10 mM Tris (pH 8.3), 50 mM KCl, 1.5 mM $MgCl_2$, 0.2 mM of each deoxynucleotide (NEB, Cat-# N0446S), 0.3 µM of each primer (see **Table 4**) and 0.04 U/µl DFS-*Taq* DNA polymerase (BIORON, Cat-# 101100; final concentrations are given).
- **invitrogen master mix:** 20 mM Tris (pH 8.4), 50 mM KCl, 1.5 mM $MgCl_2$ (all provided with invitrogen *Taq* DNA pol.), 0.2 mM of each deoxynucleotide (NEB, Cat-# N0446S), 0.3 µM of each primer (see **Table 4**) and 0.05 U/µl recombinant *Taq* DNA polymerase (invitrogen, Cat-# 10342-020; final concentrations).
- **Tris-borate-EDTA (TBE) buffer:** 50 mM Tris, 50 mM boric acid and 1 mM EDTA in H_2O. Store at room temperature.
- **6x DNA loading dye:** 30 % glycerol, 0.05 % bromophenol blue and 0.05 % xylene cyanol in TBE. Concentrations correspond to the 6x stock solution that is used in this protocol. Store at -20 °C.
- **Tris-acetate-EDTA (TAE) buffer:** 40 mM Tris, 20 mM acetic acid and 1 mM EDTA in H_2O. Store at room temperature.
- Other **buffers** and chemicals: HPLC-grade H_2O (Fisher, CAS 7732-18-5), LE Agarose (Biozym), Midori Green Advance (NIPPON Genetics, Cat-# MG04) and 1 kb Plus DNA Ladder (invitrogen, Cat-# 10787-018).

A. Collect ear biopsies of experimental animals (~0.8 mm^3) in 1.5 ml tubes during ear-tagging. Digest tissue in 50 µl DNA extraction buffer overnight at 57 °C.

B. The next day, briefly vortex tissue lysates, centrifuge for 5 min at 18000 rcf and transfer DNA-containing supernatants into fresh tubes.

C. Heat-inactivate proteinase K for 15 min at 95 °C in a peqSTAR 2X (PEQLAB) thermal cycler. Store DNA samples at -20 °C or immediately continue with PCR.

D. Prepare BIORON or invitrogen master mix (depending on transgene; see **Table 5**). Add 23 µl master mix to 2 µl DNA sample from the previous step, mix and spin down briefly. *Important: Keep samples on ice from here.*

E. Run PCR program in a Biometra TAdvanced (Biometra) thermal cycler. A generic PCR program is provided here:

95 °C, 5 min		Initial denaturation
35 ↻	T_d	Denaturation
	T_a	Annealing
	T_e	Extension
72 °C, 5 min		Final extension
8 °C, ∞		Hold condition

T_d, T_a and T_e values and related incubation times are given in **Table 5**. After PCR program, add 5 µl 6x DNA loading dye.

F. For separation of DNA bands, dissolve 2 % agarose in TAE buffer. To help this process, heat up the solution for ~2 min in a microwave until it is clear.

G. Cool down agarose gel for ~1 min under tap water, add 0.003 % Midori Green Advance and pour gel into a chamber of the BioMax MP1015 Horizontal Gel Electrophoresis System (Kodak). Let gel solidify for ≥ 30 min.

H. Load 12 µl DNA sample or 8 µl 1 kb Plus DNA Ladder containing DNA loading dye per pocket of the solidified agarose gel. Separate bands for 5 min at 50 V followed by ~35 min at 100 V (PowerPac 300, Bio-Rad).

I. Detect DNA under UV light with the “GelGreen” setting of a ChemiDoc Imaging System (Bio-Rad).

Table 4: Genotyping primers used in the present study.

Transgene	Primer name	Sequence (5’ → 3’)	Band size
cGi-L1 & mT/cGi-L2	BB01 (fwd)	CTC TGC TGC CTC CTG GCT TCT	wt: 322 bp tg: 249 bp
	BB02 (wt rev)	CGA GGC GGA TCA CAA GCA ATA	
	BB03 (ko rev)	TCA ATG GGC GGG GGT CGT T	
Cre & CreERT2	Cre800 (fwd)	GCT GCC ACG ACC AAG TGA CAG CAA TG	wt: none tg: 402 bp
	Cre1200 (rev)	GTA GTT ATT CGG ATC ATC AGC TAC AC	
NO-GC flox & NO-GC ko	BB19 (fwd)	AAG ATG CTG AAG GGA AGG ATG C	wt: 680 bp fl: 720 bp ko: 830 bp
	BB20 (wt rev)	CAG CCC AAA GAA ACA AGA AGA AAG	
	BB21 (ko rev)	GAT GTG GGA TTG TTT CTG AGG A	
CNP-lacZ	P1 (fwd)	AAG ATG ACA TCA GCG GCA G	wt: 393 bp tg: 347 bp
	P2 (wt rev)	GCT TTG AGG GAG CAA GTC C	
	P3 (ko rev)	CCT CTT CGC TAT TAC GCC AG	
GC-B-lacZ	BB22 (fwd)	TGC CAC CCT ATC CTT AGT CC	wt: 348 bp tg: 398 bp
	BB23 (wt rev)	GTG TTC TGG CAG CAC CAC	
	BB24 (ko rev)	TCG CTA TTA CGC CAG CTG	

Footnotes: Primers are divided into forward (“fwd”; binds to the template strand) and reverse (“rev”; binds to the coding strand) primers. The last column lists predicted band sizes and if PCR products are generated from wildtype (wt), transgenic (tg), floxed (fl) or knock-out (ko) alleles. Primers were obtained from eurofins and stored as 25 µM stocks in HPLC-grade H_2O. bp, base pairs.

Table 5: T_d, T_a and T_e values and related incubation times of PCR programs performed herein.

Transgene	T_d value, time	T_a value, time	T_e value, time	Master mix
cGi-L1 & mT/cGi-L2	95 °C, 10 s	61 °C, 30 s	72 °C, 30 s	BIORON
Cre & CreERT2	95 °C, 10 s	58 °C, 30 s	72 °C, 30 s	BIORON
NO-GC flox & ko	95 °C, 60 s	60 °C, 45 s	72 °C, 60 s	invitrogen
CNP-lacZ	95 °C, 30 s	60 °C, 25 s	72 °C, 25 s	invitrogen
GC-B-lacZ	95 °C, 30 s	57 °C, 30 s	72 °C, 30 s	invitrogen

Footnotes: T_d, temperature of denaturation cycle; T_a, temperature of annealing cycle; T_e, temperature of extension cycle.

2.4 Intradermal implantation of B16F10 cells

Today, we have access to many animal models mimicking human diseases including melanoma, which allows us to study the development and progression of these diseases within a close-to-native environment. These disease models can also be combined with transgenic models to analyze the role of specific genes/proteins and pathways in the respective diseases.

Here, the syngeneic B16F10 melanoma mouse model (background information is given in 1.3.6) was used. Murine B16F10 melanoma cells were transplanted by intradermal injection into the mouse back skin of 8-18-week-old immunocompetent B6 mice. This methodology had four key advantages in the context of this work: (1) The melanoma microenvironment was mimicked in a close-to-native manner. Tumor cells were injected into the skin as their natural environment, and immunocompetent mice were used as hosts that enabled tumor immune cell infiltration. (2) The cGMP signaling pathway in B16F10 cells had been characterized previously, so that the present study could focus on components of the tumor stroma. (3) B16F10 tumor growth was reasonably fast and reproducible, thus limiting the variability of parameters like tumor size and tumor weight as measure for pathophysiological characteristics of melanoma development. (4) B16F10 cells, much like GMP sensor mice, were on a B6 genetic background, enabling their syngeneic transplantation for cGMP imaging in cells of the tumor stroma. Other melanoma mouse models demanding the use of immunodeficient mice (xenotransplantation) or a melanocyte-specific Cre mouse line (many melanoma models based on genetic engineering) would not have been feasible for these experiments (see also 1.3.6).

- Required **buffers** and chemicals: **PBS, Trypsin/EDTA, DMEM**, trypan blue and isoflurane (cp-pharma).

A. Thaw and culture B16F10 cells as described in 2.2. At a density of 60-80 %, continue with the steps detailed below. 75 cm^2 growth surface area are sufficient for ~30 injections (15 mice). From here, avoid vortexing as B16F10 cells are susceptible to physical stress.

B. Wash cells 1x with PBS and detach them with trypsin/EDTA for 5 min at 37 °C and 6 % CO_2.

C. Stop the reaction by adding DMEM (4x volume of the cell suspension), resuspend cells and centrifuge 5 min at 200 rcf at room temperature.

D. Discard supernatant, wash cells 2x with PBS and resuspend them in 200 µl PBS per 75 cm^2 growth surface area.

E. Take 2 µl cell suspension, add trypan blue (0.04 % final concentration) to stain dead cells, and fill up to 20 µl with PBS. Count the (non-stained) living cells using a Neubauer improved chamber (MARIENFELD).

F. Dilute B16F10 suspension to $3.75 \cdot 10^6$ cells/ml with PBS and prepare 0.5 ml aliquots. Keep cells in a tube rotator (neoLab, Cat-# 2-1175) at room temperature to ensure uniform distribution during the injection process.

G. Anesthetize mouse with 5 % isoflurane in O_2 with the anesthesia unit "RESEARCH" (Eickemeyer, Cat-# 213087). Lower isoflurane concentration to 2 % as soon as anesthesia occurs. Before continuing, validate anesthesia via toe pinch reflex.

H. Carefully shave both flanks of the mouse with an electric shaver. Avoid afflicting damage to the skin, since scar formation can affect tumor growth.

I. 20 µl ($7.5 \cdot 10^4$ B16F10 cells) are administered by intradermal injection into each shaved flank with an Omnican 50 syringe (B. Braun; one indicator equals 0.1 units of insulin or 10 µl) as shown here:

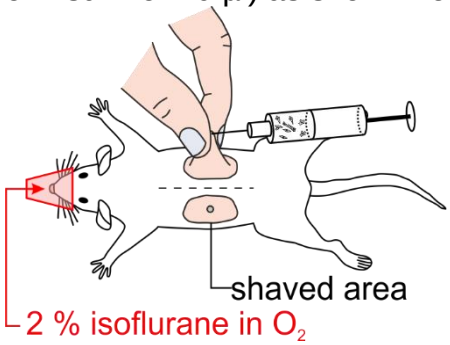

Note: Intradermal injection requires a very shallow entry angel and can be validated by wheal formation. *Important: Make a note in case no wheal forms or liquid exits the injection site.*

J. Monitor mouse until it awakes from anesthesia. This usually occurs within a few minutes. If not, keep mouse warm and get help from veterinary personnel.

After intradermal implantation of B16F10 cells, tumor size (and ulceration, where applicable) as well as animal weight and condition (i.e., coat care, breathing, movement and social interaction) were monitored daily. A 0-150 mm digital precision caliper was used to determine the tumor's largest diameter d_1 and its orthogonal diameter d_2. Based on these values, the tumor volume was calculated based according to the formula $V = \frac{1}{6}\pi \cdot {d_1}^2 \cdot d_2$. Animals that prematurely reached the termination criteria (i.e., tumor with $d_1 \geq 15$ mm, tumor ulceration, weight loss ≥ 20 % during the experiment or strange behavior) were immediately euthanized and excluded from the experiment.

2.5 FRET-based cGMP imaging

The FRET-based cGMP biosensor cGi500 (Russwurm et al., 2007) is widely used to visualize cGMP concentration changes in living samples (see 1.1.5 for a detailed description of cGi500's working principle). Briefly, cGi500 consists of the tandem cGMP binding domain of cGKI flanked by CFP (FRET donor) and YFP (FRET acceptor). In basal state (i.e., when [cGMP] is low), FRET takes place between the two fluorophores. Binding of cGMP (i.e., high [cGMP]) induces a conformational change that decreases the FRET efficiency. Therefore, the CFP/YFP ratio correlates with the local cGMP concentration.

cGi500 has proved useful in many *in vitro*, *ex vivo* and *in vivo* applications (R. Feil et al., 2021), since its properties make it well-suited to detect cGMP changes in a broad range of cell types including smooth muscle cells (Thunemann, Wen, et al., 2013). To measure cGMP in real time in the present study, either cultured cells were transfected with a cGi500 expression vector (see 2.5.1), or tissues were isolated from transgenic mice expressing cGi500 globally or in distinct cell types (see 2.3.2).

2.5.1 Transfection of cells

Transfection is an easy-to-use yet powerful method to introduce genes (e.g., reporter genes) into cultured cells, which only requires the respective expression vector. Here, the melanoma cell lines listed in 2.2 were transiently transfected by lipofection with a eukaryotic expression plasmid encoding cGi500 under control of the strong ubiquitous

cytomegalovirus (CMV) promoter (pCMV-cGi500; vector card given in **Figure S1**) as detailed below. Subsequently, cGMP generation in response to cGMP-modulating drugs could be monitored in real time in the transfected cells (see 2.5.3).

- Required **buffers** and chemicals: **PBS, Trypsin/EDTA, DMEM** or **RPMI** medium, trypan blue and GenaxxoFect Transfection Kit (containing GenaxxoFect and dilution buffer; GENAXXON, Cat-# M3053).

A. Thaw and culture cells as described in 2.2.

B. When splitting, count cells after resuspension in medium following their detachment with trypsin. To do so, take 2 µl cell suspension, add trypan blue (0.04 % final concentration) to stain dead cells, and fill up to 20 µl with PBS. Count the (non-stained) living cells using a Neubauer improved chamber (MARIENFELD). Seed $1.5 \cdot 10^4$ cells per well in a 24-well-plate supplemented with 12 mm-coverslips.

C. At a confluence of 30-50 %, prepare transfection solutions A (0.3 µg pCMV-cGi500 plasmid DNA in 40 µl dilution buffer; vortex thoroughly) and B (2 µl GenaxxoFect in 40 µl dilution buffer; vortex thoroughly). Mix solutions A and B, vortex thoroughly and incubate 30 min at room temperature.

D. Aspirate the medium and add 350 µl fresh medium to the cells that shall be transfected. Dropwise, add 80 µl of the combined transfection solution (A+B) per 24-well and distribute by carefully moving the plate in circular motion.

E. Incubate cells at 37 °C and 6 % CO_2. After 18 h, aspirate the transfection solution and add fresh medium. Allow cells to grow for 1-2 additional days until they reach a density of 70-80 %.

F. Serum-starve cells with FBS-free medium for 18-30 h prior to the imaging experiment to synchronize the cell cycle and to prevent stimulation of the cGMP pathway by serum factors.

2.5.2 Preparation of vital kidney and tumor slices

If cells shall be analyzed in a close-to-native environment, acutely isolated tissues have several key advantages over cultured cells: Using intact tissues preserves information on the localization of cells within the examined tissue, maintains the native cell-to-cell interactions, and prevents the genetic and phenotypic drift that is frequently associated with cell culture (Ben-David et al., 2018; Rensen et al., 2007). In the present study, this approach was used to visualize cGMP *in situ* in the kidney and in melanoma. To do so, kidneys and primary B16F10 tumors were isolated from cGMP sensor mice and acutely sliced as explained in the following subsections.

2.5.2.1 Preparation of kidney slices

- **Dissecting set:** Dumont #5 straight forceps, Dumont #7 curved forceps, Adson forceps (Cat-# 1106-12), Student Surgical Scissors (Cat-# 91402-12; all from F·S·T).

- Required **buffers** and chemicals: CO_2 (Mast), 70 % ethanol, **RBB** and superglue (Pattex, Cat-# 1866689).

A. Euthanize mouse with CO_2 followed by cervical dislocation. Disinfect abdominal fur with 70 % ethanol to prevent contamination and carryover of dry hair.

B. Open abdominal cavity along the linea alba. Move liver and gastrointestinal tract to the side so that kidneys are accessible.

C. Grab renal pelvis with Adson forceps and carefully cut connections to the mesentery as well as renal artery, renal vein, renal nerve, and the ureter. Avoid damaging the soft renal tissue. Store isolated whole kidneys in ice-cold carbogen-gassed RBB. cGMP imaging must be performed within 8 h after isolation of the whole kidneys.

D. Before sectioning, remove renal capsule by carefully pulling with two fine (Dumont) forceps from different directions. Transfer kidney into fresh RBB.

E. Glue the kidney with its dorsal side onto the tape-covered specimen plate of a VT1200 vibratome (Leica) with superglue. Allow glue to solidify and transfer specimen plate into buffer tray filled with ice-cold RBB.

F. Prepare 700 µm slices at a speed of 0.3 mm/s and an amplitude of 1.1 mm (cutting plane is depicted in **Figure S3**). Transfer kidney slices into ice-cold carbogen-gassed RBB using a spatula to avoid tissue damage. After slicing of kidneys, cGMP imaging must be performed within 4 h.

2.5.2.2 Preparation of tumor slices

- **Dissecting set:** Adson forceps (Cat-# 1106-12), Student Surgical Scissors (Cat-# 91402-12); both from F·S·T.

- Required **buffers** and chemicals: CO_2 (Mast), 70 % ethanol, **PBS**, hair removal cream (Veet), **IB** and superglue (Pattex, Cat-# 1866689).

A. Euthanize tumor-bearing mouse with CO_2 followed by cervical dislocation. Disinfect skin around tumors with 70 % ethanol, and wipe with PBS.

B. Remove hair on and around tumors with electric shaver and hair removal cream. Wipe off hair removal cream thoroughly with PBS after ~1.5 min. *Attention: Prolonged incubation can irritate the murine skin.*

C. Grab skin next to tumor with Adson forceps, and remove tumor with some surrounding skin. Store isolated whole tumors in ice-cold IB. cGMP imaging must be performed within 8 h after isolation of the whole tumors.

D. Glue tumor with its proximal side onto the tape-covered specimen plate of a VT1200 vibratome (Leica) with superglue. Allow glue to solidify and transfer specimen plate into buffer tray filled with ice-cold IB.

E. Prepare 700 µm slices at a speed of 0.3 mm/s and an amplitude of 1.1 mm (cutting plane is depicted in **Figure S3**). Transfer tumor slices into ice-cold IB by grabbing the surrounding skin to avoid damage of soft tumor tissue. After slicing of tumors, cGMP imaging must be performed within 3 h. Exchange blade after each tumor.

2.5.3 Imaging of cells and tissues

FRET-based cGMP imaging was performed as described previously (Thunemann, Fomin, et al., 2013) (**Figure I9**). The setup for cultured cells consisted of an Axiovert 200 (ZEISS)-based system equipped with a computer-controlled xenon short-arc lamp with electronic shutter (Oligochrome, TILL Photonics), a HAL 100 light source for brightfield illumination (ZEISS), a long-distance condenser 0.35 with DIC/Senarmount slider for brightfield, phase contrast and differential interference contrast microscopy, a 1.0/1.6x Optovar lens and a fluorescence-grade air objective (EC Plan-NEOFLUAR 10x/0.3; ZEISS). YFP fluorescence of cGi500 was detected through a filter set consisting of a 497/16 nm excitation filter, a 516 nm dichroic mirror, and a 535/22 nm emission filter. For FRET-based cGMP imaging, the donor fluorophore CFP was excited at 445/20 nm, and a Dual-View beam splitter (Photometrics) with a 516 nm dichroic mirror as well as 480/50 nm and 535/40 nm emission filters was used for simultaneous acquisition of CFP and YFP fluorescence. Signals were recorded with an electron-multiplying charge-coupled device (EM-CCD) camera (Retiga R1, QImaging) at a frame rate of 0.2 Hz and an exposure time of 300 ms.

Tissue samples were examined with a microscope system consisting of an upright Examiner.Z1 (ZEISS), a Yokogawa CSU-X1 spinning disk confocal scanner (YOKOGAWA), three diode lasers (445 nm, 488 nm and 561 nm), three water immersion objectives (W N-ACHROMAT 10x/0.3, W Plan-APOCHROMAT 20x/1.0 DIC (UV) VIS-IR, W Plan-APOCHROMAT 40x/1.0 DIC VIS-IR; all from ZEISS) and one air objective (EC Plan-NEOFLUAR 2.5x/0.085; ZEISS). mCherry and mT fluorescence were detected with a CCD camera (SPOT Pursuit, SPOT Imaging) through the quad band laser clean-up filter ZET/405/488/561/635M (CHROMA) after excitation with the 561 nm laser. Similarly, YFP fluorescence of cGi500 was detected with the SPOT Pursuit camera through a

525/50 nm emission filter after excitation with the 488 nm laser. For FRET-based cGMP imaging, the donor fluorophore CFP was excited with the 445 nm laser, and a Dual-View beam splitter (Photometrics) with 505 nm dichroic mirror, 470/24 nm and 535/30 nm emission filters was used for simultaneous acquisition of CFP and YFP. Signals were recorded with an EM-CCD camera (QuantEM 512SC, Photometrics) at a frame rate of 0.2 Hz and an exposure time of 200 ms.

Both cultured cells and isolated murine tissues were continuously superfused, either with IB in case of cultured cells and tumor slices or with carbogen-gassed RBB in case of kidney slices. Although cGMP imaging in kidney slices in principle also was possible using IB, the renal tissue appeared to retain more of its integrity when kept in RBB. Superfusion was done with or without drugs of interest at a flow rate of 1 ml/min at room temperature. The custom-built superfusion system (see also **Figure I9**) consisted of a fast protein liquid chromatography (FPLC) pump (Pharmacia P-500, GE Healthcare), FPLC injection valves (Pharmacia V-7, GE Healthcare), a magnetic platform (Warner Instruments), a superfusion chamber (RC-26, Warner Instruments) and sample loops of different sizes (7 ml for ODQ; 2 ml for other drugs). Tissue slices were pinned down with a mesh-assisted Slice Hold-Down (SHD-26H/10, Warner Instruments). To ensure that drug exposure was comparable between different imaging sessions, the same drug volumes were applied for the same time span. A vacuum pump with adjustable vacuum (Laboport N86, KNF Neuberger) was connected to the system to constantly remove excess buffer. A detailed FRET/cGMP imaging protocol is given below.

A. Calibrate beam splitter for optimal CFP-YFP-alignment, if necessary.
B. Equilibrate superfusion system including FPLC pump, injection valves, and all required loops with the respective buffer (i.e., IB or RBB) for 10 min at 5 ml/min.
C. Obtain living, cGi500-expressing samples via transfection of cultured cells (see 2.5.1) or extraction of tissues from cGMP sensor mice (see 2.5.2).
D. Assemble superfusion chamber containing the cell or tissue sample (see **Figure I9**). Apply buffer as soon as possible to prevent the samples from drying.
E. Connect chamber to superfusion system and start superfusion. Adjust aspiration needle until buffer flow and liquid level in the chamber are constant.

F. Identify a suitable field of view using the YFP filter set. Important criteria include:

   - **Cells:** cGi500 expression (low expression leads to poor signal-to-noise ratio, whereas overexpression might interfere with cellular signaling; intermediate expression usually is preferable), cell density (avoid under- and over-confluent areas), and cell viability (exclude dead cells, which can be identified via their round shape or the presence of apoptotic bodies).

   - **Tissue slices:** Anatomic structure (look for and focus on structures of interest, i.e., glomeruli or tumor vessel), fluorescence intensity and blurriness (both get worse with imaging depth; superficial imaging usually works best), and tissue integrity (avoid damaged tissue, which can be identified via floating cells and tissue pieces).

G. Assign regions of interest that account for cellular/structural heterogeneity. Monitor FRET changes during the recording. Make sure to assign several regions of interest since cGMP signaling might differ between various cells and structures.

H. Adjust camera (binning, gain), light source (intensity) and image acquisition (exposure time, frame rate) settings as desired. Avoid saturation of pixels since their intensity is not quantitatively assessed.

I. Record baseline CFP and YFP intensities for at least 3 min at the beginning of each individual experiment.

J. Freshly dilute drugs of interest to their final concentration in IB or RBB, and apply solutions via sample loops. When evaluating FRET/cGMP signals, consider that drugs reach the sample with some delay due to the system's dead volumes.

K. Between individual drug applications, make sure that the CFP/YFP ratio is back at baseline by closely monitoring live signal traces and flush sample loops 2x with IB or RBB. If necessary, correct for focus drift.

L. After the last drug application, take additional images (e.g., brightfield pictures, red fluorescence, z-stacks). This order of events limits photobleaching prior to the FRET/cGMP measurement.

M. Switch off superfusion, remove sample, disassemble superfusion chamber and flush superfusion system with 20 % ethanol. Wipe objectives with water.

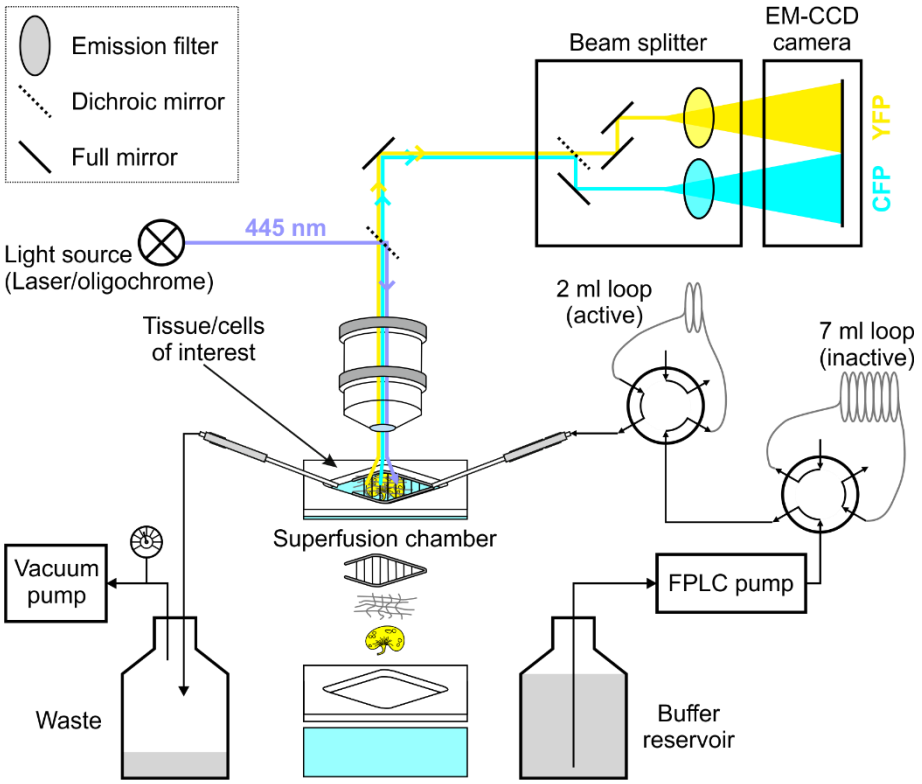

Figure I9: Microscope setup for *in situ* cGMP visualization in cells and tissues. Cells and tissue slices are placed in a superfusion chamber (exploded and condensed view are shown). During the measurement, samples are continuously superfused with a system consisting of an FPLC pump, two sample loops of different sizes and a vacuum pump that continuously aspirates excess buffer. To visualize cGMP, CFP is excited at 445 nm, and CFP as well as YFP epifluorescence are detected simultaneously using a beam splitter. This device separates CFP and YFP emission with a dichroic mirror and guides the light through the respective emission filter onto two predefined regions of the same EM-CCD camera. If all mirrors are properly aligned, CFP and YFP fluorescence will be depicted on the same pixel in the resulting pictures.

2.5.4 Image analysis and quantification of cGMP concentration changes

Online image acquisition was performed with the VisiView software (Visitron). As detailed in the protocol below, offline post-processing and analysis were performed with the Fiji software (RRID:SCR_002285) (Rueden et al., 2017; Schindelin et al., 2012) followed by further evaluation with Excel (RRID:SCR_016137; Office 16; Microsoft) and Origin 2019 (RRID:SCR_014212; OriginLab).

A. Align image stacks in x/y dimension using the Fiji plugin MultiStackReg v1.45 (RRID:SCR_016098) to correct for sample movement, if necessary.

B. *Only for cultured cells:* Correct CFP and YFP intensities for background fluorescence. This is not feasible with tissue slices, as these often cover the whole flied of view during image acquisition, thereby not leaving a background region.

C. Calculate the CFP/YFP ratio (black traces in the respective graphs; referred to as “R (cGMP)”). R (cGMP) correlates with the cGMP concentration.

D. Normalize CFP and YFP intensity as well as R (cGMP) to the baseline recorded at the beginning of each experiment to account for differences in the basal fluorescence between individual samples.

E. Smooth R (cGMP) traces according to the Savitzky-Golay filtering method. *Attention: Excessive smoothing can affect the signal shapes. Usually, smoothing windows of 10-30 points are appropriate, depending on the signal-to-noise ratio.*

F. Perform an additional baseline correction accounting for baseline drift during the measurement (e.g., due to photobleaching or focus drift), if necessary.

G. Calculate the area under the curve (AUC) and the peak height (relative R (cGMP) change) for each signal using the “Peak Analyzer” tool of Origin.

2.6 Preparation and analysis of protein samples

Although analysis of (phospho-)proteins in cell and tissue lysates does not have single-cell resolution, it is a highly quantitative and sensitive tool to determine differences in protein expression and phosphorylation between experimental groups. In the present study, protein extracted from cultured melanoma cells and tissue samples was examined via SDS-polyacrylamide gel electrophoresis (SDS-PAGE) followed by Western Blot. This methodology was used to characterize the expression of cGMP cascade proteins and cGMP-dependent protein phosphorylation in different melanoma cell lines, and to validate the smooth muscle/pericyte-specific NO-GC knock-out in NO-GCsmko mice.

2.6.1 Protein extraction from cells and tissues

Generally, protein was extracted from cultured cells (2.6.1.1) and isolated tissues (2.6.1.2) using harsh SDS-containing lysis buffers. Milder lysis buffers containing non-ionic detergents or low SDS concentrations were shown to solubilize membranes and proteins incompletely (Browning, 2012; Sefton, 2001). Under circumstances specified below, such a mild “permeabilization buffer” from the Mem-PER Plus Kit was used to remove cytosolic proteins prior to membrane protein extraction with a harsh “solubilization buffer” from the same kit. PMSF or protease inhibitor cocktail were added to inhibit cellular proteases.

2.6.1.1 Protein extraction from cultured cells

- **Cell lysis buffer:** 21 mM Tris pH 8.3, 0.67 % SDS and 0.2 mM PMSF in H_2O. *Attention*: *Composition differs from SDS lysis buffer for tissues.*

- Other **buffers** and chemicals: **DMEM** or **RPMI** medium.

A. Grow cells to a confluence of 60-80 % as described in 2.2.

B. Wash cells 2x with FBS-free medium. After last washing step, aspirate the medium and add 1 ml cell lysis buffer per 10 cm dish. Detach cells with a cell scraper (BIOLOGIX, Cat-# 70-1250). Transfer viscous lysate into a 1.5 ml tube.

C. Immediately denature protein for 10 min at 95 °C in a Thermomixer compact (Eppendorf). Centrifuge 5 min at 18000 rcf at 4 °C. Transfer protein-containing supernatant into new tube.

D. Store protein at -20 °C or immediately continue with protein quantification and SDS-PAGE.

For Western Blot detection of GC-B in B16F10 cells (**Figure 4C**), membrane proteins (including GC-B) were enriched using the Mem-PER Plus Membrane Protein Extraction Kit (Thermo) as per the manufacturer's recommendation:

- Required **buffers** and chemicals: **DMEM,** Mem-PER Plus Kit (Thermo, Cat-# 89842; including washing solution, permeabilization buffer, and solubilization buffer), cOmplete Mini Protease Inhibitor Cocktail (Roche, Cat-# 04693124001).

A. Grow cells to a confluence of 60-80 % as described in 2.2.

B. Wash cells 1x with FBS-free DMEM and 1x with washing solution. Add 0.5 ml permeabilization buffer per 2x10 cm dish B16F10 cells. Carefully detach cells with a cell scraper (BIOLOGIX, Cat-# 70-1250) and transfer into a 1.5 ml tube.

C. Incubate 10 min at 4 °C in a tube rotator (neoLab, Cat-# 2-1175). Centrifuge 15 min at 16000 rcf at 4 °C. Transfer supernatant (cytosolic fraction) into new tube.

D. Immediately denature cytosolic fraction for 10 min at 95 °C in a Thermomixer compact (Eppendorf). In parallel, continue with step E.

E. Resuspend pellet in 0.3 ml solubilization buffer and incubate for 30 min at 4 °C in a tube rotator. Centrifuge 15 min at 16000 rcf at 4 °C. Transfer supernatant (membrane fraction) into new tube.

F. Immediately denature membrane fraction for 10 min at 95 °C in a Thermomixer compact (Eppendorf).

G. Store protein samples (cytosolic and membrane fraction) at -20 °C or immediately continue with protein quantification and SDS-PAGE.

2.6.1.2 Protein extraction from isolated tissues

- **Tissue lysis buffer:** 50 mM Tris pH 8.0, 100 mM NaCl, 5 mM EDTA, 2 % SDS and 2.5 mM PMSF in H_2O. *Attention*: *Composition differs from SDS lysis buffer for cells.*

A. Dissect tissue of interest from experimental animals (e.g., 2.5.2, A-C). Make sure that different conditions/animals are handled similarly. Weigh tissues with an analytical balance (QUINTIX35-1S; SARTORIUS). Shock-freeze 50-120 mg tissue samples (note exact weight) in liquid nitrogen and transfer them to -20 °C.

B. Add 7.5 µl SDS lysis buffer per mg tissue sample. Transfer tissue samples into FastPrep 2 ml Lysing Matrix Tubes supplemented with ~2 mm Garnet Lysing Matrix A and one 6.35 mm ceramic sphere (all from MP Biomedicals).

C. Disrupt tissue integrity with two FastPrep-24 (MP Biomedicals) cycles for 1 min each at 6.5 m/s. Put tubes on ice between cycles.

D. Centrifuge samples for 1 min at 18000 rcf at 4 °C and transfer protein-containing supernatant into new tube.

E. Denature protein 10 min at 95 °C in a Thermomixer compact (Eppendorf). Centrifuge for 5 min at 18000 rcf at 4 °C. Transfer supernatant into new tube (avoid transferring precipitate).

F. Store protein at -20 °C or immediately continue with protein quantification and SDS-PAGE.

2.6.2 Protein quantification with the Lowry assay

Protein quantification according to Lowry (Lowry et al., 1951) is a highly sensitive protein assay that is not disrupted by moderate SDS concentrations (Lees & Paxman, 1972). In this study, Peterson's modification of the Lowry method (Peterson, 1977) was performed. All samples were analyzed at least in duplicates.

- **Bovine serum albumin (BSA) standard:** 400 µg/ml BSA in H_2O. Prepare serial 1/2 dilution down to 12.5 µg/ml BSA. Store at -20 °C.

- Other **buffers** and chemicals: H_2O, Total Protein Kit - Micro Lowry - Peterson's Modification (Sigma-Aldrich, Cat-# TP0300-1KT; contains BSA standard, Lowry reagent (Cat-# L3540-25VL), and Folin-Ciocâlteu phenol reagent).

A. Fill up 10 µl (cell lysates) or 1 µl (tissue lysates) samples from 2.6.1 to 100 µl with H_2O in 1.5 ml tubes. Use the same amounts of lysis buffer (10 µl and 1 µl, respectively, ad 100 µl H_2O) as blank controls. For the standard curve, use 100 µl BSA standard and 100 µl H_2O as blank control.

B. Add 100 µl Lowry reagent to each sample, vortex thoroughly and incubate for 20 min at room temperature.

C. Add 50 µl Folin-Ciocâlteu phenol reagent to each sample, vortex thoroughly and incubate for 30 min at room temperature in the dark.

D. Prepare technical duplicates for each sample by pipetting 100 µl into 2 wells of a 96-well flat-bottom plate.

E. Determine OD_{620} with a multi-well plate reader (Multiskan EX, Thermo). Calculate protein concentration based on the BSA standard curve after subtraction of the appropriate blank controls.

2.6.3 SDS-PAGE and Western Blot analysis

Commonly, denatured proteins are analyzed by molecular weight-based separation via SDS-PAGE according to Laemmli (Laemmli, 1970) followed by immunostaining of specific proteins via Western Blot (Towbin et al., 1979). The combined specificity of the protein's migration behavior and the used antibody, in conjunction with the high sensitivity of enhanced chemiluminescence (ECL) detection, makes this method a powerful tool to determine even small differences in protein levels between different protein samples. The protocols used for SDS-PAGE and Western Blot in the present study are described below.

- **4x Tris/SDS pH 8.8:** 1.5 M Tris and 0.4 % SDS in H_2O. Adjust pH to 8.8 and store at 4 °C.
- **4x Tris/SDS pH 6.8:** 0.5 M Tris and 0.4 % SDS in H_2O. Adjust pH to 6.8 and store at 4 °C.
- **5x SDS loading dye:** 320 mM Tris pH 6.8, 40 % Glycerol, 15 % SDS, 25 % 2-mercaptoethanol and 1 mg/ml bromophenol blue. Concentrations correspond to the 5x stock solution used in the protocol below. Store at -20 °C.
- **SDS running buffer:** 25 mM Tris, 192 mM glycine and 0.1 % SDS in H_2O. Store at room temperature.
- **Anode buffer I:** 300 mM Tris and 20 % methanol in H_2O. Store at room temperature.
- **Anode buffer II:** 25 mM Tris and 20 % methanol in H_2O. Store at room temperature.
- **Cathode buffer:** 40 mM 6-aminohexanoic acid, 25 mM Tris and 20 % methanol in H_2O. Store at room temperature.
- **WB block solution:** 5 % milk powder in TBS-T. Store at 4 °C.

- **WB wash buffer:** 1 % milk powder in TBS-T. Store at 4 °C.
- **ECL substrate:** Solution A and solution B of WesternBright Sirius ECL substrate (Biozym) mixed in an equivalent manner. *Important: Always prepare freshly.*
- Other **buffers** and chemicals: H_2O, Rotiphorese Gel 30 (37.5:1) (Roth, Cat-# 3029.1), TEMED, APS (20 % in H_2O), isopropanol, protein ladder (PageRuler Prestained Protein Ladder; Thermo), Whatman blotting paper (A. Hartenstein, Cat-# GB46), PVDF membrane (Roche, Cat-# 03010040001), **TBS-T**, and antibodies (complete list of antibodies used for Western Blot is provided in **Table 6**).

A. Prepare 10 % SDS gels for a Mini-PROTEAN Tetra Cell system (Bio-Rad; 1.5 mm glass plates; 15 pockets/gel) as specified here:

	Rotipho-rese	Tris/SDS pH 6.8	Tris/SDS pH 8.8	H_2O	TEMED	APS
Stacking gel (4 %)	0.65 ml	1.25 ml	-	3.05 ml	10 µl	25 µl
Separating gel (10 %)	3.30 ml	-	2.5 ml	4.10 ml	10 µl	50 µl

The given quantities suffice for two 10 % SDS gels as specified above. Ensure complete polymerization before removing combs.

B. Thaw protein samples, dilute them to the desired concentration (usually 0.5-5 µg/µl final concentration; up to 20 µl can be loaded to the gels as prepared in the previous step) with H_2O and 5x SDS loading dye.

C. Denature the diluted protein samples at 95 °C for 5 min in a Thermomixer compact (Eppendorf).

D. Load samples into 10 % SDS gel (usually 10-50 µg total protein). As size reference, add 3 µl protein ladder.

E. Separate proteins in SDS running buffer by applying 80 V for 10 min and 120 V for additional 1 h (Standard Power Pack P25, Biometra).

F. Transfer protein from the SDS gel onto a PVDF membrane with a discontinuous Trans-Blot SD Semi-Dry Transfer Cell system (Bio-Rad). To do so, assemble the “blotting sandwich” consisting of (from anode to cathode):

   - 4 Whatman blotting papers soaked with anode buffer I
   - 4 Whatman blotting papers soaked with anode buffer II
   - PVDF membrane
   - SDS gel
   - 8 Whatman blotting papers soaked with cathode buffer

Make sure to remove all air bubbles by rolling a 10 ml pipette over the assembled blotting sandwich. Apply a current of 60 mA per blotting sandwich for 75 min (Standard Power Pack P25, Biometra).

G. Disassemble blotting sandwich and ensure complete protein transfer by looking at the prestained protein ladder.

H. Block PVDF membrane for 1 h at room temperature in WB block solution. During blocking, cut membrane where applicable. Wash 2x with TBS-T before immunostaining.

I. Incubate PVDF membrane in primary antibody (complete list of antibodies used for Western Blot can be found in **Table 6**) overnight at 4 °C. Wash 3x with WB wash buffer for 10 min each.

J. Incubate PVDF membrane in HRP-coupled secondary antibody for 2 h at room temperature. Wash 1x with WB wash buffer and 2x with TBS-T for 5 min each.

K. Add ECL substrate to PVDF membrane (2 ml ECL substrate suffice for one membrane) and detect chemiluminescence with a ChemiDoc Imaging System (Bio-Rad).

L. To be able to assign protein sizes to each band using the protein ladder, take a picture with the “Colorimetric” setting. If membrane shall be re-probed, wash with TBS-T for 30 min.

Table 6: Antibodies used for Western Blot in the present study.

Antibody	Source/ isotype	Poly-/mono-clonal	Manufacturer & order-#	Working dilution*
α-cGKIc(DH)	rabbit	poly	workgroup Feil [1]	1/5000
α-NO-GC β1 2A	rabbit	poly	workgroup Friebe [2]	1/10000
α-GAPDH	rabbit	mono	Cell Signaling #2118	1/1000
α-GC-B(ECD)	guinea pig	poly	workgroup Schmidt [3]	1/5000
α-RFP	rabbit	poly	abs-online #ABIN129578	1/2500
α-SM22	rabbit	poly	abcam #ab14106	1/1000
α-phospho(Ser239)-VASP	rabbit	poly	Cell Signaling #3114	1/1000
α-rabbit IgG, HRP-linked	goat	poly	Cell Signaling #7074	1/5000
α-guinea pig IgG, HRP-linked	donkey	poly	Jackson #706-035-148	1/10000

Footnotes: *Primary antibodies were diluted in TBS-T +5 % BSA +0.05 % NaN_3. Secondary antibodies were diluted in WB wash buffer. [1]Valtcheva et al. (2009); [2]Friebe et al. (2007); [3]Ter-Avetisyan et al. (2014).

2.7 Staining of murine tissue sections

In contrast to the analysis of tissue lysates, (immuno-)staining of tissue sections enables inspection of protein expression *in situ* at the single-cell level. This, however, comes at the cost of a relatively poor signal-to-noise ratio and quantifiability, which is mostly due to the background from the tissue itself (i.e., autofluorescence) and unspecific binding of antibodies. In particular, this work included transgenic cells and mice that stably

expressed certain fluorescent proteins (i.e., mCherry, tdTomato, and cGi500). These proteins might still be fluorescent in tissue sections after fixation, resulting in substantial fluorescence that is not related to the staining with fluorescent antibodies. To benefit from the strengths of both methodologies, analysis of tissue lysates (see also 2.6) and *in situ* (immuno-)staining of tissue sections as described in the following sections were used in a complementary manner.

2.7.1 Fixation and preparation of frozen tissue sections

- **Tissuefix:** 4 % PFA in PBS. Aid dissolution by heating to 50 °C and adding 100 µl of a 1 M NaOH solution. Adjust pH to 7.4, sterile filter and store at -20 °C.
- **Zambroni's fixative:** 2 % PFA and 0.15 % (v/v) picric acid in PBS. Aid PFA dissolution by heating to 50 °C and adding 100 µl of a 1 M NaOH solution. Adjust pH to 7.4, sterile filter and store at -20 °C
- **Sucrose solution:** 30 % sucrose in PBS. Store at 4 °C.
- Other **buffers** and chemicals: **PBS**, Tissue-Tek (Tissue-Tek O.C.T. Compound; Sakura)

A. Extract tissue of interest from experimental animals (2.5.2, A-C). Make sure that different conditions/animals are handled similarly.

B. Fix tissues for 3-4 h with tissuefix at 4 °C. *Attention: If sections are to be used for X-Gal (5-bromo-4-chloro-3-indolyl-β-D-galactopyranoside) staining, exchange tissuefix for Zambroni's fixative and perform fixation for 20 min at room temperature according to Kramer et al. (2021).*

C. Wash tissues 2x with PBS and incubate for 18 h in sucrose solution at 4 °C. Freeze tissues in Tissue-Tek at -20 °C.

D. After complete solidification of Tissue-Tek, prepare 20 µm-thick frozen tissue sections (cutting plane for tumor sectioning is depicted in **Figure S3**) with a cryostat (HM 505 E; MICROM) on SuperFrost Plus object slides (Thermo).

E. Allow tissue sections to adhere to their object slides for ~30 min at room temperature. From here on, store sections at -20 °C until further procedures are applied.

2.7.2 Immunofluorescence (IF) staining of frozen tissue sections

Given the large number of different fluorophores that can be linked to secondary antibodies, IF is a good choice to perform co-staining of several proteins. Within this work, the nuclear stain Hoechst 33258 was combined with green (Alexa Fluor 488) and red

(Alexa Fluor 555 and Alexa Fluor 594) fluorescence to analyze colocalization of cell type-specific marker proteins with components of the cGMP signaling pathway. The spectra of these fluorescent dyes enabled efficient separation of the different channels. However, there was a huge spectral overlap between the fluorescent dyes and the fluorescent reporters used herein. Therefore, any combination of various green (Alexa Fluor 488, cGi500) or red (Alexa Fluor 555/594, mCherry, tdTomato) fluorophores was avoided wherever possible. Of note, this could not be done in the IF shown in **Figures S6 and S7,** since these samples expressed both cGi500 and mT, thereby blocking both fluorescent channels.

- **IF block solution:** 1 % normal goat serum (Sigma-Aldrich, Cat-# S26-100mL) in PBS-T. Store at 4 °C.
- Other **buffers** and chemicals: **PBS**, **PBS-T**, Tissue-Tek (Sakura), antibodies (complete list of antibodies used for IF staining is provided in **Table 7**), Hoechst 33258 (Sigma-Aldrich, CAS 23491-45-4), H_2O, and Immu-Mount (Fisher).

A. Allow frozen sections to adapt to room temperature for ~30 min and remove Tissue-Tek by immersing the glass slide in PBS for 10 min.

B. Block unspecific binding sites with IF block solution for 1 h at room temperature. Remove blocking solution completely.

C. Add primary antibody overnight at 4 °C in a humidified chamber to prevent drying-out. Remove primary antibody and wash 3x10 min with PBS-T at room temperature

D. Incubate tissue sections in secondary antibody for ≥ 2 h at room temperature. From here, keep samples in the dark. During the last secondary antibody incubation, add Hoechst 33258 (1 µg/ml final concentration) for nuclear staining.

E. Remove secondary antibody and wash 3x10 min with PBS-T at room temperature. If more than one immunostaining is to be performed, repeat procedures C-E.

F. After completing the last immunostaining, immerse object slides with tissue sections in H_2O and completely remove liquid. *Attention*: *Do not allow tissue to completely dry out.*

G. Add 3 drops of Immu-Mount per object slide. Add a coverslip of suitable size and remove air bubbles by carefully pushing them to the border of the coverslip. Make sure to not damage the tissue through pressure.

H. Let Immu-Mount solidify for 18 h and acquire images with a confocal laser scanning microscope (LSM) 710 setup as specified below.

The LSM 710 setup consisted of an inverted Axio Observer.Z1 stand (ZEISS) equipped with a diode laser (405 nm), a multiline Argon laser (25 mW; 458 nm, 488 nm and 514 nm), a diode-pumped solid-state laser (561 nm), a He/Ne laser (633 nm), and an air objective (Plan-APOCHROMAT 20x/0.8; ZEISS). Hoechst 33258 was excited with the 405 nm laser, Alexa Fluor 488 with the Argon laser 488 nm line, and Alexa Fluor 555/594 with the 561 nm laser. Confocal epifluorescence images were acquired with an LSM 710 3-channel spectral detector using the ZEN Black software (ZEISS).

Table 7: Antibodies used for IF staining in the present study.

Antibody	Source/ isotype	Poly-/mono-clonal	Manufacturer & order-#	Working dilution*
α-PDGFR-β	goat	poly	R&D #AF1042	1/100
α-CD31	rat IgG2a κ	mono	BD Pharmingen #550274	1/50
α-NO-GC β1 1A	rabbit	poly	workgroup Friebe [1]	1/1000
α-cGKIc(DH)	rabbit	poly	workgroup Feil [2]	1/1000
α-GFP	chicken	poly	abcam #13970	1/2000
α-goat IgG, Alexa Fluor 594-linked	donkey	poly	invitrogen #A11058	1/1000
α-rat IgG, Alexa Fluor 594-linked	rabbit	poly	invitrogen #A21211	1/1000
α-rabbit IgG, Alexa Fluor 488/555-linked	goat	poly	invitrogen #A11034 (488) and #A21429 (555)	1/1000
α-chicken IgY, Alexa Fluor 488-linked	goat	poly	invitrogen #A11039	1/1000

Footnotes: *Antibodies were diluted in IF block solution. [1]Friebe et al. (2007); [2]Valtcheva et al. (2009).

2.7.3 X-Gal staining of frozen tissue sections

X-Gal staining is based on the β-galactosidase-catalyzed conversion of the lactose analog X-Gal to an indigo dye. Introduction of the *E. coli lacZ* gene (coding for β-galactosidase) under a cell type-specific promoter into the murine genome allows for the highly specific and sensitive identification of cells in which the respective promoter is active (Kramer et al., 2021). In the present study, tumors of CNP-lacZ and GC-B-lacZ mice expressing β-galactosidase with a nuclear localization sequence were evaluated via X-Gal staining as detailed below (*Attention: different fixation required*). The resulting nuclear X-Gal staining was combined with chromogenic immunohistochemistry (CIH) to assign CNP- and GC-B-positive cells to structures.

- **X-Gal wash buffer:** 2 mM $MgCl_2$, 0.01 % sodium deoxycholate and 0.02 % Nonidet P-40 in PBS. Store at room temperature. Protect from light.
- **X-Gal stock solution:** 20 mg/ml X-Gal (invitrogen, Cat-# 15520-018) in DMF. Store at -20 °C. Protect from light.
- **X-Gal staining buffer:** 5 mM $K_3Fe(CN)_6$, 5 mM $K_4Fe(CN)_6$ and 0.5 mg/ml X-Gal (from X-Gal stock solution) in X-Gal wash buffer.
- **Tissuefix:** 4 % PFA in PBS. Aid dissolution by heating to 50 °C and adding 100 µl of a 1 M NaOH solution. Adjust pH to 7.4, sterile filter and store at -20 °C.
- Other **buffers** and chemicals: **PBS** and $MgCl_2$.

A. Allow frozen sections to adapt to room temperature for 30 min and remove Tissue-Tek by immersing the glass slides in PBS for 10 min. Wash cryosections 3x10 min in X-Gal wash buffer.

B. Incubate cryosections upside-down in X-Gal staining buffer for 2 h to overnight at 37 °C in a humid chamber in the dark. Wash 3x10 min in PBS supplemented with 2 mM $MgCl_2$.

C. Fix the cryosections for 10 min in tissuefix at room temperature. Wash 3x10 min with PBS. Continue with CIH or IF, or remove liquid and freeze cryosections at -20 °C.

2.7.4 Chromogenic immunohistochemistry (CIH) of frozen tissue sections

In contrast to the fluorescence-based IF, CIH makes use of a color-producing reaction. Commonly, the signal-amplifying properties of the avidin-biotin complex (ABC) is used to boost the peroxidase-catalyzed oxidation of 3,3'-diaminobenzidine (DAB) to a precipitating brown polymer (Hsu et al., 1981). These two layers of signal amplification, ABC and enzymatic reaction, make CIH much more sensitive than IF. However, due to the limited number of peroxidase substrates (and different colors), complicated separation of colors within the same region, and large spatial expansion of the staining due to the huge size of the formed complex, CIH is not well suited for colocalization experiments. Instead, CIH herein was used in conjunction with X-Gal staining to identify structures expressing CNP and GC-B.

- **Peroxidase block:** 9 % H_2O_2 and 1.3 % methanol in PBS.
- **Antigen retrieval solution:** 10 mM sodium citrate in H_2O. Adjust pH to 6.0 with citric acid. Store at room temperature.
- **CIH block solution:** 10 % normal goat serum (Sigma-Aldrich, Cat-# S26-100mL) in TBS-T. Store at 4 °C.
- **ABC solution:** 1 % reagent A and 1 % reagent B (VECTASTAIN Elite ABC-HRP Kit, Peroxidase (Standard); Vector Labs, Cat-# PK-6100) in 48 % PBS. Add 50 % TBS-T directly before use.
- **DAB staining solution:** 0.05 % DAB (Sigma-Aldrich, Cat-# D5637) and 0.01875 % H_2O_2 in PBS.
- Other **buffers** and chemicals: **PBS**, **TBS-T**, antibodies (complete list of antibodies used for CIH staining is provided in **Table 8**), Hoechst 33258 (Sigma-Aldrich, CAS 23491-45-4), H_2O, and Aquatex Aqueous Mounting Medium (Merck).

A. Allow frozen sections to adapt to room temperature for 30 min and remove Tissue-Tek by immersing the glass slides in PBS for 10 min.

B. Block endogenous peroxidases with peroxidase block for 20 min at room temperature in a humid chamber. Wash 3 min with PBS at room temperature.

C. Incubate in antigen retrieval solution for 15 min at room temperature followed by 10 min at 92 °C in a water bath. Let samples cool down for 10 min at room temperature. Wash briefly with TBS-T.

D. Block unspecific binding sites with CIH block solution for 2 h at room temperature. Remove block solution completely.

E. Add primary antibody overnight at 4 °C in a humidified chamber to prevent drying-out. Remove primary antibody, wash 3x5 min with TBS-T at room temperature.

F. Add biotinylated secondary antibody supplemented with Hoechst 33258 (1 µg/ml final; for nuclear staining) for 2 h at room temperature. From here, keep samples in the dark. Remove liquid and wash 3x5 min with TBS-T at room temperature.

G. Incubate sections in freshly prepared ABC solution for 30 min at room temperature in a humid chamber. Remove ABC solution completely and wash 3x5 min with TBS-T at room temperature.

H. Incubate samples with freshly prepared DAB staining solution, until a sufficient staining intensity is achieved (prolonged staining might increase background).

I. Stop staining by immersing object slides with tissue sections in H_2O. Remove liquid completely. *Attention*: *Do not allow tissue to completely dry out.*

J. Add 3 drops of Aquatex medium per object slide. Add a coverslip of suitable size and remove air bubbles by carefully pushing them to the border of the coverslip. Make sure to not damage the tissue through pressure.

K. Let Aquatex medium solidify for 18 h and acquire images with an Axioskop 20 microscope setup as specified below.

The microscope setup for acquisition of X-Gal and CIH images consisted of an Axioskop 20 microscope (ZEISS) equipped with an HBO 50 mercury short-arc lamp for epifluorescence illumination, a halogen lamp for brightfield illumination, a brightfield condenser 0.9 Z with swing-in front lens, and three air objectives (A-Plan 5x/0.12, A-Plan 10x/0.25, Plan-NEOFLUAR 20x/0.5; all from ZEISS). Hoechst 33258 fluorescence was detected through a filter set consisting of a 365 nm shortpass excitation filter, a 395 nm dichroic mirror and a 420 nm longpass emission filter. Images were acquired with an EOS 750D complementary metal-oxide-semiconductor (CMOS) camera (Canon) mounted with a 1.6x camera adapter.

Table 8: Antibodies used for CIH staining in the present study.

Antibody	Source/ isotype	Poly-/mono-clonal	Manufacturer & order-#	Working dilution*
α-CD31	rat IgG2a κ	mono	BD Pharmingen #550274	1/25
α-SMA	rabbit IgG	mono	abcam #ab124964	1/2000
α-rat IgG, biotinylated	rabbit	poly	Vector Labs #BA-4001	1/250
α-rabbit IgG, biotinylated	goat	poly	Vector Labs #BA-1000	1/250

Footnotes: *Antibodies were diluted in TBS-T +5 % normal goat serum.

2.8 Statistics

Statistical analysis was performed using Origin 2019 (OriginLab), with $P < 0.05$ considered to be significant. For not normally distributed data sets, statistical differences were analyzed non-parametrically by Mann-Whitney *U*-Test. In case of normally distributed data, statistical differences were analyzed parametrically by Student's *t*-Test (equal variances) or Welch's *t*-Test (unequal variances). Statistical differences of multifactorial comparisons were assessed by one-way ANOVA and post-hoc Bonferroni *t*-Test. The DEA/NO concentration-response curve on kidney slices in **Figure 1** was calculated with the sigmoidal "DoseResp" fitting function of Origin 2019. Asterisks (*) represent different significance levels: *$P > 0.05$; **$P \leq 0.01$; ***$P \leq 0.001$.

3 Results

3.1 Inside the renal cortex, cGMP is mainly generated by glomeruli and blood vessels in response to NO and ANP

cGMP is known to be an important regulator of renal function: ANP and NO were associated with important physiological parameters in the kidney, including natri- and diuresis, GFR, and renal blood flow (see also 1.2.2). Indeed, recent studies have pointed towards the cGMP pathway as potential drug target in CKD (Boustany-Kari et al., 2016; J. V. Tobin et al., 2018) (reviewed by Krishnan et al., 2018). However, the molecular and structural mechanisms linking ANP and NO with the observed physiological changes are not well-characterized. To my knowledge, this study analyzed for the first time cGMP generation *in situ* in the adult kidney by utilizing a real-time cGMP imaging approach. To do so, vital kidney slices from cGi-L1 mice, which express the cGMP sensor cGi500 globally in all cells, were subjected to multicolor imaging of the cGMP sensor to monitor cGMP concentration changes in response to the physiological GC ligands NO and ANP (outlined schematically in **Figure 1A**, left panel).

First, cGi500 expression was assessed in whole kidney slices (**Figure 1A**, right panel). YFP fluorescence of the cGMP sensor protein (as an indicator for the quantity of cGi500 protein and completely independent of the presence and concentration of cGMP) was detected in all anatomical compartments of the kidneys, i.e., cortex, medulla, and pelvis. The YFP fluorescence intensity varied between different renal structures, being particularly high in glomeruli.

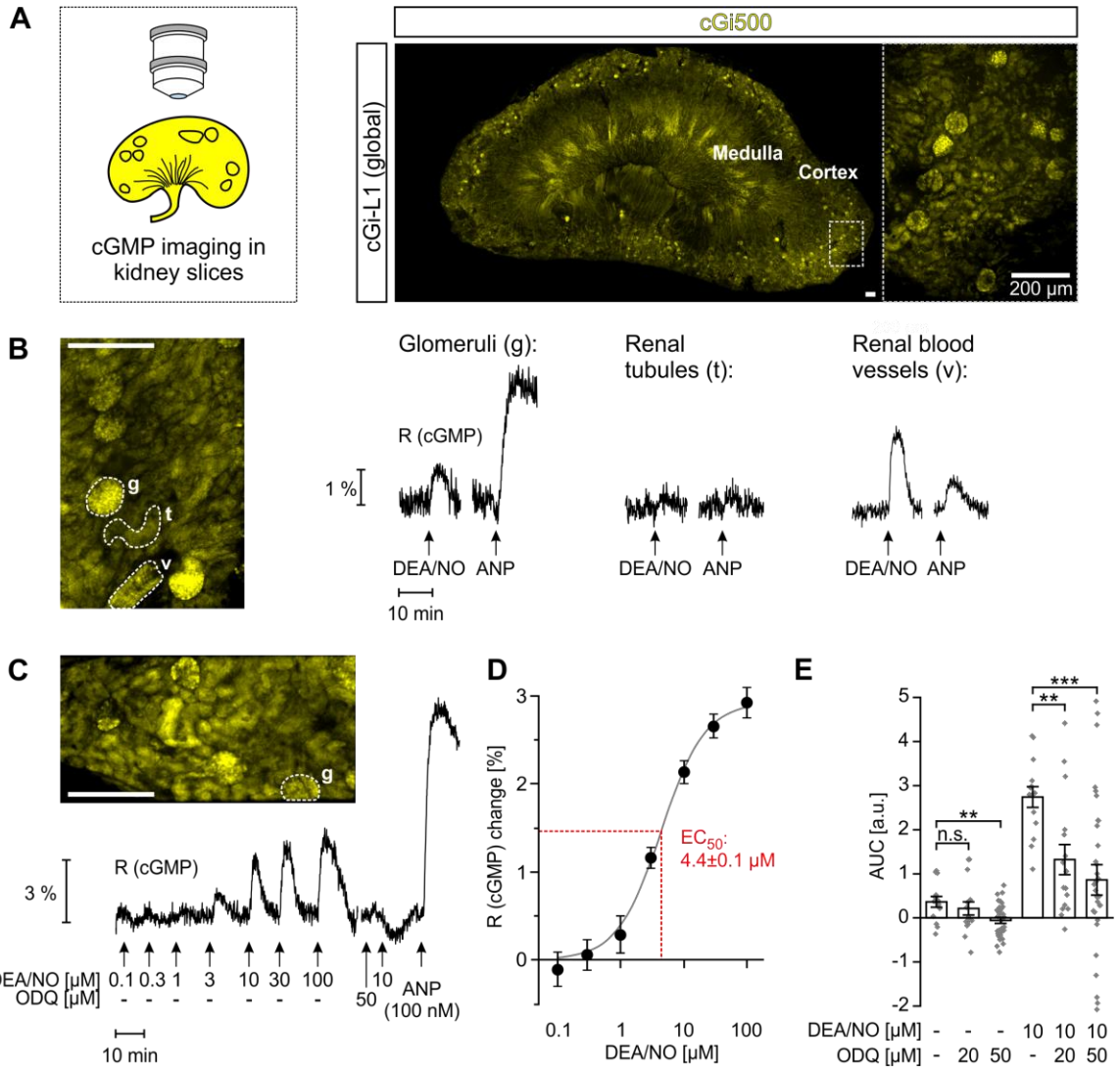

Figure 1: NO concentration-dependently induces cGMP generation in the glomeruli of acute kidney slices, which is inhibited by the NO-GC-oxidizing agent ODQ. FRET-based cGMP imaging was performed with acute kidney slices from cGi-L1 mice. **(A)** Schematic representation (left) and representative image (right) of acute kidney slices. Yellow color represents YFP fluorescence of cGi500 in renal cells, not cGMP. Dashed rectangle indicates the magnified region shown right. **(B)** Representative real-time FRET/cGMP measurement of an acute kidney slice. During the measurement, slices were superfused with DEA/NO (10 µM) or ANP (100 nM) for 2 min each. Black traces represent the CFP/YFP ratio R, which indicates cGMP concentration changes, recorded in glomeruli (g), renal tubules (t), and blood vessels (v). **(C)** In a different set of FRET/cGMP imaging experiments, increasing concentrations of DEA/NO or ANP (100 nM) were applied to the slices for 2 min each. Before the second last stimulation with 10 µM DEA/NO, slices were pre-incubated for 5 min with ODQ (50 µM). **(D)** The concentration-response relationship of DEA/NO on glomerular cGMP was evaluated using the relative R (cGMP) changes (n = 19 glomeruli in 4 kidney slices from 2 mice). **(E)** Statistical analysis was performed with the AUC of cGMP changes induced by ODQ, DEA/NO alone, and DEA/NO in the presence of ODQ (n ≥ 14 glomeruli in ≥ 5 kidney slices from ≥ 2 mice). Data represent mean ± SEM. g, glomerulus; t, renal tubule; v, renal blood vessel; AUC, area under the curve. Scale bars, 200 µm. Part of these results was published in Stehle et al. (2021).

Subsequently, cGMP was visualized in these kidney slices by looking at CFP/YFP-FRET changes in response to various drugs. In the renal cortex, glomeruli, renal tubules and perilobular blood vessels could be readily identified by their anatomical features (**Figure 1B**; histological image for comparison can be found in **Figure I5**). Glomeruli showed cGMP increases in response to NO (applied in the form of 10 µM of the NO-releasing compound DEA/NO) and sustained cGMP increases in response to ANP (100 nM). In renal tubules, only minor R (cGMP) changes could be detected in response to both DEA/NO and ANP. Large renal blood vessels, which could be distinguished from tubules by their characteristic VSMC "rings", responded well to DEA/NO and ANP. Their response patterns were different from the glomeruli's, as the blood vessels showed higher R (cGMP) changes in response to DEA/NO and lower R (cGMP) changes in response to ANP in the given concentrations when compared to glomeruli (**Figure 1B**, right panel). These perilobular blood vessels, however, were rarely captured in the field of view, indicating that only few of them are present in the renal cortex. This made quantitative analysis of the perilobular blood vessels' cGMP signaling infeasible, which is why subsequent experiments herein focused on the glomeruli. The GC-B-stimulating CNP (0.1-1 µM) was also applied to the renal cortex in some measurements, but CNP-induced R (cGMP) changes were not observed (data not shown). Together, these experiments demonstrated glomeruli and their associated renal vasculature to be the main producers of cGMP within the adult murine kidney.

Next, the capacity of glomeruli for NO-induced cGMP generation and their sensitivity to NO were assessed in more detail. Increasing DEA/NO concentrations ranging from 0.1 to 100 µM were applied to the kidney slices. Concentration-dependent cGMP transients were observed in glomeruli with an EC_{50} of 4.4 ± 0.1 µM DEA/NO (**Figure 1C and D**). After the highest DEA/NO concentration (100 µM), the NO-GC oxidant ODQ (50 µM) was applied to the kidney slices. ODQ on its own slightly decreased the basal R (cGMP). More importantly, however, subsequent addition of DEA/NO (10 µM) did no longer increase the glomerular cGMP levels. ANP (100 nM), on the other hand, still potently increased the glomerular cGMP levels after ODQ application (without ODQ: 2.2 ± 0.3 % versus 50 µM ODQ: 4.0 ± 0.9 % R (cGMP) change; **Figure S4A**). These results indicated that (1) ODQ application resulted in the loss of NO-induced cGMP generation, probably by formation

of the NO-unresponsive, heme-oxidized NO-GC,(2) NO-GC-independent cGMP generation triggered by ANP was not affected by ODQ and (3) the tissue was still vital at the end of each individual experiment. Both effects of ODQ on glomerular cGMP signaling, slight reduction of basal R (cGMP) (AUC of control: 0.4 ± 0.1 a.u. versus 20 µM ODQ: 0.2 ± 0.1 a.u. versus 50 µM ODQ: -0.1 ± 0.1 a.u.) and attenuation of DEA/NO-induced cGMP generation (control: 2.7 ± 0.2 a.u. versus 20 µM ODQ: 1.3 ± 0.3 a.u. versus 50 µM ODQ: 0.9 ± 0.3 a.u.), were observed to be concentration-dependent (**Figure 1E**). Of note, 50 µM ODQ were not sufficient to completely abolish cGMP generation in response to DEA/NO (10 µM) in the entirety of the assessed renal glomeruli. Together, these data demonstrated the presence of a functional and oxidation-sensitive NO/cGMP signaling pathway in the glomeruli of murine kidneys.

3.2 NO-GC stimulator potentiates NO-induced cGMP in glomeruli, while NO-GC activator increases cGMP under oxidative stress-conditions

With the newly established cGMP imaging setup in kidney slices, cGMP-modulating drugs could be readily tested under close-to-native conditions. Especially NO-GC-stimulating drugs are a current research focus, with many novel compounds being developed for the treatment of several diseases including CKD. The present study aimed to test two of these NO-GC-modulating drugs, the NO-GC stimulator BAY-41 (BAY 41-2272) and the novel NO-GC activator BAY-543, on the murine kidney. Kidney slices from cGi-L1 mice were analyzed either under native conditions or in the presence of the NO-GC-oxidizing agent ODQ to mimic oxidative stress, which was associated with CKD. The physiological ligand NO, NO-GC modulator or a combination of both substances were superfused, and glomerular cGMP levels were followed.

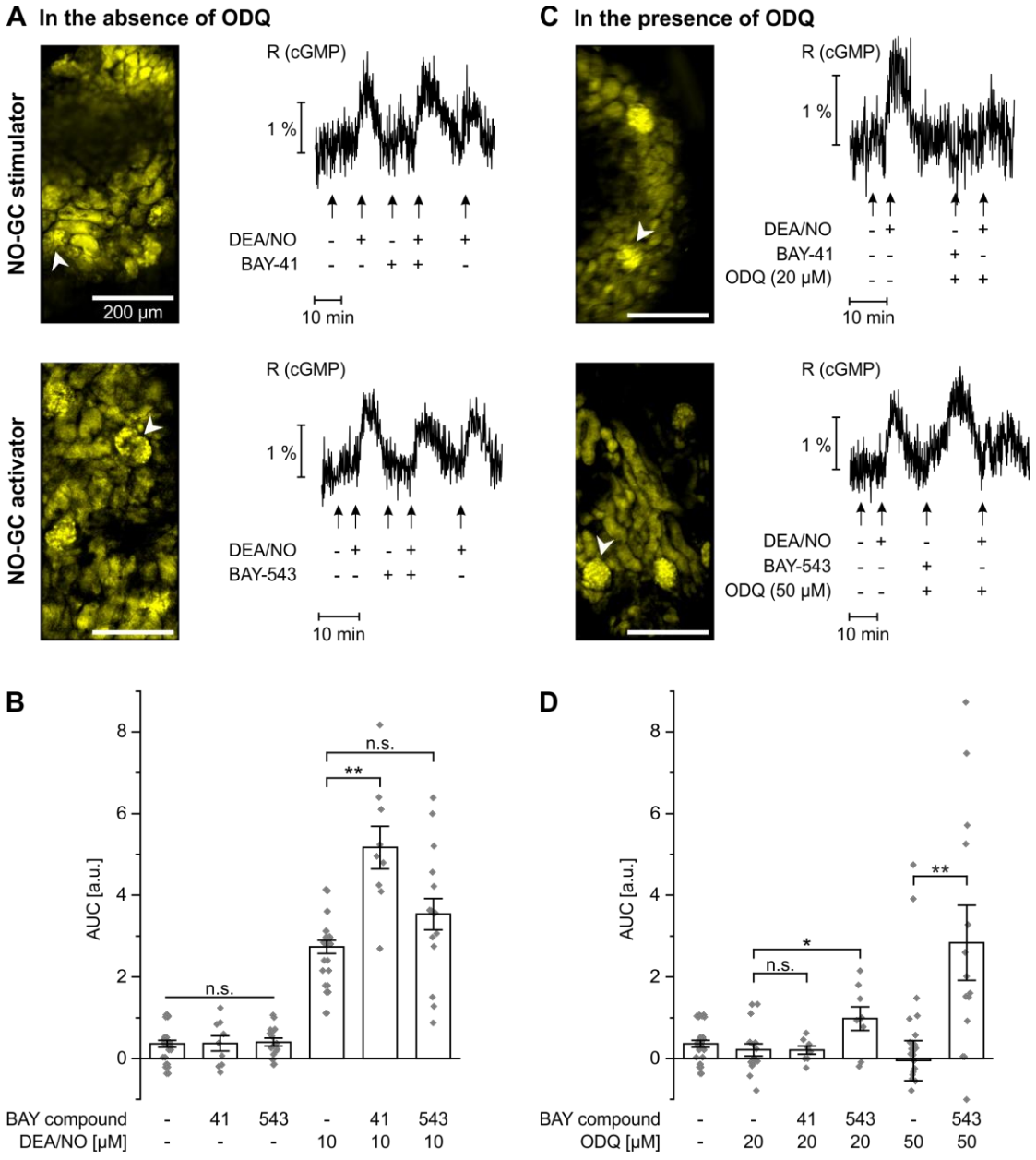

Figure 2: The NO-GC stimulator BAY-41 acts synergistically with NO, whereas the NO-GC activator BAY-543 acts NO-independently in the presence of ODQ. FRET-based cGMP imaging was performed in the glomeruli of acute kidney slices from cGi-L1 mice. **(A)** Representative cGMP measurements of renal glomeruli under native conditions. During the measurements, vehicle control (0.1 % DMSO), DEA/NO (10 µM), BAY-41 (10 µM), BAY-543 (10 µM) or a combination of DEA/NO and BAY compound were applied to the slices for 2 min each. Black traces represent the CFP/YFP ratio R, which indicates cGMP concentration changes. White arrow heads point towards the glomeruli represented by the traces on the right side. **(B)** Statistical analysis was performed with the AUC of the signals. **(C)** Representative cGMP measurements of renal glomeruli in the presence of ODQ. Vehicle, DEA/NO and BAY compounds were applied to the slices for 2 min each, either with or without 5 min pre-incubation with ODQ (50 µM). **(D)** Statistical analysis was performed with the AUC of the signals. Note that negative AUC values in the presence of ODQ can be explained by (1) increased noise and (2) reduced endogenous cGMP generation. Data represent mean ± SEM (n ≥ 8 glomeruli in ≥ 3 kidney slices from ≥ 2 mice). AUC, area under the curve. Scale bars, 200 µm. Part of these results was published in Stehle et al. (2021).

First, kidney slices were analyzed under native conditions (**Figure 2A and B**). In line with the previous experiments (**Figure 1C**), DEA/NO (10 µM) induced robust, but non-saturated cGMP generation in renal glomeruli. The NO-GC stimulator BAY-41 (10 µM) alone did not significantly increase glomerular cGMP when compared with vehicle control (0.1 % DMSO; indicated as "-/-" in panel A) (**Figure 2A**, top graph; **Figure 2B**). Co-application of BAY-41 and DEA/NO, however, induced significantly stronger cGMP signals than DEA/NO alone (AUC of control: 2.7 ± 0.2 a.u. versus BAY-41: 5.2 ± 0.5 a.u.). The NO-GC activator BAY-543 (10 µM) under the same conditions did not increase glomerular cGMP levels on its own and failed to significantly potentiate the DEA/NO-induced cGMP generation (**Figure 2A**, bottom graph; **Figure 2B**).

Glomerular cGMP levels were also assessed in the presence of the NO-GC inhibitor ODQ (**Figure 2C and D**). Prior to these experiments, vehicle (0.1 % DMSO; indicated as "-/-/-" in panel C) and DEA/NO (10 µM; indicated as "+/-/-" in panel C) were applied as controls to validate the functionality of the setup. Indeed, DEA/NO but not DMSO induced an increase in glomerular cGMP. Subsequently, kidney slices were incubated with ODQ (20 or 50 µM as indicated) for 5 min followed by application of BAY compound. Under these conditions (i.e., in the presence of ODQ and in the absence of exogenous DEA/NO), BAY-41 (10 µM) did not increase glomerular cGMP levels (**Figure 2C**, top graph; **Figure 2D**). The NO-GC activator BAY-543 (10 µM), on the other hand, potently induced cGMP generation (**Figure 2C**, bottom graph; **Figure 2D**). As expected, BAY-543-induced cGMP generation was more pronounced in the presence of 50 µM ODQ when compared with 20 µM ODQ (**Figure 2D**) (50 µM ODQ: 2.8 ± 0.9 a.u. versus 20 µM ODQ: 1.0 ± 0.3 a.u.). Altogether, these data demonstrated that the NO-GC stimulator BAY-41 has the capacity to potentiate endogenous NO-induced cGMP signaling in glomeruli with normal oxidative stress levels. The NO-GC activator BAY-543, on the other hand, induces cGMP production in murine glomeruli under disease-relevant oxidative stress-conditions mimicked by ODQ application, where the effects of NO and NO-GC stimulators are diminished.

3.3 Melanoma cells express a functional CNP/GC-B/cGMP/cGKI cascade

After the potency of NO-GC modulators had been assessed on kidney slices, an additional set of experiments aimed to uncover the role of NO-GC/cGMP signaling in melanoma. The (patho)physiological effects of cGMP in melanoma development and progression are still a matter of debate. Whereas some studies observed deleterious effects of high cGMP on tumorigenesis (Arozarena et al., 2011; Dhayade et al., 2016; W. Q. Li, Qureshi, et al., 2014), others suggested an anti-tumor effect of cGMP stimulation in melanoma (Kashiwagi et al., 2005; Meyer et al., 2011) (discussed in 1.3.5). One plausible explanation for these discrepancies is that different cell types and their related cGMP signaling cascades mediated the respective effects. More precisely, the studies of Arozarena et al. and Dhayade et al. focused on the melanoma cells and showed increased growth and invasiveness of these cells in response to stimulation of the cGMP pathway. Kashiwagi et al. and Meyer et al., on the other hand, analyzed cells of the tumor stroma (mural cells and myeloid-derived suppressor cells, respectively) upon modulation of cGMP pathway components in melanoma.

The seemingly contradictory results of the previous studies show that further work is required to improve our knowledge of the underlying mechanisms of cGMP signaling and to ultimately utilize this pathway as drug target in melanoma. Thus, in the present study, cGMP signaling was characterized in melanoma cells as well as various other cell types within the tumor microenvironment. First, several cultured melanoma cell lines (**Figure 3A**) were transfected with pCMV-cGi500 and microscopically analyzed. YFP fluorescence was used to identify cGMP sensor-expressing cells, and changes of the intracellular cGMP levels in response to the physiological GC ligands NO, ANP and CNP were monitored via FRET/cGMP imaging. In parallel, protein was extracted from non-transfected melanoma cells to analyze the expression of cGMP pathway proteins.

A

Cell line	Species	Tumor	BRAF	NRAS
B16F10	murine	metastatic [1]	WT	WT
1205Lu	human	metastatic	V600E	WT
A375	human	metastatic	V600E	WT
SKMel147	human	metastatic	WT	Q61L
SKMel19	human	metastatic	V600E	WT
WM3211	human	primary	WT	WT
WM35	human	primary	V600E	WT
WM852	human	metastatic	V600E	WT
G361	human	metastatic	V600E	WT

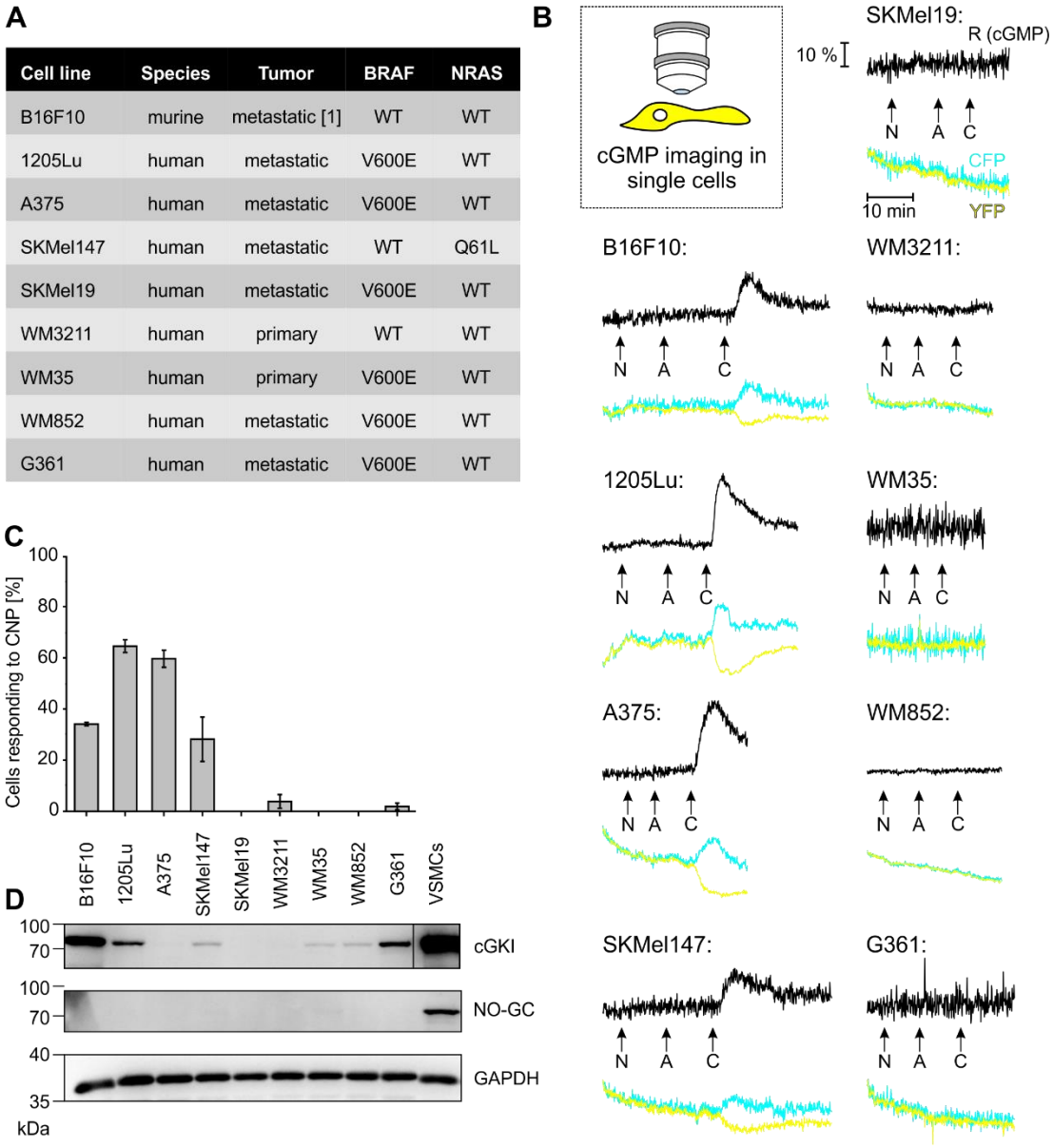

Figure 3: Melanoma cells generate cGMP in response to CNP, but not to NO or ANP. Murine B16F10 cells as well as different human melanoma cell lines were characterized according to their cGMP signaling. **(A)** Features of the different melanoma cell lines, including their *BRAF* and *NRAS* genotype. **(B)** Melanoma cells were transfected with pCMV-cGi500. Single cells were subjected to real-time FRET/cGMP imaging in the absence and presence of DEA/NO (N; 500 nM), ANP (A; 250 nM), and CNP (C; 250 nM). GC ligands were superfused for 2 min each. Representative R (cGMP), CFP and YFP traces are shown. **(C)** Quantification of cells showing CNP-induced cGMP signals. Data represent mean ± SEM (n ≥ 3 independent experiments). **(D)** Protein extracted from these different melanoma cell lines was analyzed via SDS-PAGE followed by Western Blot. Immunostaining for cGKI, NO-GC and GAPDH (as reference protein) was performed (n = 2 Western Blots). [1]B16F10 cells originally were isolated from a primary tumor, but were *in vivo*-passaged via metastases as described in 1.3.6, last paragraph.

The analyzed tumor cell lines covered a broad genotypic and phenotypic spectrum. Cells were extracted from melanoma-bearing mice (B16F10) or humans (all other cell lines), were of primary or metastatic origin, and differed with regard to the genotype of the two most commonly mutated genes in human melanoma, *BRAF* and *NRAS* (**Figure 3A**). To ensure the reliability of the cGMP imaging setup in all cells including those not responding to the tested GC ligands, cells were permeabilized with β-escin (0.1 mM) at the end of each individual experiment. Subsequent application of 100 µM cGMP reliably induced R (cGMP) changes (data not shown). In none of the tested melanoma cell lines, cGMP generation could be detected in response to DEA/NO (500 nM) or ANP (250 nM) (**Figure 3B**). CNP (250 nM), however, increased cGMP levels in the murine melanoma cell line B16F10 as well as the human melanoma cell lines 1205Lu, A375 and SKMel147, whilst cGMP signals were not detected in the other tested cell lines (**Figure 3B and C**). Interestingly, all CNP-responsive cell lines have been isolated from metastatic tumors. Consistent with the cGMP imaging data, NO-GC was not detectable in protein lysates of any tested melanoma cell line (**Figure 3D**). Lysates of primary aortic VSMCs, which were used as a positive control, clearly contained NO-GC protein. The major downstream cGMP effector protein cGKI was detected in several of the analyzed melanoma cell lines including CNP-responsive B16F10, 1205Lu and SKMel147 cells as well as in VSMCs, which served as positive control (**Figure 3D**). These data suggested that NO/NO-GC and ANP/GC-A signaling are not present in the tested murine and human melanoma cells, while CNP/GC-B is able to increase cGMP in some, but not all, melanoma cell lines.

Many melanomas including B16F10 are highly pigmented due to their melanin production. The obstructive optical properties of melanin cause that large fractions of excitation and emission light are absorbed by the tissue, leading to an impaired signal-to-noise ratio as well as cell damage and tissue inflammation during *in situ* imaging (Tikoo et al., 2021). One common approach to circumvent these problems is to render the melanoma cells amelanotic. This can be done by (1) *in vitro*-passaging until melanin generation is lost or (2) targeted mutagenesis of proteins involved in melanin biosynthesis. Amelanotic B16F10 (B16F10-A) cells used in this study were generated by CRISPR/Cas9-mediated deletion of tyrosinase (Tikoo et al., 2021).

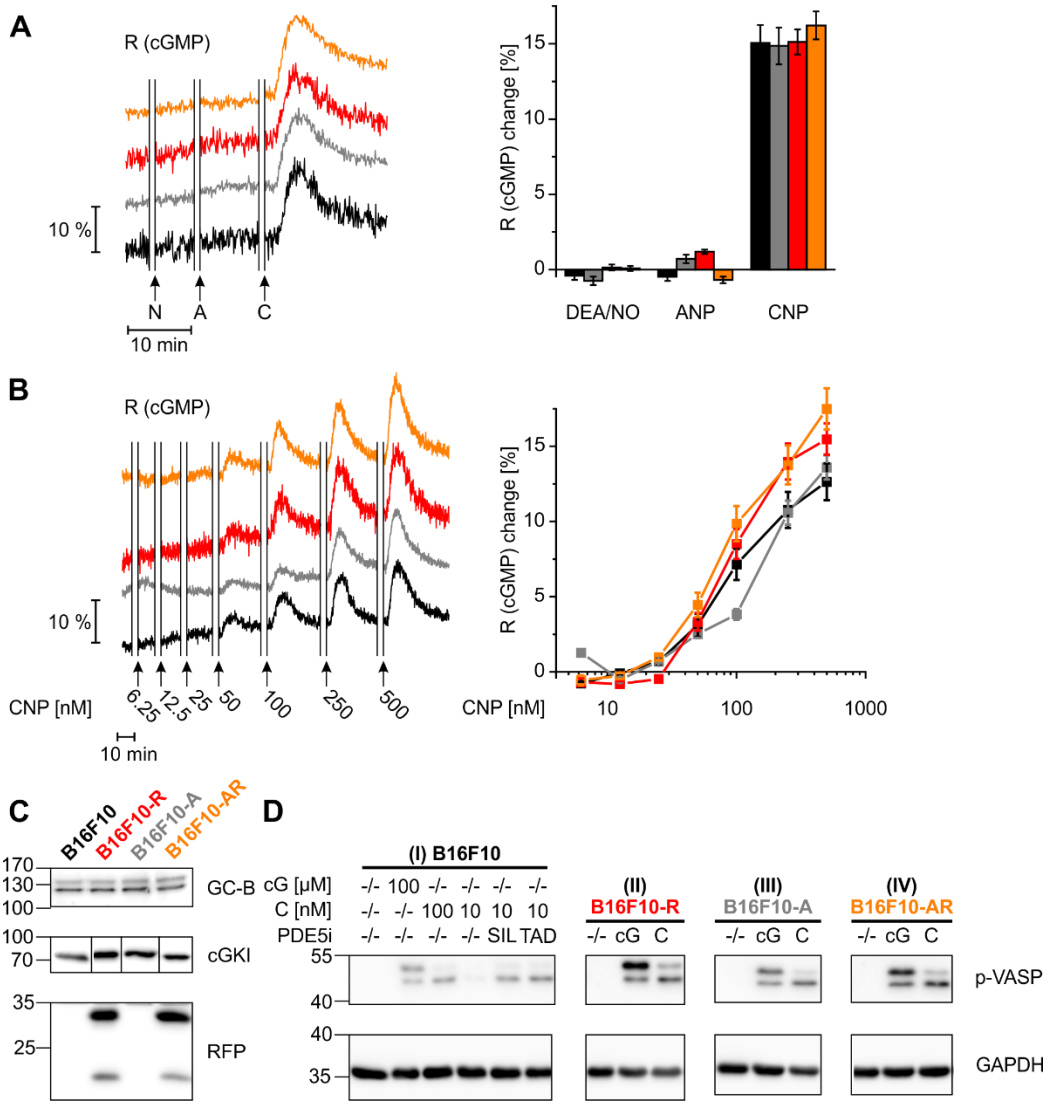

Figure 4: Amelanotic B16F10 cells represent an adequate model for fluorescence imaging in melanoma. B16F10 cells (**black lines/bars**) were genetically modified via CRISPR/Cas9 to render them amelanotic (**B16F10-A**; **gray lines/bars**), to express the red fluorophore mCherry (**B16F10-R**; **red lines/bars**), or both (**B16F10-AR**; **orange lines/bars**) (Tikoo et al., 2021). **(A)** The different B16F10 clones were transfected with pCMV-cGi500 and subjected to real-time FRET/cGMP imaging in the absence and presence of DEA/NO (N; 500 nM), ANP (A; 250 nM), and CNP (C; 250 nM). GC ligands were superfused for 2 min each. Representative R (cGMP) traces (left) and quantification of cGMP signals (right) induced by different GC ligands are shown (n ≥ 47 cells from ≥ 2 independent experiments). **(B)** In a different set of FRET/cGMP imaging experiments, cGi500-expressing B16F10 cells were superfused with increasing CNP concentrations for 2 min per concentration. Graphs show representative R (cGMP) traces (left) and quantification of CNP-induced cGMP signals (right) (n ≥ 40 cells). **(C)** Protein extracted from the different B16F10 clones was analyzed via SDS-PAGE followed by Western Blot. Immunostaining for GC-B, cGKI and RFP was performed. GC-B was detected in the membrane fraction after its enrichment as described in 0. **(D)** B16F10 (**I**), B16F10-R (**II**), B16F10-A (**III**) and B16F10-AR (**IV**) cells were incubated for 10 min at 37 °C and 6 % CO_2 with the cell-permeable cGMP analog 8-Br-cGMP (100 µM), CNP (100 nM, if not specified) or the PDE5 inhibitors sildenafil (30 µM) or tadalafil (100 nM) before analysis. Immunostaining for phospho(Ser239)-VASP (p-VASP) and GAPDH (as reference protein) was performed (n = 2 Western Blots). Data represent mean ± SEM. RFP, red fluorescent protein; cG, 8-Br-cGMP; C, CNP; PDE5i, PDE5 inhibitor; SIL, sildenafil; TAD, tadalafil. Part of these results was published in Tikoo et al. (2021).

Both B16F10 and B16F10-A cells were additionally modified to express the red fluorescent protein mCherry (referred to as B16F10-R and B16F10-AR, respectively) to allow for melanoma cell visualization during imaging experiments. To assess whether these genetic modifications affected the cells' cGMP signaling properties, B16F10, B16F10-A, B16F10-R and B16F10-AR cells were transfected with pCMV-cGi500. cGMP sensor expression as well as changes of the intracellular cGMP generation in response to NO, ANP and CNP were microscopically assessed. Furthermore, expression of cGMP pathway proteins as well as cGMP-induced protein phosphorylation were analyzed.

As assessed with real-time FRET/cGMP imaging, neither melanin-producing nor amelanotic B16F10 cells generated cGMP in response to DEA/NO (500 nM) or ANP (250 nM) (**Figure 4A**). The relative R (cGMP) changes in response to 250 nM CNP (**Figure 4A**) and the sensitivity to increasing CNP concentrations (**Figure 4B**; calculated EC_{50} between 100-200 nM in all B16F10 clones) were comparable between melanin-producing and amelanotic B16F10 cells. Note that saturating CNP concentrations were not reached in these experiments, impairing reliability and accuracy of EC_{50} calculation. In line with the cGMP imaging data, SDS-PAGE followed by Western Blot revealed no obvious differences in the GC-B and cGKI protein levels between the B16F10 clones (**Figure 4C**). In addition, RFP immunostaining confirmed the presence of the monomeric RFP derivate mCherry specifically in the cell lines B16F10-R and B16F10-AR (**Figure 4C**, bottom).

Next, the cGMP pathway in B16F10 cells was analyzed on the effector level. Phosphorylation of the known cGKI target VASP was used as an indicator for cGKI activity. B16F10 cells stimulated with the cell-permeable cGMP analog 8-Br-cGMP (100 µM) and CNP (100 nM) contained increased levels of phospho(Ser239)-VASP (p-VASP) when compared with unstimulated control cells (**Figure 4D I**). As opposed to stimulation with 100 nM CNP, 10 nM CNP induced very little VASP phosphorylation. The PDE5 inhibitors sildenafil (30 µM) and tadalafil (100 nM) elevated the VASP phosphorylation induced by 10 nM CNP to a level similar to that observed after stimulation with 100 nM CNP (**Figure 4D I**), indicating that PDE5 is expressed and involved in the degradation of CNP-induced cGMP in B16F10 cells. In the investigated clones B16F10-R,

B16F10-A and B16F10-AR, increases in p-VASP observed after application of 8-Br-cGMP (100 µM) and CNP (100 nM) were similar to that observed in B16F10 cells (**Figure 4D I-IV**). The same was true for the elevation of CNP (10 nM)-induced VASP phosphorylation by the PDE5 inhibitors sildenafil (30 µM) and tadalafil (100 nM) (**Figure S5**). Taken together, the murine melanoma cell line B16F10 was shown to express a functional CNP/GC-B/cGMP/cGKI pathway which triggers VASP phosphorylation as previously published by Dhayade et al. (2016). This pathway is not affected by tyrosinase deletion (B16F10-A), mCherry knock-in (B16F10-R), or the combination of both modifications (B16F10-AR).

3.4 NO-GC, GC-B and cGKI are expressed in blood vessel-associated cells in primary melanomas

With the newly established tool of amelanotic B16F10-A and -AR cells, characterization of cGMP signaling in the melanoma microenvironment with optical imaging was now feasible. Although melanoma cells were shown to express a functional CNP/GB-B/cGMP pathway, the source of CNP in melanoma tumors was not yet investigated. Furthermore, additional cells in the tumor could have the capacity to generate cGMP in response to CNP. To identify CNP- and GC-B-expressing cells in the melanoma microenvironment, B16F10-A cells were administered by intradermal injection into CNP-lacZ and GC-B-lacZ mice, respectively. These mice expressed β-galactosidase with a nuclear localization sequence in the gene loci of CNP or GC-B, enabling nuclear X-Gal staining in the target cells as described in 2.7.3. Importantly, the injected B16F10-A cells did not express the *lacZ* reporter, making them “invisible” for X-Gal staining independent of their CNP or GC-B expression. Tumors were allowed to grow for 10-14 days to a final size of ~150 mm^3, before they were dissected, fixed and cryosectioned. Frozen tumor sections were stained with X-Gal to identify *lacZ*-positive (i.e., CNP- or GC-B-expressing) stromal cells followed by CIH staining of the smooth muscle/pericyte marker SMA to visualize tumor blood vessels.

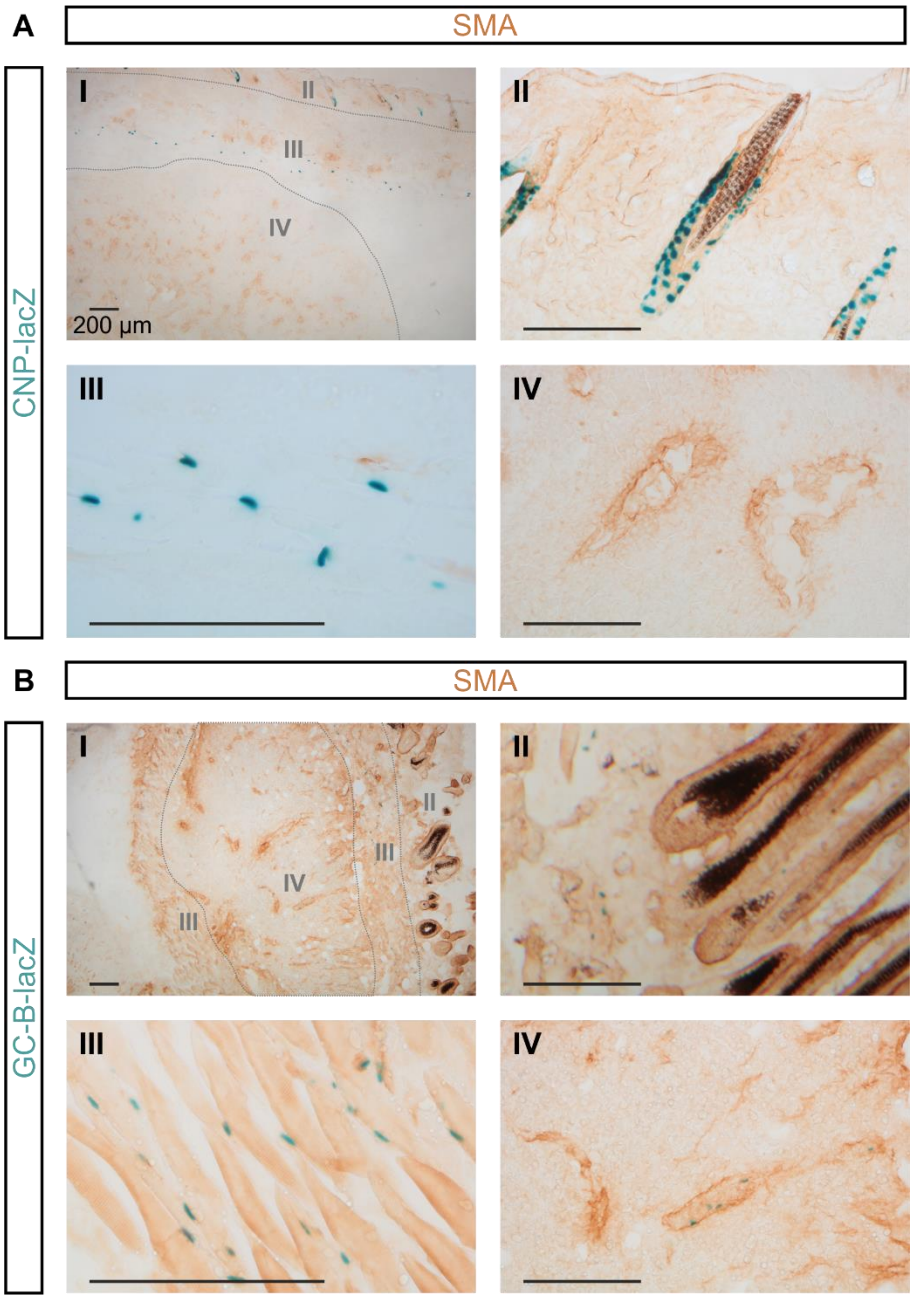

Figure 5: CNP expression is not detected inside the tumor, while GC-B is expressed in tumor vessel-associated cells. B16F10-A cells were administered by intradermal injection into **(A)** CNP-lacZ or **(B)** GC-B-lacZ mice. Tumors were allowed to grow for 10-14 days. Experimental animals were sacrificed and the tumors were dissected, fixed with Zambroni's fixative, and cryosectioned. Frozen sections were stained with X-Gal to identify *lacZ*-positive cells, and CIH staining of SMA (as smooth muscle/pericyte marker protein) was added to depict tumor blood vessels. Panels show brightfield pictures of the whole section (**I**), hair follicles (**II**), subcutaneous muscle (**III**) and tumor blood vessels (**IV**). Gray dashed lines in the overview picture indicate borders between the different tissues. Pictures are representative for n = 3 tumors dissected from 3 mice per genotype. Scale bars, 200 µm.

CIH staining of SMA visualized the tumor vasculature (**Figure 5**). Most of the tumor blood vessels had diameters of ~20-100 µm. No X-Gal staining was observed in the tumors of CNP-lacZ mice (**Figure 5A I**). In the tumor-surrounding tissue, however, CNP-positive cells were detected in hair follicles (**Figure 5A II**) as well as alongside subcutaneous muscle strands (**Figure 5A III**). No CNP-positive cells were found around the CIH-stained blood vessels (**Figure 5A IV**). In contrast to the results with CNP-lacZ mice, X-Gal staining of tumors of GC-B-lacZ mice revealed the presence of a small GC-B-positive cell population deep inside the tumor mass (**Figure 5B I**). These GC-B-positive cells inside the tumor were rare, but found exclusively in close proximity to tumor blood vessels (**Figure 5B IV**). GC-B-positive cells were also observed alongside subcutaneous muscle strands (**Figure 5B III**), but not in hair follicles (**Figure 5B II**) that were found to contain CNP-positive cells or in other structures of the tumor-surrounding tissue. Similar results were obtained in CD31-stained tumor sections of CNP-lacZ and GC-B-lacZ mice (data not shown). These findings demonstrated that GC-B is not only expressed in melanoma cells, but also in a specific yet uncharacterized cell type associated with tumor blood vessels, whereas CNP expression could not be detected anywhere in the tumor microenvironment.

In contrast to CNP/GC-B signaling, NO/NO-GC signaling was not detectable in melanoma cells (**Figures 3 and 4**). Therefore, it was of great interest to assess whether stromal cells within the tumor microenvironment express NO-GC, as this would allow targeted modulation of cGMP signaling without initiating the potentially deleterious effects of cGMP in melanoma cells. To look for NO-GC expression in the melanoma microenvironment, B16F10-A cells were administered by intradermal injection into wildtype B6 mice, and tumors were allowed to grow for 10-14 days to a final size of ~150 mm^3 before they were dissected, fixed and cryosectioned. Expression of NO-GC as well as CD31 as marker for endothelial cells and PDGFR-β as marker for pericytes was analyzed in the central tumor region.

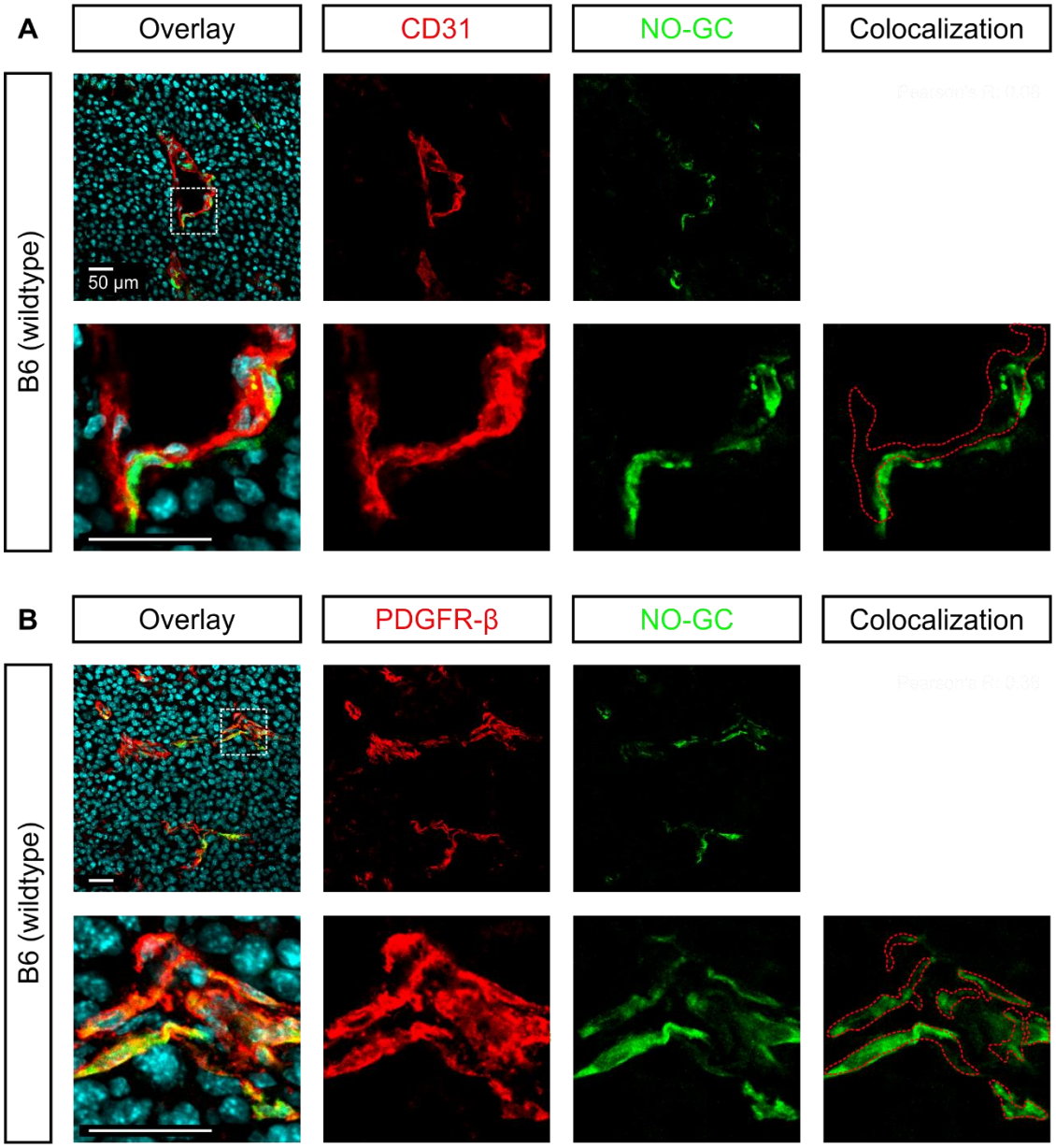

Figure 6: NO-GC is expressed in pericytes, but not in endothelial cells of tumor vessels. B16F10-A cells were administered by intradermal injection into wildtype B6 mice. Tumors were allowed to grow for 10-14 days. Experimental animals were sacrificed and the tumors were dissected, fixed and cryosectioned. Frozen sections were stained via IF for NO-GC as well as **(A)** CD31 as endothelial marker or **(B)** PDGFR-β as pericyte marker. Panels show (from left to right) an overlay picture (Cyan: nuclei (Hoechst 33258); Red: CD31 or PDGFR-β; Green: NO-GC; nuclei without associated immunostaining are likely to belong to tumor cells), CD31 or PDGFR-β staining, and NO-GC staining with low (top row) and high (bottom row) magnification. To identify colocalization, CD31 or PDGFR-β staining is indicated as red dashed line in a copy of the corresponding NO-GC picture (right image). Pictures are representative for n = 3 tumors dissected from 3 mice. Scale bars, 50 µm.

Similar to the CIH staining of SMA shown in **Figure 5**, IF staining of CD31 and PDGFR-β allowed visualization of tumor blood vessels with diameters of ~20-100 µm (**Figure 6**). NO-GC expression was detected in cells alongside some, but not all, tumor blood vessels. No overlap of NO-GC with CD31 staining was observed (**Figure 6A**). Instead, NO-GC seemed to be expressed in cells directly attached to the endothelium of tumor blood vessels (**Figure 6A**). In contrast to CD31, PDGFR-β staining clearly colocalized with NO-GC staining (**Figure 6B**). All NO-GC-positive cells in the tumor vasculature were also positive for PDGFR-β, indicating that NO-GC expression in B16F10 tumors is specific for pericytes of the melanoma vasculature. Vice versa, some PDGFR-β-positive cells were not stained for NO-GC, suggesting that there is also a population of NO-GC-negative tumor pericytes. Note that NO-GC is presumably a cytosolic protein, whereas CD31 and PDGFR-β are membrane proteins, leading to different subcellular distributions. Consistent with the Western Blot results (**Figure 3D**), NO-GC was not detected by IF in the CD31- and PDGFR-β-negative tumor areas, where mostly B16F10 cells would be expected (**Figure 6A and B**, nuclei without associated CD31- or PDGFR-β immuno-staining). Together, these results indicated that NO-GC is selectively expressed in a population of tumor pericytes, but not in B16F10 tumor cells, endothelial cells of the tumor vasculature, or other cell types in the tumor stroma.

The effects of cGMP in many tissues including the healthy vasculature are mediated via cGKI. Therefore, it was determined whether cGKI is also expressed in the abnormal tumor vasculature. Similar to the previous experiments, B16F10-A cells were administered by intradermal injection into wildtype B6 mice, and tumors were allowed to grow for 10-14 days to a final size of ~150 mm^3 before they were dissected, fixed and cryosectioned. Tumor sections were stained for cGKI as well as CD31 as endothelial cell marker and PDGFR-β as pericyte marker.

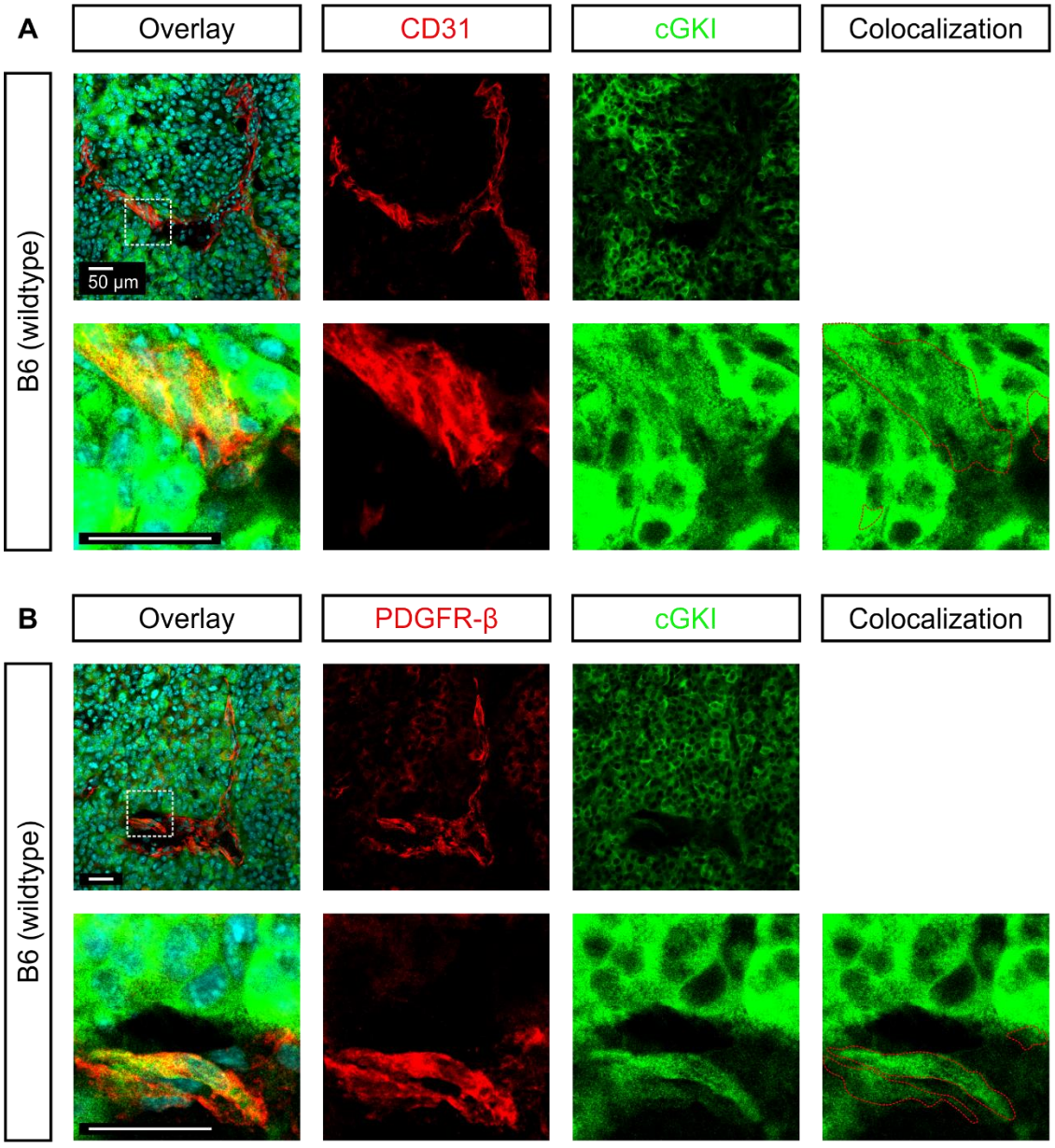

Figure 7: cGKI is expressed in several cell populations within the tumor, including B16F10 melanoma cells. B16F10-A cells were administered by intradermal injection into wildtype B6 mice. Tumors were allowed to grow for 10-14 days. Experimental animals were sacrificed and the tumors were dissected, fixed and cryosectioned. Frozen sections were stained via IF for cGKI as well as **(A)** CD31 as endothelial marker or **(B)** PDGFR-β as pericyte marker. Panels show (from left to right) an overlay picture (Cyan: nuclei (Hoechst 33258); Red: CD31 or PDGFR-β; Green: cGKI; nuclei without associated immunostaining are likely to belong to tumor cells), CD31 or PDGFR-β staining, and cGKI staining with low (top row) and high (bottom row) magnification. To identify colocalization, CD31 or PDGFR-β staining is indicated as red dashed line in a copy of the corresponding cGKI picture (right image). Pictures are representative for n = 3 tumors dissected from 3 mice. Scale bars, 50 µm.

IF staining revealed pronounced expression of cGKI in the tumor cells of primary B16 melanomas (**Figure 7A and B**, CD31- and PDGFR-β-negative areas). This observation was in line with the robust cGKI expression detected in cultured B16F10 cells via Western Blot (**Figures 3D and 4C**). In addition, cGKI was found to colocalize with both CD31 (**Figure 7A**) and PDGFR-β (**Figure 7B**), indicating that it might be expressed in endothelial cells and pericytes as well. Taken together, cGKI was broadly expressed in primary B16 melanomas, including the tumor cells themselves, endothelial cells and pericytes of the tumor vasculature, and perhaps other yet unidentified stromal cell types.

3.5 Endothelial cells and pericytes of the tumor vasculature generate cGMP in response to ANP and NO, respectively

To understand the mechanism(s) of action of cGMP signaling in melanoma, real-time *in situ* cGMP imaging was performed in acute tumor slices. This approach preserved both spatial and temporal information of cGMP generation. Thereby, cGMP signaling in different structures and cell types within the tumor could be compared under well-controllable conditions, e.g., in the presence and absence of drugs. For these experiments, B16F10-A cells were administered by intradermal injection into global (cGi-L1), endothelial cell-specific (TIE2-cGi) or smooth muscle/pericyte-specific (SMA-cGi; specificity and efficiency of SMA-CreERT2-mediated recombination in PDGFR-β-positive tumor pericytes demonstrated in **Figure S8**) cGMP sensor mice. In the tumors of cGi-L1 mice, all mouse-derived cells including the vasculature and all kinds of stromal cells constitutively expressed the cGMP sensor, whereas the tumor cells were cGi500-negative. In the tumors of cell type-specific cGMP sensor mice, all mouse-derived cells prior to recombination expressed mT as detailed in 2.3.2. Recombination induced a switch from mT to cGi500 expression specifically in the target cell population. Tumor cells were negative for both mT and cGi500. In all experiments, tumors were allowed to grow for 10-14 days to a final size of ~150 mm^3 before they were dissected. To enable real-time FRET/cGMP imaging experiments, the isolated whole tumors and tumor slices were kept vital by incubation in glucose-containing buffer on ice as described in 2.5.2.2. cGMP concentration changes in response to the physiological GC ligands CNP, ANP and NO as well as to the NO-GC stimulator riociguat were recorded.

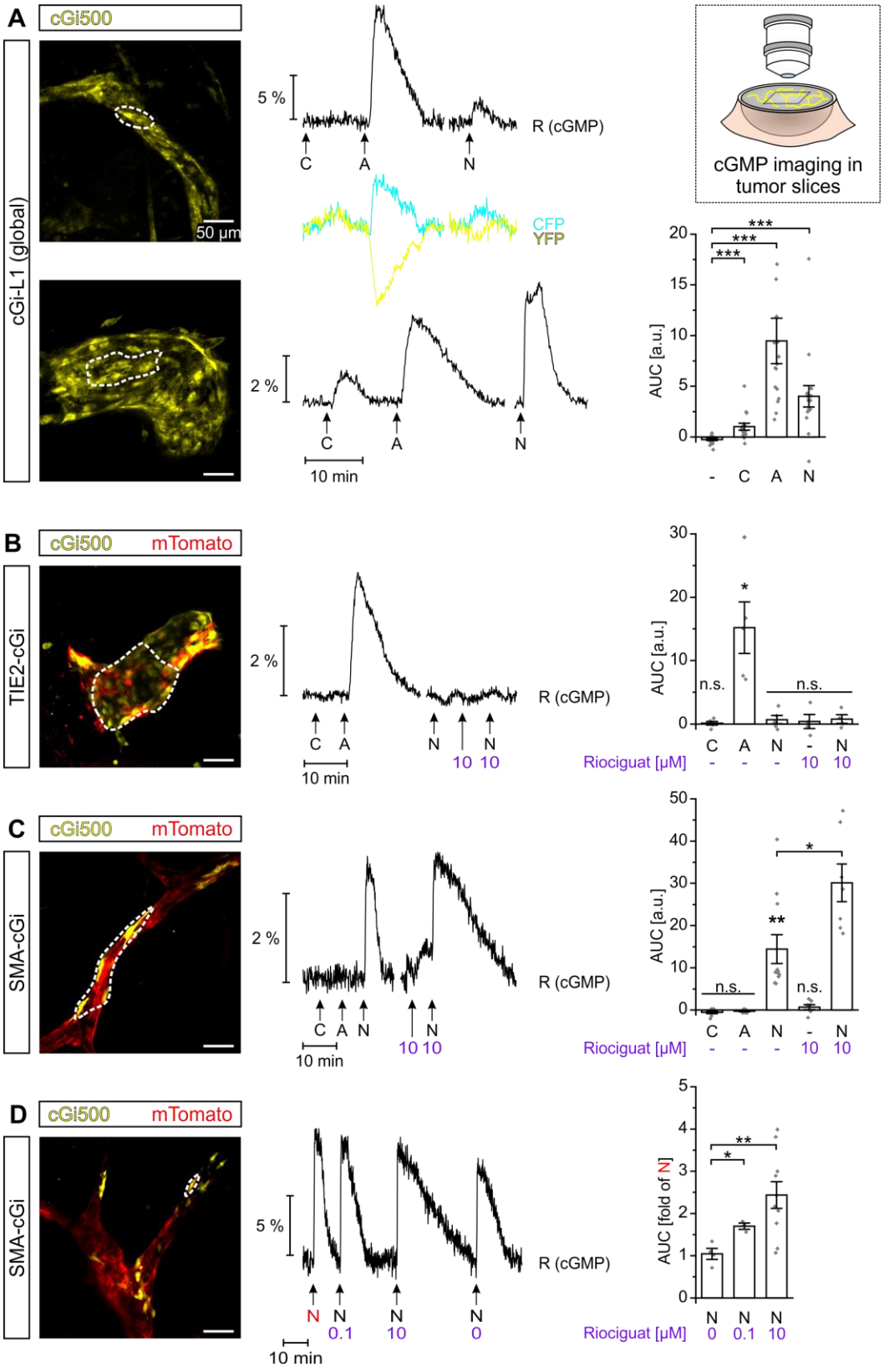
A
cGi500
cGi-L1 (global)
50 µm
5 %
R (cGMP)
C
A
N
CFP
YFP
2 %
10 min
cGMP imaging in tumor slices
AUC [a.u.]
***
***
***
- C A N
B
cGi500
mTomato
TIE2-cGi
2 %
R (cGMP)
C A N N
10 10
10 min
n.s.
*
n.s.
C A N - N
Riociguat [µM] - - - 10 10
C
cGi500
mTomato
SMA-cGi
2 %
R (cGMP)
C A N N
10 10
10 min
n.s.
**
*
n.s.
C A N - N
Riociguat [µM] - - - 10 10
D
cGi500
mTomato
SMA-cGi
5 %
R (cGMP)
N N N N
0.1 10 0
10 min
AUC [fold of N]
*
**
N N N
Riociguat [µM] 0 0.1 10

Figure 8: Tumor pericytes generate cGMP in response to NO, whereas endothelial cells are ANP-responsive. Amelanotic B16F10 cells were administered by intradermal injection into mice expressing cGi500 in the different tissues specified below. Tumors were allowed to grow for 10-14 days, before experimental animals were sacrificed and the tumors were dissected. Acute tumors slices were prepared and subjected to real-time FRET/cGMP imaging. During the recordings, the GC ligands CNP (C; 100 nM), ANP (A; 100 nM), DEA/NO (N; 10 µM), riociguat (concentrations as indicated), or a combination of 10 µM DEA/NO and riociguat were superfused for 2 min each. Shown are (from left to right) fluorescence images of the tumor slices, R (cGMP) and (where applicable) CFP and YFP traces corresponding to the representative regions indicated on the left (white dashed lines), and statistical analysis of the AUC of cGMP signals recorded after vehicle or GC ligand application. **(A)** FRET/cGMP measurements were performed with B16F10-AR tumors dissected from global cGi-L1 mice. Two representative regions with tumor vessels of different size are shown to account for the variability of the analyzed tumor vessels. Yellow color shows YFP fluorescence of cGi500, not cGMP. Red fluorescence derived from mCherry-expressing B16F10-AR cells was also observed, verifying that tumor tissue was analyzed (data not shown). **(B and C)** FRET/cGMP measurements were performed with B16F10-A tumors dissected from **(B)** endothelial cell-specific TIE2-cGi or **(C)** smooth muscle/pericyte-specific SMA-cGi mice. Yellow color shows YFP fluorescence of cGi500 and red color shows mT fluorescence of the non-recombined stromal cells. **(D)** To assess the concentration-response-relationship of riociguat on tumor pericytes, some of the B16F10-A tumors dissected from SMA-cGi mice were superfused with 10 µM DEA/NO together with varying concentrations of riociguat. The AUCs of the evoked cGMP signals were normalized to a reference application of 10 µM DEA/NO at the start of the recording (red-colored "N" in the R (cGMP) traces). Data represent mean ± SEM (n ≥ 5 tumors dissected from ≥ 3 mice). Scale bars, 50 µm.

cGMP sensor expression was readily detectable in the stroma of B16F10 tumors isolated from cGi-L1 mice (**Figure 8A**). The most prominent fluorescent structures were the tumor blood vessels which had diameters of ~20-100 µm, consistent with the observations made by immunostaining of tumor sections (**Figures 5, 6 and 7**). Other mouse-derived cGi500-expressing cells were rarely detected in the tumor stroma, and no cGMP signals were recorded in these non-vascular cells (**Figure 8A** and data not shown). Considering that cGi-L1 mice express the cGMP sensor globally in all cells, tumor vessels were apparently the major structures in the microenvironment of the analyzed B16F10 tumors. The cellular structure of tumor blood vessels was well visible, representing the vascular endothelium. However, larger tumor blood vessels > 100 µm diameter (like the one shown in **Figure 8A**, bottom panel) did not have the VSMC "rings" characteristic for healthy arteries and veins of similar size, indicating functional impairment of the tumor vasculature. The capacity of these tumor blood vessels to generate cGMP in response to endogenous GC ligands was assessed by FRET/cGMP imaging in acute tumor slices (**Figure 8A**, right panels). ANP (100 nM) and DEA/NO (10 µM) both strongly increased cGMP in the tumor vasculature (AUC of cGMP signals induced by ANP: 9 ± 2 a.u. and DEA/NO: 4 ± 1 a.u,). CNP (100 nM), albeit less potent than the other tested GC ligands, increased cGMP (1.0 ± 0.3 a.u.) in some, but not all of the analyzed regions.

Next, cell type-specific sensor mice were used to identify the cell type(s) responsible for cGMP generation in tumor vessels from cGi-L1 mice. In tumors of TIE2-cGi mice expressing cGi500 specifically in endothelial cells, YFP fluorescence of the cGMP sensor was detected as expected in the vascular wall with a pattern resembling the morphology of endothelial cells (**Figure 8B**). Some cells that were associated with these tumor blood vessels were not recombined as deduced from their mT expression, which could be explained by the presence of non-endothelial cells. Consistent with the lack of GC-B and NO-GC expression in tumor endothelial cells (**Figures 5 and 6A**), CNP (100 nM) as well as DEA/NO (10 µM) did not increase cGMP in the tumor endothelium of TIE2-cGi mice (**Figure 8B**). ANP (100 nM), on the other hand, induced robust cGMP signals (15 ± 4 a.u.) that were comparable to the ANP-induced cGMP generation in tumor blood vessels of cGi-L1 mice (**Figure 8A**). With the same setup, the NO-GC stimulator riociguat (10 µM) did not increase cGMP alone or in combination with DEA/NO (10 µM) (**Figure 8B**). Similar results were obtained with tumors of CDH5-cGi mice (data not shown).

Since tumor pericytes were identified to express NO-GC (**Figure 6B**), smooth muscle/pericyte-specific cGMP sensor mice (SMA-cGi) were also analyzed (**Figure 8C**). YFP fluorescence of the cGMP sensor in SMA-cGi mice was observed in spread single cells with finger-like extensions, resembling the morphology of pericytes. Supporting their pericyte identity, these YFP-positive cells were wrapped around mT-expressing tube-like structures that closely resembled the vascular endothelium. Again, the response pattern of recombined (yellow-fluorescent) cells to different cGMP-modulating substances was analyzed. CNP and ANP (both 100 nM) did not increase cGMP in tumor pericytes of SMA-cGi mice (**Figure 8C**). DEA/NO (10 µM), however, strongly induced cGMP generation in these cells, which was further potentiated by riociguat (10 µM) (without riociguat: 14 ± 3 a.u. and 10 µM riociguat: 30 ± 4 a.u.). Riociguat (10 µM) alone showed a trend to slightly elevate the basal R (cGMP), but this effect did not reach statistical significance (**Figure 8C**). Similar results were obtained with tumors of SM22-cGi mice (data not shown). The amplifying effect of riociguat on DEA/NO-induced cGMP generation was further assessed by means of a concentration response. Similar to previous experiments, application of 10 µM DEA/NO as reference stimulus induced robust cGMP signals in tumor pericytes of SMA-cGi mice (**Figure 8D**, red-colored “N”).

Subsequent co-application of riociguat further potentiated the cGMP generation induced by 10 µM DEA/NO in a concentration-dependent manner, which was not the case when vehicle (“0”; 0.1 % DMSO) was co-applied (vehicle control: 1.0 ± 0.1-fold versus 0.1 µM riociguat: 1.7 ± 0.1-fold versus 10 µM riociguat: 2.4 ± 0.3-fold of reference stimulus N). In summary, two cell types with unique cGMP signaling patterns could be identified in the melanoma tumor microenvironment: (1) endothelial cells that generated cGMP in response to ANP, but not to NO or CNP, and (2) pericytes that generated cGMP in response to NO, but not ANP or CNP. Accordingly, riociguat potentiated the NO-induced cGMP generation in pericytes, but not in endothelial cells. Together, these experiments suggested that within melanoma tumors, NO-GC modulators provide a powerful tool for the targeted stimulation of the cGMP pathway in vascular pericytes, without inducing potentially deleterious cGMP increases in the tumor cells.

3.6 Genetic ablation of NO-GC in tumor pericytes attenuates the growth of primary melanomas

Up to this point, the present study has shown that tumor pericytes have a fully functional NO/NO-GC/cGMP/cGKI signaling pathway. However, the pathophysiological role of cGMP in tumor pericytes was still unclear. To tackle this question, B16F10-A cells were injected into both flanks of smooth muscle/pericyte-specific NO-GC knock-out (NO-GCsmko) mice and control littermates that were heterozygous for the NO-GC mutation (NO-GCctrl). The CreERT2-controlled NO-GC knock-out was induced by two rounds of tamoxifen injection, the first one before establishment of the tumors at an age of 6 weeks, and the second one at an age of ~10 weeks starting 5 days after tumor cell injection as outlined schematically in **Figure 9A**. Tumor growth was monitored over the course of 14 days, before tumors were dissected, weighted and inspected by eye. Tissue samples of representative experimental animals were subjected to immunostaining (**Figures S6 and S7**) and Western Blot analysis (**Figure S9**).

Visual inspection of the tumors at the end of the experiment revealed that tumors of NO-GCsmko mice on average were smaller than tumors of NO-GCctrl mice (**Figure 9B**). In addition, NO-GCsmko tumors were paler than NO-GCctrl tumors, indicating that the blood flow in tumors of NO-GCsmko mice might be impaired.

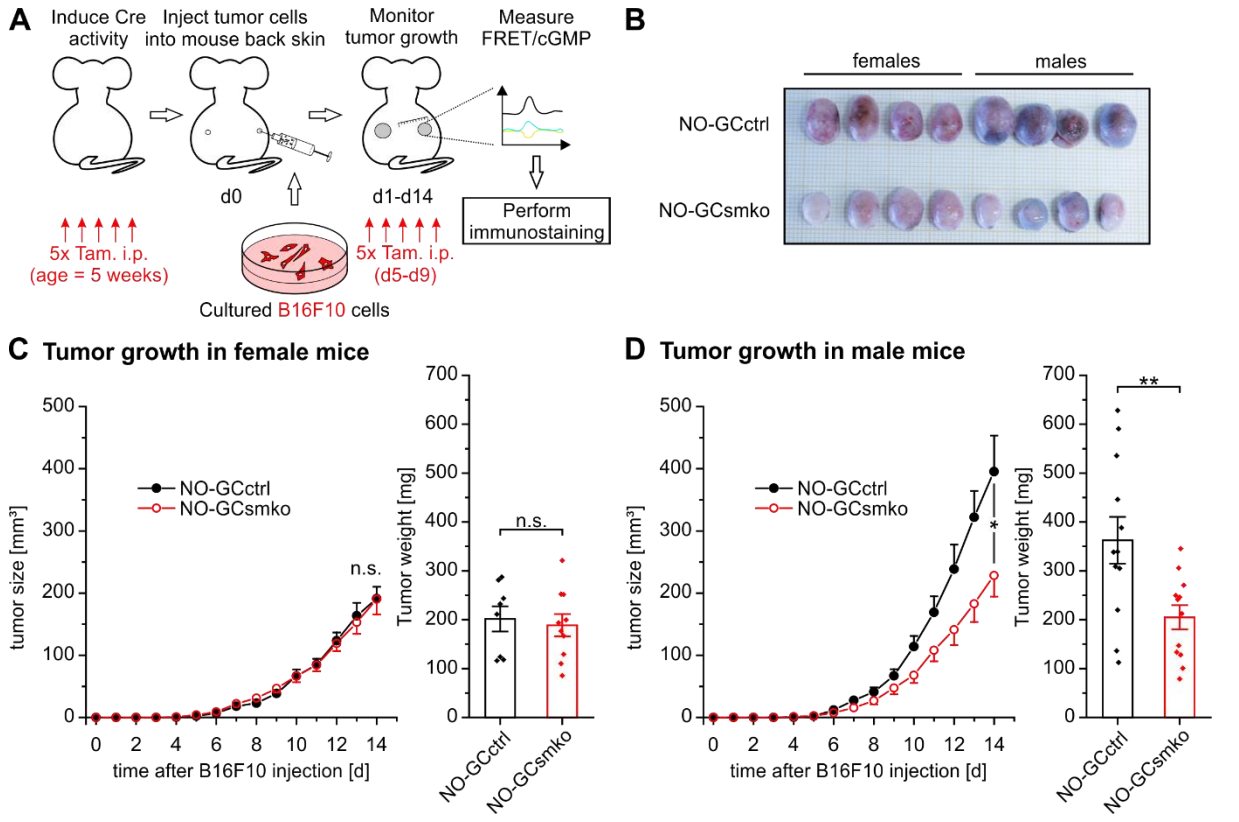

Figure 9: Impairment of the NO/cGMP signaling pathway in SMA-positive cells leads to decreased tumor growth. B16F10-A cells were administered by intradermal injection into NO-GCctrl or NO-GCsmko mice. Tumor size was determined daily. After 14 days, experimental animals were sacrificed, and tumors were dissected and further analyzed. **(A)** Graphical outline of the experimental procedures. **(B)** Image of representative tumors of female (left) and male (right) NO-GCctrl (top) and NO-GCsmko (bottom) mice after dissection on day 14. **(C and D)** Tumor growth (left) and tumor weight after dissection on day 14 (right) in **(C)** female and **(D)** male NO-GCctrl as well as NO-GCsmko mice. Data represent mean ± SEM (n = 12 tumors dissected from 6 mice per genotype).

Interestingly, while tumor growth was not significantly affected by NO-GCsmko in female mice (**Figure 9C**), male NO-GCsmko mice showed significantly reduced tumor growth as compared to their NO-GCctrl littermates (**Figure 9D**). These results were also reflected in the tumor weight after dissection on day 14 (**Figure 9C and D**, bar graphs on the right), which again was not affected by NO-GCsmko in female mice but strongly reduced in male NO-GCsmko mice. Together, these experiments suggested that the NO/NO-GC/cGMP signaling pathway in pericytes of the tumor vasculature is functionally relevant in melanoma development, most likely by affecting formation and/or homeostasis of the melanoma vasculature.

4 Discussion

This study demonstrated the pharmacological potential of NO-GC modulators to increase cGMP levels in the kidney and in tumor blood vessels, and has examined some features and preconditions of their respective modes of action. For the first time, the spatiotemporal dynamics of cGMP signals induced by NO-GC stimulators and activators were analyzed *in situ* using real-time cGMP imaging in live cells and tissues with a FRET-based cGMP biosensor. In line with existing *in vitro* data and functional studies, the results presented here suggested that NO-GC *stimulators* mainly potentiate the cGMP generation induced by endogenous NO under native conditions (Liu et al., 2021; Stasch et al., 2001), whereas NO-GC *activators* are able to provoke cGMP production by NO-GC under oxidative stress-conditions that render the enzyme unresponsive to NO (Hahn et al., 2021; Stasch et al., 2002). Thereby, NO-GC stimulators and activators might be able to restore cGMP signaling, and presumably improve tissue function, under disease-relevant conditions of reduced NO bioavailability and oxidative stress, respectively. This opens the gate to new targeting approaches for diseases with impaired NO/NO-GC/cGMP signaling.

4.1 Renal cGMP

In the kidney, robust NO- and ANP-induced cGMP signals were recorded in glomeruli as well as in perilobular blood vessels, whereas cells from the renal tubular system showed limited capability to increase cGMP in response to these substances (**Figure 1B, C and D**). NO-induced, but not ANP-induced cGMP generation was ODQ-sensitive (**Figure 1E**), presumably due to ODQ-triggered NO-GC oxidation. Since CKD is associated with oxidative stress – and impaired NO-GC/cGMP signaling might be a crucial driver of CKD (reviewed by Coppolino et al., 2018) – novel drugs restoring cGMP generation in the kidney under these pathophysiological conditions could prove efficacious for CKD treatment. Indeed, the NO-GC stimulator BAY-41 potentiated the NO-induced cGMP generation, and the NO-GC activator BAY-543 potently increased glomerular cGMP levels in the absence of exogenously added NO and in the presence of the NO-GC oxidant ODQ. A model for the effects of NO-GC activators in CKD kidneys is shown in **Figure 10**, and will be discussed in the following paragraphs.

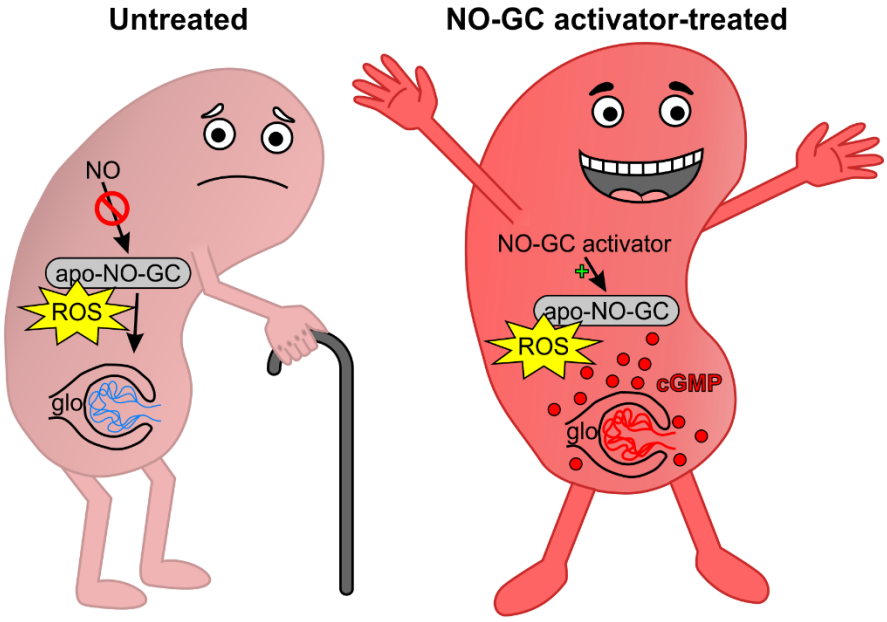

Figure 10: How NO-GC activators might restore kidney function under oxidative stress-conditions. Increased oxidative stress levels in CKD lead to impaired NO-GC/cGMP signaling in the diseased kidney. Glomerular arterioles are constricted and the intrarenal vascular resistance is high, which culminates in impaired renal blood flow. In contrast to the endogenous ligand NO, NO-GC activators like runcaciguat can induce cGMP generation by apo-NO-GC under oxidative stress-conditions. This leads to dilation of glomerular arterioles and improved renal blood flow. This illustration has been published as a graphical abstract together with the original study of Stehle et al. (2021). ROS, reactive oxygen species; glo, glomerulus.

4.1.1 Distribution of NO-GC in the kidney

Structures like glomeruli, blood vessels and renal tubules in kidneys of cGi-L1 mice (**Figure 1A**) were identified on the basis of different cell densities, varying cGi500 expression between cell types, and embedding in non-fluorescent extracellular matrix and body fluids. These structures accurately reflected these different structures as depicted by histological hematoxylin-eosin staining elsewhere (for example, see **Figure I5**, right panel). Supporting this statement, the detected NO-induced cGMP signals were in line with NO-GC expression patterns observed by Theilig et al. (2001). Their immunostainings indicated that within the kidney, NO-GC expression is highest in glomerular mesangial cells and the smooth muscle envelope of afferent and efferent arterioles, whereas epithelial and endothelial cells constituting most part of renal tubules and capillaries are NO-GC-negative. However, the study of Theilig et al. also revealed NO-GC expression in peritubular interstitial fibroblasts in cortex and medulla, where the NO-induced cGMP signals observed herein were weak (**Figure 1B**). In this context, it has to be considered

that CFP and YFP fluorescence from proximal non-responsive cells of global cGMP sensor mice might dampen relative R (cGMP) changes by artificially elevating the baseline. Either way, the present study did not directly identify the cell types showing cGMP signaling. This question could be addressed in the future by using cell type-specific cGMP sensor mice, for example, the SMA-cGi mice used herein (see also 2.3.2).

4.1.2 Physiological role of cGMP in the kidney

Consistent with the strong expression of NO-GC and robust NO-induced cGMP generation in glomeruli, collaborative experiments suggested that at least some of the beneficial effects of NO-GC modulators on the kidney are mediated by glomerular arterioles (Stehle et al., 2021). These experiments demonstrated that the NO-GC activator runcaciguat dilates isolated angiotensin II-pre-constricted glomerular arterioles in the absence of NO. Importantly, this NO-GC activator-induced vasodilation was observed in the presence of ODQ, where the effect of the NO donor S-nitroso-N-acetylpenicillamine was strongly and significantly weakened. Runcaciguat-induced vasodilation of renal arterioles was already detected under native, “non-oxidizing” conditions, but significantly lower runcaciguat concentrations were required after ODQ application. The authors continued to analyze the effect of NO-GC activators in an even more physiological setting by using isolated perfused kidneys (Stehle et al., 2021). They found that in the presence of ODQ, runcaciguat potently increased the perfusion rate as well as the perfusate’s cGMP concentration in these isolated kidneys, while the effects of S-nitroso-N-acetylpenicillamine again were abolished. These results indicated the presence of an oxidation-sensitive NO-GC/cGMP pathway in the renal vasculature that controls renal blood flow and can be restored under oxidative stress-conditions by treatment with NO-GC activators (working hypothesis illustrated in **Figure 10**).

In addition to its impact on the renal vasculature, there is evidence that NO-GC/cGMP in non-vascular cells also contributes to the observed beneficial effect of NO-GC activators on kidney function. Preclinical studies have reported anti-fibrotic and anti-inflammatory effects of NO-GC stimulators in various disease models involving liver and kidney (Hall et al., 2019; Schinner et al., 2017; Shea et al., 2020), which most likely are mediated via the NO-GC-expressing hepatic stellate cells and renal interstitial fibroblasts identified by

Theilig et al. (2001). The results of Schinner et al. (2017) indicated that increased NO-GC/cGMP in renal fibroblasts inhibits transforming growth factor β signaling and reduces production of extracellular matrix proteins as well as pro-inflammatory factors. Assuming the presence of oxidative stress in CKD, NO-GC activators might as well be effective under CKD conditions. Indeed, Benardeau et al. (2021) recently have found that the NO-GC activator runcaciguat exhibits cardio-renal protection in several rat CKD models by reducing proteinuria and attenuating kidney damage, with little to no effect on the systemic blood pressure. Along with the present study, the findings of Benardeau et al. (2021) highlighted the strength of NO-GC activators' novel and unique mode of action (i.e., their selectivity for heme-oxidized NO-GC; see also 1.1.4): They can induce beneficial effects in diseased tissues under oxidative stress-conditions without systemically affecting NO-GC/cGMP signaling in healthy tissues. Unsurprisingly, runcaciguat is currently investigated in phase II clinical trials in CKD patients with severe cardiovascular comorbidities (CONCORD; NCT04507061) and in patients with nonproliferative diabetic retinopathy (NEON-NPDR; NCT04722991). Together, the present and previous studies suggested that NO-GC modulators act on the renal vasculature to restore renal blood flow, but also on interstitial fibroblasts to reduce fibrosis in CKD kidneys under pathological conditions of oxidative stress and/or reduced NO bioavailability.

4.1.3 ODQ as oxidative stress-mimetic

In most studies (including the present one) that aimed to analyze heme-oxidized NO-GC, ODQ has been used as oxidative stress-mimetic. This inhibitor was shown to oxidize the NO-GC heme-cofactor, thereby lowering the enzyme's sensitivity to NO (Y. Zhao et al., 2000). Results shown in **Figures 1 and 2** clearly demonstrated that ODQ reduces the NO-induced cGMP generation in renal glomeruli in a concentration-dependent manner, whereas NO-GC-independent cGMP production by ANP/GC-A is not significantly affected (**Figure S4A**). These findings are in line with previous *in vitro* analyses (Garthwaite et al., 1995), where ODQ inhibited purified NO-stimulated NO-GC, but not ANP-stimulated GC-A. In the study of Garthwaite et al., 10 µM ODQ were sufficient to almost completely abolish NO-GC activity, while the kidney slices analyzed in the present work showed smaller, but still significant NO-induced cGMP signals after application of

50 µM ODQ (~33 % of NO-induced cGMP signals in the absence of ODQ; **Figure 1E**). However, it should be considered that in *ex vivo* measurements of kidney slices as performed herein, the drugs had to pass through cell membranes and, to reach deeper tissue regions, through whole cell layers that could scavenge the drugs. Therefore, drugs might reach the enzyme of interest at a lower concentration than initially applied.

Instead of ODQ, NO-GC oxidation *in vivo* is thought to be triggered by endogenous reactive oxygen species like peroxynitrite (Stasch et al., 2006). Although it seemed obvious to validate the results obtained after ODQ application using these pathophysiologically relevant substances, several problems were encountered when trying this approach. It took substantial concentrations of H_2O_2 (> 1 mM) or peroxynitrite (> 100 µM) to induce detectable changes in NO-GC reactivity. At these concentrations, H_2O_2 caused optical issues including bubble formation and baseline drift, and peroxynitrite appeared to induce cGMP generation on its own, presumably via decay-mediated NO release (**Figure S4B and C**). Thus, future experiments using a different approach will be necessary to study the relevance of pathophysiological reactive oxygen species on the NO-GC/cGMP signaling in CKD kidneys. For example, Jia et al. (2013) published a mouse model of adenine diet-induced CKD, which could be used to treat cGMP sensor mice prior to cGMP imaging with NO-GC activators.

4.1.4 ANP/GC-A/cGMP as drug target in the kidney

As mentioned earlier, ANP-induced cGMP generation in glomeruli apparently was not affected by ODQ (**Figure S4A**). This raises the question whether the ANP/cGMP signaling pathway could provide an alternative drug target under pathological oxidative stress-conditions in CKD patients. Indeed, ANP was reported to dilate renal arteries (Frees et al., 2021) and improve renal blood flow in animal models (Opgenorth et al., 1986). However, even if both NO- and ANP-based drugs mediate their effects via cGMP elevation, their associated signaling pathways could differ by (1) cGMP compartmentation *within* individual cells and (2) heterogeneity *between* different cell types in the analyzed tissue (R. Feil et al., 2021). In the context of cGMP compartmentation, it was hypothesized that cGMP produced by NO-GC or pGCs might be restricted to specific subcellular compartments (Piggott et al., 2006), for example, by

the involvement of different PDEs (Castro et al., 2006). Similarly, cell-to-cell heterogeneity with regard to GC and/or PDE expression could also result in different functional outcomes.

Interestingly, NO was shown to *increase* renin secretion in a PDE3- and cAMP-dependent manner in isolated perfused rat kidneys (Kurtz et al., 1998), whereas ANP was reported to *decrease* renin secretion in rats (Brands & Freeman, 1988) and dogs (Opgenorth et al., 1986). Although these studies suggested that renin secretion is oppositely affected by NO and ANP, it remains questionable whether intra- or intercellular heterogeneity is the reason for this discrepancy. In fact, the kidney is composed of several cell types which might respond differently to NO and NPs. In particular, NO-GC expression was not detected in (renal) endothelial cells (Theilig et al., 2001), but was demonstrated to mediate VSMC relaxation (Arnold et al., 1977; Furchgott & Zawadzki, 1980; Ignarro et al., 1987). The ANP receptor GC-A, on the other hand, was shown to be expressed in both endothelial cells (Sabrane et al., 2005) and VSMCs (Holtwick et al., 2002). Therefore, part of the ANP-induced cGMP generation in the kidney could be derived from endothelial cells, even though the functional role of endothelial cGMP is controversial (reviewed by Kuhn, 2012). Indeed, Opgenorth et al. (1986) only observed a mild and transient increase in renal blood flow in response to ANP, whereas NO and the NO-GC stimulator BAY-41 chronically increased the renal blood flow in another study (Boerrigter et al., 2003). Taken together, these studies indicated that the NO/NO-GC and ANP/GC-A pathways in the kidney are functionally different. Thus, although the present study reported robust increases in glomerular cGMP levels after ANP application, the clinical implications of GC-A in CKD remains to be investigated in dedicated experiments analyzing the effect of ANP on the GFR or other indicators of kidney function.

4.1.5 NO-GC modulator mode of action

The experiments presented here shed some light on the proposed modes of action of NO-GC stimulators and activators using an *ex vivo* model of *in situ* cGMP imaging. The NO-GC stimulator BAY-41 had a strong synergistic effect with NO, but did not significantly increase cGMP in the absence of NO and was ineffective in the presence of the NO-GC oxidant ODQ (**Figure 2A and B**). The missing effect of BAY-41 alone was unexpected,

given that previous studies have demonstrated that at least under *in vitro*-conditions, BAY-41 can both stimulate purified NO-GC in the absence of NO and potentiate its NO-induced catalytic activity (Stasch et al., 2001). Stasch et al. argued that NO-GC stimulation evoked by pharmacologically relevant BAY-41 concentrations (i.e., 10-100 nM) are sufficient to cause physiological effects. However, the *ex vivo* FRET/cGMP imaging results obtained with kidney slices in the present study suggested that the NO-synergistic aspect of NO-GC stimulators might be more important in intact tissues. This hypothesis is supported by the fact that *in vivo*, NO will be present under disease conditions, although potentially at lower concentrations (Zhang et al., 2021). Still, it remains possible that physiological effects are caused by cGMP concentrations below the detection limit of *in situ* cGMP imaging using cGi500.

In contrast to NO and BAY-41, the NO-GC activator BAY-543 potently increased cGMP in renal glomeruli in the presence of the NO-GC oxidant ODQ, but did not affect cGMP levels or NO-induced cGMP generation under native conditions in the absence of ODQ (**Figure 2C and D**). These findings are in line with the proposed mode of action of NO-GC activators, which are believed to bind to the unoccupied heme-binding pocket of NO-GC, either after loss of the enzyme's heme group or by active replacement of the loosely bound iron(III) heme (Surmeli & Marletta, 2012). Although this was not observed in the present study, there is evidence that NO-GC activators can also induce catalytic activity of native iron(II) NO-GC. Cinaciguat (BAY 58-2668), one of the pioneer NO-GC activators, was shown to activate purified NO-GC (Stasch et al., 2002), and cinaciguat (Wennysia et al., 2021) as well as runcaciguat (Stehle et al., 2021) dilated angiotensin II-pre-constricted glomerular arterioles in the absence of ODQ. However, in all studies that directly compared native with "oxidative stress" conditions, ODQ increased the sensitivity of NO-GC towards NO-GC activators (Stasch et al., 2002; Stehle et al., 2021). Either way, it is an intriguing concept that NO-GC activators could overcome the pathophysiological impairment of NO/NO-GC/cGMP signaling under oxidative stress-conditions, while having limited effects on healthy ("non-oxidized") tissue.

4.2 cGMP in melanoma

After the effects of NO-GC modulators on kidney slices had been analyzed, this study went on to uncover the involvement of the cGMP pathway in melanoma growth and progression. *In situ* characterization of the cGMP pathway in primary B16 melanoma revealed the presence of at least three cell types with unique cGMP signaling patterns: (1) Melanoma cells generated cGMP in response to CNP, but not NO or ANP (**Figure 3**). Besides the tumor cells, GC-B expression as analyzed with GC-B-lacZ mice (**Figure 5B**) as well as CNP-induced cGMP generation (**Figure 8A**) was limited to a small yet unidentified cell population closely associated with tumor blood vessels. (2) Endothelial cells generated cGMP in response to ANP, but not NO or CNP (**Figure 8B**). (3) Pericytes generated cGMP in response to NO, but not ANP or CNP (**Figure 8C and D**). Moreover, NO-GC immunostaining indicated that NO-GC expression within B16 tumors is restricted to the pericytes (**Figures 6B and S8**). This previously unknown modularity of cGMP signaling in melanoma opens new ways for targeted stimulation of the cGMP pathway in specific cell types without unwanted off-target effects. More precisely, previous studies have shown that cGMP in melanoma cells can cross-stimulate the MAPK pathway (Arozarena et al., 2011; Dhayade et al., 2016). Since these studies found several cGMP effectors including PDE5 and cGKI in various melanoma cell lines, promotion of the cGMP pathway at the effector level (e.g., with PDE5 inhibitors) might also increase growth and invasiveness of the melanoma cells. In strong contrast, stimulation of the cGMP pathway on the generator level using the NO-GC stimulator riociguat potentiated the NO-induced cGMP generation in pericytes (**Figure 8C and D**), but had no effect on endothelial cells (**Figure 8B**) or B16F10 melanoma cells (data not shown). This might prove useful for melanoma therapy, since the present study suggested NO-GC/cGMP signaling in pericytes to affect tumor growth, presumably by regulating formation and/or homeostasis of the melanoma vasculature. A model for the effects of NO-GC modulators on tumor pericytes is shown in **Figure 11**, and will be discussed in the following paragraphs.

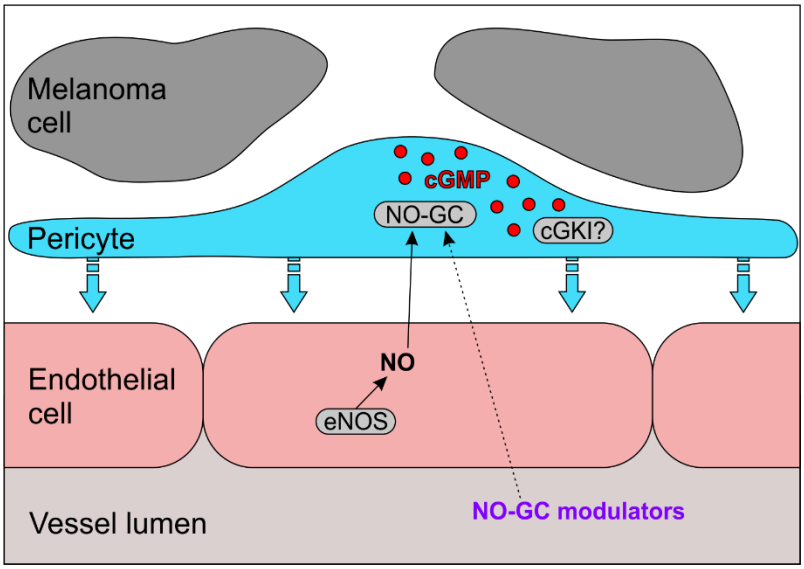

Figure 11: Proposed mechanism of NO-GC-dependent pericyte recruitment to newly formed tumor vessels. During (tumor) angiogenesis, endothelial cells release NO generated by eNOS, which can then diffuse through the tissue to reach pericytes or their precursors. NO stimulates cGMP generation by NO-GC in these cells, triggering their migration towards the newly formed blood vessel and maturation to functional pericytes. Similarly, cGMP generation in (tumor) pericytes can be induced by pharmacological NO-GC modulators like riociguat. Pericyte recruitment might be mediated by cGKI, since this cGMP effector is also expressed in tumor pericytes.

4.2.1 cGMP in melanoma and healthy melanocytes

Dhayade et al. (2016) have already demonstrated that B16F10 melanoma cells express a self-stimulating, growth-promoting loop of cGMP and MAPK signaling (see also **Figure I8**). Their results suggested that CNP-induced cGMP activates cGKI, which phosphorylates targets in the MAPK pathway. Stimulated MAPK signaling would then lead to inhibition of PDE5 and thereby further increased cGMP levels. Functionally, this signaling cascade increased B16F10 proliferation and migration *in vitro*, and pharmacological and genetic stimulation accelerated the growth of primary B16F10 tumors *in vivo*. Dhayade et al. also showed that at least parts of this pathway are present in several human melanoma cell lines. cGKI mRNA was found in most analyzed melanoma cell lines, and high cGKI expression in melanoma tissue correlated with shorter survival times of melanoma patients. Application of 8-Br-cGMP and CNP increased cGMP, p44/42 MAPK (Thr202/Tyr204) phosphorylation and cell growth of 1205Lu and WM3211 melanoma cells. Furthermore, CNP induced cGKI activity in 1205Lu, WM852, SKMel147 and (although very weakly) WM35 cells as determined by

VASP (Ser239) phosphorylation. The present study aimed to further improve our understanding of cGMP signaling in these human melanoma cell lines by analyzing cGMP generation as a measure of intracellular signal transduction. In line with the results of Dhayade et al. (2016), NO and ANP were not able to evoke cGMP signals in any of the tested melanoma cell lines, whereas CNP-induced cGMP generation was detected in B16F10, 1205Lu and SKMel147 cells (**Figure 3B and C**).

Interestingly, human A375 melanoma cells were also found to generate cGMP in response to CNP (**Figure 3B and C**), whilst expression of the cGMP effector cGKI could not be detected by Western Blot (**Figure 3D**). The latter finding was consistent with the very low cGKI mRNA levels in A375 cells reported by Dhayade et al. (2016). Neither Dhayade et al. nor the present study have analyzed CNP- or cGMP-induced VASP (Ser239) phosphorylation in A375 cells. However, previous *in vivo* studies with PDE5-overexpressing and control A375 cells indicated that cGMP has a pro-invasive effect on this cell type (Arozarena et al., 2011). The question remains how cGMP increases are translated into these physiological changes in the absence of cGKI in A375 cells. The results from Arozarena et al. suggested that the mechanism does not involve cGKs or the cGMP-regulated cAMP-specific PDEs, but might be mediated by cGMP/Ca^{2+} crosstalk. Overexpression of PDE5 in A375 cells resulted in lower cGMP and Ca^{2+} concentrations, which correlated with decreased myosin light chain 2 phosphorylation and invasiveness. It remains to be investigated whether CNG channels are involved in the cGKI-independent cGMP/Ca^{2+} crosstalk and thus might be the pro-invasive cGMP effectors in A375 cells, and possibly also in other (melanoma) cell lines.

In the melanoma cell lines WM3211 and WM852, real-time cGMP imaging did not reveal CNP-induced cGMP signals (**Figure 3B and C**). Conversely, Dhayade et al. (2016) by Western Blot detected increased levels of phospho(Thr202/Tyr204)-p44/42 MAPK in WM3211 cells and increased levels of phospho(Ser239)-VASP in WM852 cells following 10 min incubation with CNP (1 µM). The reason could be different detection limits of the used methods. It was already described for specific cell types that basal and stimulated cGMP concentrations were not in the dynamic range of the cGi500 biosensor. This, for example, was reported for adult cardiomyocytes, where regardless of cGMP's role in

cardiac contractility, cGMP visualization proved difficult until Gotz et al. (2014) generated a transgenic mouse line with cardiomyocyte-specific expression of a cGMP sensor more sensitive than cGi500 (red cGES-DE5; Niino et al., 2009). To analyze whether the cGMP levels in WM3211 and WM852 cells also require a more sensitive cGMP sensor, it would be necessary to repeat the experiments depicted in **Figure 3B** with these reporters.

Although NO was unable to trigger cGMP formation in melanoma cells, NO/NO-GC/cGMP was shown to be involved in UV radiation-induced melanogenesis by healthy human melanocytes (Romero-Graillet et al., 1996). The apparent loss of NO-responsiveness during malignancy was found to correlate with upregulation of NP/pGC/cGMP signaling and increased metastatic potential (Ivanova et al., 2001). The present study provided additional evidence that melanocytes lose NO-GC expression during melanoma development which renders them NO-unresponsive, while CNP/GC-B-mediated cGMP generation was readily detected.

To date it is unclear where the CNP that acts as ligand of the melanoma cells' GC-B is generated *in vivo*. Dhayade et al. (2016) hypothesized that melanoma cells might be stimulated by CNP released from the inflamed endothelium. However, X-Gal staining of B16F10 tumors of CNP-lacZ mice did not confirm CNP expression in the tumor endothelium (**Figure 5A**). Indeed, the experiment failed to identify any source of CNP within the B16F10 tumor stroma, while cells associated with hair follicles and subcutaneous muscle tissue clearly were CNP-positive (**Figure 5A**). It has to be mentioned, however, that the B16F10-A cells used in this experiment did not express the CNP-lacZ reporter. Thus, B16F10 cells (and of course also other melanoma cells) might secrete CNP in an autocrine manner. In addition, although X-Gal staining involves an enzymatic amplification step, its sensitivity of course is limited. As discussed by Kramer et al. (2021), it should be taken into account that (1) a certain number of β-galactosidase enzymes is required for a positive X-Gal staining, which might be different for the assessed gene (i.e., *Nppc*/CNP) and (2) factors that are not dependent on the promoter, like protein half-life and time-restricted protein expression, can lead to "false-negative" readouts. Since CNP is considered a mainly auto- and paracrine factor, even low expression levels could result in sufficient local CNP concentrations to induce cGMP

generation in responsive cells. Of note, CNP was also found in low concentrations in the circulation, which was associated with regulation of the vascular tone (Clavell et al., 1993). Therefore, it is possible that stimulation of melanoma cell GC-B/cGMP signaling is triggered by circulating CNP. Finally, the B16 melanoma is generally considered poorly immunogenic, whilst immunotherapy yields promising results in the treatment of human melanoma (discussed in 1.3.3). This means that the lack of CNP-lacZ detection in B16F10 melanoma could be caused by missing inflammation. Still, inflamed endothelium (and presumably CNP generation) might be present in many human melanoma patients. This question could be addressed by using modern techniques with single cell resolution, like single-cell RNA-sequencing, on human melanoma samples.

Melanin pigmentation makes melanoma a challenging tissue for microscopic imaging. As outlined by Tikoo et al. (2021), melanin interferes with optical imaging by two means: (1) The pigment's absorption of excitation and emission light limits the depth in which imaging is feasible to the outermost areas of the tumor. (2) Absorption of high-intensity excitation light induces cell death of the melanin-bearing tumor cells (called "speckling" by the authors), which *in vivo* and perhaps *ex vivo* might trigger an inflammatory response. The authors reasoned that amelanotic B16F10 cells without the capability to produce melanin would prove useful for microscopic imaging of melanomas under close-to-native conditions. To generate amelanotic B16F10 cells, Tikoo et al. (2021) used a CRISPR/Cas9-assisted gene editing approach to knock out tyrosinase, an enzyme crucial for melanin biosynthesis. Indeed, the pigmentation-dependent shortcomings regarding penetration depth and speckling were overcome by tyrosinase deletion, while proliferation and migration rates, tumor growth and immune cell-infiltration were unaffected (Tikoo et al., 2021). The present study compared cGMP signaling in these amelanotic, tyrosinase knock-out B16F10 cells (B16F10-A and B16F10-AR) with their melanin-producing counterparts (B16F10 and B16F10-R). Real-time cGMP imaging and Western Blot analysis revealed no obvious differences in GC ligand-induced cGMP generation, expression of cGMP-associated proteins, and cGMP-dependent protein phosphorylation between the different B16F10 clones (**Figures 4 and S5**). These results demonstrated that the amelanotic B16F10 cells generated by Tikoo et al. provide a valuable new tool to study the cGMP pathway in melanoma using fluorescence-based biosensors.

4.2.2 Physiological role of cGMP in the tumor microenvironment

As discussed in 4.2, various cell types inside the tumor (i.e., tumor cells, pericytes and endothelial cells) show completely different response patterns to physiological and pharmacological GC ligands. To take advantage of this new knowledge, it will be necessary to identify the physiological role of NO- and ANP-induced cGMP in tumor pericytes and endothelial cells, respectively. A first insight into the pathophysiological relevance of NO-GC/cGMP in tumor pericytes is given in **Figure 9**. Smooth muscle/pericyte-specific NO-GC knock-out significantly reduced B16F10 tumor growth in male mice, presumably by limiting the intra-tumoral blood flow. This hypothesis is in line with a previous study by Kashiwagi et al. (2005), who demonstrated that endothelial cell-derived NO recruits pericyte precursors to newly formed B16 tumor blood vessels and thereby stabilizes them. Since previous studies had observed similar effects depending on cGMP (Brown et al., 1999; Yamahara et al., 2003) – and NO-GC is the canonical NO receptor – Kashiwagi et al. hypothesized that NO-induced recruitment of pericytes to tumor vessels might be mediated via the NO-GC/cGMP/cGKI cascade. Indeed, NO-GC (**Figure 6B**) and cGKI (**Figure 7B**) were found to be expressed in tumor pericytes, and DEA/NO induced cGMP generation in these cells in live tumor tissue which was further potentiated by the pharmacological NO-GC stimulator riociguat (**Figure 8C and D**). Taken together, the results of Kashiwagi et al. (2005) and the work presented here suggested that during tumor angiogenesis, NO released by endothelial cells might recruit pericytes to newly formed blood vessels by stimulating the pericytes' NO-GC/cGMP cascade, thereby improving vessel function. The tumor pericytes' NO-induced cGMP generation at least *ex vivo* could be augmented by pharmacological NO-GC stimulation. A working hypothesis for this interaction is given in **Figure 11**.

How NP/GC-A/cGMP signaling might be involved in endothelial regulation is a controversially discussed topic (reviewed by Kuhn, 2012). While most studies agree that endothelial cells are equipped with this pathway's key proteins and that it is involved in the regulation of vascular permeability and angiogenesis, the direction of this modulation was reported to be different depending on physiological (i.e., vessel type, inflammation and hypoxia) and experimental (i.e., *in vitro* versus *in vivo*) parameters (Kuhn, 2012). Therefore, it seems impossible to predict the outcome of NP/GC-A/cGMP modulation in

the endothelium of tumor vessels without direct experimental evidence. To analyze these dependencies in melanoma, the experiment shown in **Figure 9** could be repeated with endothelial cell-specific GC-A knock-out mice. Of note, the appropriate genetic tools including endothelial cell-specific Cre mouse lines (Kisanuki et al., 2001; Sorensen et al., 2009) and constitutive (Lopez et al., 1995) as well as conditional (Holtwick et al., 2002) GC-A knock-out mice already exist. However, although these experiments alone would be valuable in improving our understanding of the mechanisms underlying tumor angiogenesis and tumor vessel maturation, the tools to pharmacologically intervene with ANP/GC-A-dependent cGMP generation are limited. To date, no selective GC-A agonist has reached clinical approval, and substances inhibiting NP degradation (e.g., sacubitril) are not specific for distinct NPs and most likely would also increase the potentially deleterious CNP-induced cGMP in melanoma cells. Therefore, we are far from utilizing endothelial GC-A as drug target in cancer. However, additional studies unravelling the role of cGMP in the endothelium under different environmental conditions and development of selective and potent GC-A agonists together have the potential to change this in the future.

Previous studies have reported cGMP-associated effects in additional stromal cell populations, more precisely in myeloid-derived suppressor cells (Meyer et al., 2011; Serafini et al., 2006) and cancer-associated fibroblasts (Catalano et al., 2019). In both cell types, upregulation of the cGMP pathway via PDE5 inhibition had anti-tumor effects, suggesting them as candidates for cGMP-based therapies. However, these studies did not examine the signaling upstream of cGMP, and the present study did not detect GC-B (**Figure 5**) or NO-GC (**Figure 6**) expression in the tumor that could be attributed to immune cells or fibroblasts based on localization and morphology. Of course, it remains possible that their GC expression just did not reach the detection limit of the used techniques, or that they express GC-A as cGMP generator which was, however, not the focus of the present study. That being said, real-time cGMP imaging only rarely revealed cGMP generation that was not directly associated with tumor blood vessels (data not shown). Given the robust cGMP generation in melanoma cells, endothelial cells and tumor pericytes (**Figure 8**), it anyway seems unlikely that cGMP increases in other cell types can be achieved without covering at least one of the named cell populations.

4.2.3 Impact of sex on B16F10 tumor growth and the cGMP pathway

The experiments analyzing B16F10 progression *in vivo* revealed a markedly faster tumor growth in male than in female experimental mice under control conditions (NO-GCctrl male: 395 ± 58 mm^3 versus female: 191 ± 19 mm^3 on day 14; **Figure 9C and D**). This is not the first study reporting sex-specific differences in melanoma growth. Dakup et al. (2020), for example, observed lower T cell counts in the blood and tumors of B16F10 tumor-bearing male as compared to female mice, which correlated with faster tumor growth. They hypothesized that the female anti-tumor immune response is stronger than that of males, and that the female immune system slows down melanoma growth.

Interestingly, smooth muscle/pericyte-specific NO-GC knock-out as performed in the present study reverted this sex-dependent difference in B16F10 tumor growth (NO-GCsmko male: 228 ± 34 mm^3 versus female: 190 ± 24 mm^3 on day 14). It will be important to clarify why deletion of NO-GC in female NO-GCsmko mice did not affect tumor growth. The reason could lie within the cGMP signaling pathway itself. Sex differences in the expression of eNOS in endothelial cells or NO-GC in tumor pericytes, as well as different sensitivity of female and male pericytes to NO, might affect the relevance of NO/NO-GC/cGMP signaling for pericyte recruitment to tumor vessels in female and male mice. Similarly, associated or compensatory pathways could be regulated in a sex-specific manner. Indeed, there is evidence for a sex-specific regulation of the NO/NO-GC/cGMP pathway in the cardiovascular system. eNOS knock-out has been suggested to induce cardiac dysfunction and pulmonary hypertension in adult male, but not female mice (W. Li et al., 2004; Miller et al., 2005). Similarly, knock-out of the NO-GC α1-subunit induced hypertension (Buys et al., 2008) and impaired the response to vascular injury (Vermeersch et al., 2009) in male, but not in female mice. Furthermore, Vermeersch et al. (2009) observed that aortic cGMP levels were strongly reduced by NO-GC α1 knock-out in mice of both sexes, but were 4-fold higher in female than in male mice of either genotype. The authors hypothesized that a “threshold” cGMP level might be sufficient for vascular homeostasis, which can be maintained in female mice with NO-GC α1 knock-out. This threshold cGMP level could potentially be achieved by NO-GC2 or pGCs. Even though knock-out of the NO-GC β1-subunit was shown to deplete both NO-GC1 and NO-GC2 (Friebe et al., 2007), the NP/pGC system remained

intact in the present study. In conclusion, these studies demonstrated that the NO/NO-GC/cGMP pathway is tightly regulated in a complex, sex-dependent manner, with various factors such as testosterone levels (Buys et al., 2008) as well as the genetic and metabolic predisposition (Buys et al., 2012; Dordea et al., 2016) contributing to the observed phenotypes. From this perspective, the different effect of NO-GCsmko on male and female mice (**Figure 9C and D**) seems comprehensible. Beyond that, the present work – in addition to all the studies discussed above – should be considered a wake-up call to any researcher who limits experiments to animals of one sex, which commonly is done to limit variability in tumor growth experiments.

Of note, tumors isolated from both female and male NO-GCsmko mice appeared paler than the tumors of same-sex NO-GCctrl mice (**Figure 9B**). Although direct evidence is missing and the question certainly deserves additional investigation, this observation indicated that the intra-tumoral blood flow might be affected in mice of both sexes. As discussed in 1.3.4, modulation of the tumor vasculature has double-edged sword character. Although high dose anti-angiogenic treatment depletes the tumor's nutrient and oxygen supply, it also impairs the anti-tumor immune response (Y. Huang et al., 2012). Considering the results obtained by Dakup et al. (2020), the presumably reduced intra-tumoral blood flow in NO-GCsmko mice might attenuate the T cell-mediated anti-tumor immune response, with a greater impact on female than male mice due to their higher T cell numbers. Importantly, sex differences in the efficacy of angiogenesis inhibitors were also observed in human patients although the underlying mechanisms are not yet understood (Cignarella et al., 2021). In summary, it seems worth performing further experiments that account for potential differences in the regulation of cGMP signaling, angiogenesis, and anti-tumor immunity between male and female experimental animals.

4.2.4 Limitations of the SMA-CreERT2-mediated NO-GCsmko

As highlighted in 1.1, the NO/NO-GC/cGMP pathway plays a crucial role in VSMC relaxation and, as a result, regulation of the vascular tone. Consequently, knock-out of the NO-GC β1-subunit (which depletes both NO-GC1 and NO-GC2) was reported to induce chronic hypertension in both male and female mice (Friebe et al., 2007). A similar increase of the systolic blood pressure in male mice was observed by Groneberg et al.

(2010) after smooth muscle-specific NO-GC deletion mediated by the tamoxifen-inducible SMMHC-CreERT2. In these smooth muscle-specific NO-GC knock-out mice, the systolic blood pressure gradually increased after induction of recombination starting at day 5-10 after the first tamoxifen injection and plateauing at day 20-30. Assuming that the SMA-CreERT2-controlled NO-GCsmko performed herein had a similar effect on the blood pressure, these mice would have developed severe hypertension by the time of B16F10 cell injection. Therefore, it cannot be excluded that the decreased tumor growth in male mice with NO-GCsmko (**Figure 9D**) was caused by its systemic effects, and it will be an important challenge for future experiments to decipher the cellular mechanisms underlying the observed phenotype.

There is also strong evidence that tamoxifen, which was used to induce CreERT2-mediated recombination, does not behave as an inert substance in the murine system but can directly affect processes including metabolism (Stout et al., 2021; L. Zhao et al., 2020), endothelial healing (Blum et al., 2021; Zahreddine et al., 2020), and angiogenesis (Blackwell et al., 2000; Gagliardi & Collins, 1993). The studies of L. Zhao et al. (2020) and Blum et al. (2021) in addition found the observed tamoxifen effects to be sex-specific. Furthermore, there are several reports of gene deletion-independent effects of tamoxifen-activated CreERT2 that were not induced by tamoxifen alone. For example, Y. Li, Choi, et al. (2014) observed complete regression of p53 knock-out lymphomas after tamoxifen-induced ubiquitin C-CreERT2 activation without additional insertion of loxP sites. In a different study, Brash et al. (2020) reported impaired retinal angiogenesis in the presence of tamoxifen-induced CDH5-CreERT2 and PDGFR-β-iCreERT2, which was neither detected in CDH5-CreERT2 mice without tamoxifen injection nor in tamoxifen-treated wildtype and TIE2-Cre mice. The authors concluded that experiments utilizing CreERT2-mediated gene editing should include tamoxifen-injected, CreERT2-containing control mice lacking only the floxed genes to exclude flawed results caused by CreERT2 toxicity. Although the present study took these considerations into account (see 2.3.2 for genotypic information on NO-GCsmko and NO-GCctrl mice), it still remains possible that tamoxifen- or CreERT2-induced artifacts triggered, for example, the sex differences in B16F10 tumor growth in NO-GCsmko mice (**Figure 9C and D**).

Finally, it should be noted that in the present study, NO-GC expression in NO-GCsmko aortae was not completely abolished (**Figure S9**), indicating that the smooth muscle/pericyte-specific recombination was incomplete. Especially with regard to sex-dependent differences in aortic cGMP levels and regulation of cGMP signaling (see 4.2.3), residual non-recombined VSMCs and pericytes might be able to maintain functions such as vascular contractility and integrity under given circumstances.

In conclusion, it might be worthwhile for future experiments to (1) increase recombination efficiency in tumor pericytes (e.g., by using a constitutive Cre mouse line) and (2) limit recombination to (tumor) pericytes with a better-suited Cre expression-driving promoter. However, achieving both efficient and specific recombination in tumor pericytes at the same time might be challenging, considering the largely overlapping "marker" protein expression patterns of VSMCs and pericytes (reviewed by Armulik et al., 2005). Nevertheless, Cre mouse lines have been generated for the most used pericyte markers, PDGFR-β (Cuervo et al., 2017; Foo et al., 2006), chondroitin sulfate proteoglycan NG2 (LeBleu et al., 2013; Zhu et al., 2011), and desmin (Gary-Bobo et al., 2008).

4.2.5 Potential melanoma therapy options based on the cGMP pathway

As discussed in 1.3.4, several studies have proposed vascular normalization as novel option to support anti-cancer therapies, for example, in melanoma. Unfortunately, conventional anti-angiogenic therapy with VEGF inhibitors tends to have severe dose-dependent adverse effects including hypertension (reviewed by Versmissen et al., 2019), which could be harmful to patients with hypertension-related comorbidities. Recent studies aimed to overcome these shortcomings of VEGF-based anti-angiogenic therapies. Kahn et al. (2021) performed large-scale transcriptome analysis of cancer patients' tumor vasculature. They found huge heterogeneity in the tumor vasculatures, and successfully identified two metrics to predict the efficacy of VEGF inhibition in individual patients. Sun et al. (2021) demonstrated that CD93 contributes to the abnormal tumor vasculature and CD93 blockade promotes vessel maturation. Importantly, this vascular normalization correlated with an increased response to chemotherapy as well as ICB.

The NO system has also been suggested for vascular normalization (reviewed by Mintz et al., 2021). The experiments presented here indeed provided evidence for NO-GC as an alternative drug target to improve tumor vessel function, perhaps by recruiting pericytes to tumor blood vessels thereby regulating vessel diameter and integrity. Importantly, pharmacological NO-GC stimulation is not associated with hypertension, but depending on the dosage can even lower the systemic blood pressure (Rothermund et al., 2000) which might be advantageous in hypertensive patients. Although direct *in vivo* evidence has not yet been provided, *in situ* cGMP imaging indicated that NO-GC stimulators pharmacologically increase the tumor pericytes' cGMP generation, which might induce vascular normalization.

As discussed in 1.1.4, the growing line-up of NO-GC modulators enables us to restore dysfunctional NO-GC/cGMP signaling under conditions of reduced NO bioavailability and oxidative stress. This comes in handy, since the tumor microenvironment was shown to contain high levels of reactive oxygen species (Fiaschi & Chiarugi, 2012). Considering their oxidative stress-dependent mode of action, NO-GC activators might even be able to specifically increase cGMP in the tumor while limiting potential off-target effects on the systemic circulation. However, the experiments described here only assessed the NO-GC stimulator riociguat, and whether NO-GC activators also can increase cGMP in tumor pericytes is yet to be analyzed.

Taken together, the present study provided evidence that pharmacological NO-GC stimulation specifically increases cGMP in tumor pericytes, where it could be involved in the regulation of the intra-tumoral blood flow. With this, the working hypothesis can be proposed that NO-GC modulators induce vascular normalization in melanoma in a way independent of traditional targets like VEGF-A (**Figure 11**). This might prove useful as co-therapy for all kinds of anti-cancer treatments in melanoma patients in which conventional therapies fail to achieve full recovery.

4.3 Conclusions and outlook

The real-time *in situ* cGMP imaging presented here shed some light on the molecular mechanisms of GC activation by endogenous as well as pharmacological ligands. In the kidney, NO-GC/cGMP stimulation was shown to dilate renal arterioles and improve the renal blood flow (Stehle et al., 2021). The observed beneficial effects of NO-GC activators in the kidney are already translated in a phase II clinical trial in CKD patients (CONCORD; NCT04507061). In primary melanoma, NO-GC/cGMP signaling was observed selectively in tumor pericytes, suggesting a role in the regulation of the tumor vasculature. In line with the working hypothesis that the pericytes' NO-GC/cGMP signaling is crucial for tumor vessel maturation, NO-GCsmko strongly reduced the B16 tumor growth in male mice, presumably via a reduction in the intra-tumoral blood flow.

Certainly, many questions could not be answered within the scope of this study:

(1) The cellular mechanism behind the tumor growth phenotype of male NO-GCsmko (**Figure 9D**) was not yet resolved. This could be achieved by *in situ* analysis of the tumor vasculature in NO-GCctrl and NO-GCsmko mice. Immunostaining of endothelial cells and pericytes in tumors with subsequent detection via confocal (tissue sections) or light sheet microscopy (whole-mount samples) could depict the vascular network and uncover potential differences in the distribution or localization of the tumor pericytes. Furthermore, differences in the vascular integrity between NO-GCctrl and NO-GCsmko tumors could be visualized by intravenous injection of dyes like Evans blue-BSA or fluorescently labelled dextrans and leptins, respectively (R. Jain et al., 2021). In this context, it will be important to carefully compare tumors of male and female experimental animals to analyze the causes for the observed sex differences (**Figure 9C and D**).

(2) *In situ* cGMP imaging provided evidence that the NO-GC stimulator riociguat can modulate the NO-induced cGMP generation in tumor pericytes (**Figure 8C and D**). This raises the question whether NO-GC modulators also have an effect on the tumor vasculature *in vivo*. To investigate this, wildtype and NO-GCsmko mice could be treated with NO-GC modulators, and the tumor vasculature could be analyzed as described above. With regard to NO-GC activators specifically, it would make sense to first determine the presence of oxidative stress within B16 tumors, for example, by

quantification of oxidative stress biomarkers (reviewed by Ho et al., 2013). Since the working hypothesis is that NO-GC activation in tumor pericytes induces vascular normalization (**Figure 11**), it might be advantageous to combine NO-GC modulator treatment with a co-therapy like chemo- or immunotherapy.

(3) In the present study, SMA-CreERT2 activation by tamoxifen injection was performed *before and during* tumor growth (2.3.2) to cover all tumor pericytes, independent of their cellular identity before tumor cell injection. It would be interesting to determine whether these tumor pericytes originate from perivascular cells of existing blood vessels that migrate into the tumor, or transdifferentiate from a non-vascular cell population within the tumor. To distinguish between these two possible origins, tamoxifen injection could be restricted to *either before or during* tumor growth, and the destiny of individual tumor pericytes could be followed by using a designated fate-mapping reporter like the confetti mouse model (Livet et al., 2007; Snippert et al., 2010). Preliminary experiments in which tamoxifen was only injected *before* tumor cell injection indicated that at least part of the tumor pericytes originate from cells that already were SMA-positive (**Figure S8**).

(4) Finally, the present work has only assessed primary B16 tumors, although most melanoma patients die from metastatic disease rather than the primary melanoma (see also 1.3.2). Therefore, it would be intriguing to decipher the role of tumor pericytes in a mouse model of metastatic melanoma. In the fast-growing B16 model, the termination criteria generally are met before metastases reach the size required for analysis. To allow more time for metastatic progression, it would be possible to resect the primary tumor after the initial growth phase, as reviewed by Day et al. (2015).

In conclusion, novel pharmacological NO-GC modulators like BAY-543 and runcaciguat provide powerful tools to restore NO-GC/cGMP signaling under disease conditions involving NOS blockade, NO scavenging and oxidative stress, while their unique modes of action at the same time limit effects on healthy tissues (e.g., hypotension). The present study has provided evidence for the potency of these drugs in CKD and melanoma. The clinical implications, however, do not stop here: I am convinced that future research will identify more diseases where NO-GC modulators prove useful to restore disrupted NO-GC/cGMP signaling.

5 References

Addgene (2019). Cre-lox plasmids. Available from https://www.addgene.org/collections/cre-lox/ (accessed 21 June 2021)

Anand-Srivastava, M. B. (2005). Natriuretic peptide receptor-C signaling and regulation. *Peptides, 26*(6), 1044-1059. doi:10.1016/j.peptides.2004.09.023

Armulik, A., Abramsson, A., & Betsholtz, C. (2005). Endothelial/pericyte interactions. *Circ Res, 97*(6), 512-523. doi:10.1161/01.RES.0000182903.16652.d7

Arnold, W. P., Mittal, C. K., Katsuki, S., & Murad, F. (1977). Nitric oxide activates guanylate cyclase and increases guanosine 3':5'-cyclic monophosphate levels in various tissue preparations. *Proc Natl Acad Sci U S A, 74*(8), 3203-3207. doi:10.1073/pnas.74.8.3203

Arozarena, I., Sanchez-Laorden, B., Packer, L., Hidalgo-Carcedo, C., Hayward, R., Viros, A., … Marais, R. (2011). Oncogenic BRAF induces melanoma cell invasion by downregulating the cGMP-specific phosphodiesterase PDE5A. *Cancer Cell, 19*(1), 45-57. doi:10.1016/j.ccr.2010.10.029

Auso, E., Gomez-Vicente, V., & Esquiva, G. (2021). Visual side effects linked to sildenafil consumption: An update. *Biomedicines, 9*(3), 1-23. doi:10.3390/biomedicines9030291

Baillie, G. S., Tejeda, G. S., & Kelly, M. P. (2019). Therapeutic targeting of 3',5'-cyclic nucleotide phosphodiesterases: inhibition and beyond. *Nat Rev Drug Discov, 18*(10), 770-796. doi:10.1038/s41573-019-0033-4

Ben-David, U., Siranosian, B., Ha, G., Tang, H., Oren, Y., Hinohara, K., … Golub, T. R. (2018). Genetic and transcriptional evolution alters cancer cell line drug response. *Nature, 560*(7718), 325-330. doi:10.1038/s41586-018-0409-3

Benardeau, A., Kahnert, A., Schomber, T., Meyer, J., Pavkovic, M., Kretschmer, A., … Sandner, P. (2021). Runcaciguat, a novel soluble guanylate cyclase activator, shows renoprotection in hypertensive, diabetic, and metabolic preclinical models of chronic kidney disease. *Naunyn Schmiedebergs Arch Pharmacol, 394*(12), 2363-2379. doi:10.1007/s00210-021-02149-4

Bender, A. T., & Beavo, J. A. (2006). Cyclic nucleotide phosphodiesterases: molecular regulation to clinical use. *Pharmacol Rev, 58*(3), 488-520. doi:10.1124/pr.58.3.5

Blackwell, K. L., Haroon, Z. A., Shan, S., Saito, W., Broadwater, G., Greenberg, C. S., & Dewhirst, M. W. (2000). Tamoxifen inhibits angiogenesis in estrogen receptor-negative animal models. *Clin Cancer Res, 6*(11), 4359-4364.

Blum, K. M., Roby, L. C., Zbinden, J. C., Chang, Y. C., Mirhaidari, G. J. M., Reinhardt, J. W., … Breuer, C. K. (2021). Sex and Tamoxifen confound murine experimental studies in cardiovascular tissue engineering. *Sci Rep, 11*(1), 8037. doi:10.1038/s41598-021-87006-3

Boerrigter, G., Costello-Boerrigter, L. C., Cataliotti, A., Tsuruda, T., Harty, G. J., Lapp, H., … Burnett, J. C., Jr. (2003). Cardiorenal and humoral properties of a novel direct soluble guanylate cyclase stimulator BAY 41-2272 in experimental congestive heart failure. *Circulation, 107*(5), 686-689. doi:10.1161/01.cir.0000055737.15443.f8

Boustany-Kari, C. M., Harrison, P. C., Chen, H., Lincoln, K. A., Qian, H. S., Clifford, H., … Pullen, S. S. (2016). A soluble guanylate cyclase activator inhibits the progression of diabetic nephropathy in the ZSF1 rat. *J Pharmacol Exp Ther, 356*(3), 712-719. doi:10.1124/jpet.115.230706

Brands, M. W., & Freeman, R. H. (1988). Aldosterone and renin inhibition by physiological levels of atrial natriuretic factor. *Am J Physiol, 254*(6 Pt 2), R1011-1016. doi:10.1152/ajpregu.1988.254.6.R1011

Brash, J. T., Bolton, R. L., Rashbrook, V. S., Denti, L., Kubota, Y., & Ruhrberg, C. (2020). Tamoxifen-activated CreERT impairs retinal angiogenesis independently of gene deletion. *Circ Res, 127*(6), 849-850. doi:10.1161/CIRCRESAHA.120.317025

Breyer, M. D., & Susztak, K. (2016). Developing treatments for chronic kidney disease in the 21st century. *Semin Nephrol, 36*(6), 436-447. doi:10.1016/j.semnephrol.2016.08.001

Briasoulis, A., Al Dhaybi, O., & Bakris, G. L. (2018). SGLT2 inhibitors and mechanisms of hypertension. *Curr Cardiol Rep, 20*(1), 1. doi:10.1007/s11886-018-0943-5

Brown, C., Pan, X., & Hassid, A. (1999). Nitric oxide and C-type atrial natriuretic peptide stimulate primary aortic smooth muscle cell migration via a cGMP-dependent mechanism: relationship to microfilament dissociation and altered cell morphology. *Circ Res, 84*(6), 655-667. doi:10.1161/01.res.84.6.655

Browning, M. (2012). 1% SDS is the lysis buffer of choice for most Western Blots. Available from https://www.phosphosolutions.com/2353-2/ (accessed 22 June 2021)

Burnett, J. C., Jr., Granger, J. P., & Opgenorth, T. J. (1984). Effects of synthetic atrial natriuretic factor on renal function and renin release. *Am J Physiol, 247*(5 Pt 2), F863-866. doi:10.1152/ajprenal.1984.247.5.F863

Buys, E. S., Raher, M. J., Kirby, A., Shahid, M., Baron, D. M., Hayton, S. R., … Bloch, K. D. (2012). Genetic modifiers of hypertension in soluble guanylate cyclase alpha1-deficient mice. *J Clin Invest, 122*(6), 2316-2325. doi:10.1172/JCI60119

Buys, E. S., Sips, P., Vermeersch, P., Raher, M. J., Rogge, E., Ichinose, F., … Brouckaert, P. (2008). Gender-specific hypertension and responsiveness to nitric oxide in sGCalpha1 knockout mice. *Cardiovasc Res, 79*(1), 179-186. doi:10.1093/cvr/cvn068

Carretero-Gonzalez, A., Lora, D., Ghanem, I., Otero, I., Lopez, F., Castellano, D., & de Velasco, G. (2019). Comparative safety analysis of immunotherapy combined with chemotherapy versus monotherapy in solid tumors: a meta-analysis of randomized clinical trials. *Oncotarget, 10*(35), 3294-3301. doi:10.18632/oncotarget.26908

Castro, L. R., Verde, I., Cooper, D. M., & Fischmeister, R. (2006). Cyclic guanosine monophosphate compartmentation in rat cardiac myocytes. *Circulation, 113*(18), 2221-2228. doi:10.1161/CIRCULATIONAHA.105.599241

Catalano, S., Panza, S., Augimeri, G., Giordano, C., Malivindi, R., Gelsomino, L., … Barone, I. (2019). Phosphodiesterase 5 (PDE5) is highly expressed in cancer-associated fibroblasts and enhances breast tumor progression. *Cancers (Basel), 11*(11), 1740. doi:10.3390/cancers11111740

Chen, Y., & Burnett, J. C. (2018). Particulate guanylyl cyclase A/cGMP signaling pathway in the kidney: Physiologic and therapeutic indications. *Int J Mol Sci, 19*(4), 1006. doi:10.3390/ijms19041006

Cignarella, A., Fadini, G. P., Bolego, C., Trevisi, L., Boscaro, C., Sanga, V., … Barton, M. (2021). Clinical efficacy and safety of angiogenesis inhibitors: Sex differences and current challenges. *Cardiovasc Res, 0*, 1-16. doi:10.1093/cvr/cvab096

Clavell, A. L., Stingo, A. J., Wei, C. M., Heublein, D. M., & Burnett, J. C., Jr. (1993). C-type natriuretic peptide: a selective cardiovascular peptide. *Am J Physiol, 264*(2 Pt 2), R290-295. doi:10.1152/ajpregu.1993.264.2.R290

Coppolino, G., Leonardi, G., Andreucci, M., & Bolignano, D. (2018). Oxidative stress and kidney function: a brief update. *Curr Pharm Des, 24*(40), 4794-4799. doi:10.2174/1381612825666190112165206

Cormier, J. N., Abati, A., Fetsch, P., Hijazi, Y. M., Rosenberg, S. A., Marincola, F. M., & Topalian, S. L. (1998). Comparative analysis of the in vivo expression of tyrosinase, MART-1/Melan-A, and gp100 in metastatic melanoma lesions: implications for immunotherapy. *J Immunother, 21*(1), 27-31. doi:10.1097/00002371-199801000-00003

Cuervo, H., Pereira, B., Nadeem, T., Lin, M., Lee, F., Kitajewski, J., & Lin, C. S. (2017). PDGFRbeta-P2A-CreER(T2) mice: a genetic tool to target pericytes in angiogenesis. *Angiogenesis, 20*(4), 655-662. doi:10.1007/s10456-017-9570-9

Czirbesz, K., Gorka, E., Balatoni, T., Panczel, G., Melegh, K., Kovacs, P., … Liszkay, G. (2019). Efficacy of vemurafenib treatment in 43 metastatic melanoma patients with BRAF mutation. Single-institute retrospective analysis, early real-life survival data. *Pathol Oncol Res, 25*(1), 45-50. doi:10.1007/s12253-017-0324-1

Dakup, P. P., Porter, K. I., Little, A. A., Zhang, H., & Gaddameedhi, S. (2020). Sex differences in the association between tumor growth and T cell response in a melanoma mouse model. *Cancer Immunol Immunother, 69*(10), 2157-2162. doi:10.1007/s00262-020-02643-3

Dankort, D., Curley, D. P., Cartlidge, R. A., Nelson, B., Karnezis, A. N., Damsky, W. E., Jr., … Bosenberg, M. (2009). Braf(V600E) cooperates with Pten loss to induce metastatic melanoma. *Nat Genet, 41*(5), 544-552. doi:10.1038/ng.356

Davar, D., Wang, H., Chauvin, J. M., Pagliano, O., Fourcade, J. J., Ka, M., … Zarour, H. M. (2018). Phase Ib/II study of pembrolizumab and pegylated-interferon alfa-2b in advanced melanoma. *J Clin Oncol, 36*(35), JCO1800632. doi:10.1200/JCO.18.00632

Day, C. P., Merlino, G., & Van Dyke, T. (2015). Preclinical mouse cancer models: a maze of opportunities and challenges. *Cell, 163*(1), 39-53. doi:10.1016/j.cell.2015.08.068

De Bock, K., Cauwenberghs, S., & Carmeliet, P. (2011). Vessel abnormalization: another hallmark of cancer? Molecular mechanisms and therapeutic implications. *Curr Opin Genet Dev, 21*(1), 73-79. doi:10.1016/j.gde.2010.10.008

Derbyshire, E. R., & Marletta, M. A. (2012). Structure and regulation of soluble guanylate cyclase. *Annu Rev Biochem, 81*, 533-559. doi:10.1146/annurev-biochem-050410-100030

Dhayade, S., Kaesler, S., Sinnberg, T., Dobrowinski, H., Peters, S., Naumann, U., … Feil, R. (2016). Sildenafil potentiates a cGMP-dependent pathway to promote melanoma growth. *Cell Rep, 14*(11), 2599-2610. doi:10.1016/j.celrep.2016.02.028

Dordea, A. C., Vandenwijngaert, S., Garcia, V., Tainsh, R. E., Nathan, D. I., Allen, K., … Buys, E. S. (2016). Androgen-sensitive hypertension associated with soluble guanylate cyclase-alpha1 deficiency is mediated by 20-HETE. *Am J Physiol Heart Circ Physiol, 310*(11), H1790-1800. doi:10.1152/ajpheart.00877.2015

Elwood, J. M., & Gallagher, R. P. (1998). Body site distribution of cutaneous malignant melanoma in relationship to patterns of sun exposure. *Int J Cancer, 78*(3), 276-280. doi:10.1002/(SICI)1097-0215(19981029)78:3<276::AID-IJC2>3.0.CO;2-S

Emdin, C. A., Khera, A. V., Klarin, D., Natarajan, P., Zekavat, S. M., Nomura, A., … Kathiresan, S. (2018). Phenotypic consequences of a genetic predisposition to enhanced nitric oxide signaling. *Circulation, 137*(3), 222-232. doi:10.1161/CIRCULATIONAHA.117.028021

Feil, R. (2007). Conditional somatic mutagenesis in the mouse using site-specific recombinases. In R. Feil & D. Metzger (Eds.), *Conditional mutagenesis: An approach to disease models*, (pp. 3-28). Berlin, Heidelberg: Springer Berlin Heidelberg.

Feil, R., & Kemp-Harper, B. (2006). cGMP signalling: from bench to bedside. Conference on cGMP generators, effectors and therapeutic implications. *EMBO Rep, 7*(2), 149-153. doi:10.1038/sj.embor.7400627

Feil, R., Lehners, M., Stehle, D., & Feil, S. (2021). Visualising and understanding cGMP signals in the cardiovascular system. *Br J Pharmacol, 10.1111/bph.15500*, 1-19. doi:10.1111/bph.15500

Feil, R., Lohmann, S. M., de Jonge, H., Walter, U., & Hofmann, F. (2003). Cyclic GMP-dependent protein kinases and the cardiovascular system: insights from genetically modified mice. *Circ Res, 93*(10), 907-916. doi:10.1161/01.RES.0000100390.68771.CC

Feil, S., Krauss, J., Thunemann, M., & Feil, R. (2014). Genetic inducible fate mapping in adult mice using tamoxifen-dependent Cre recombinases. *Methods Mol Biol, 1194*, 113-139. doi:10.1007/978-1-4939-1215-5_6

Feil, S., Valtcheva, N., & Feil, R. (2009). Inducible Cre mice. *Methods Mol Biol, 530*, 343-363. doi:10.1007/978-1-59745-471-1_18

Fiaschi, T., & Chiarugi, P. (2012). Oxidative stress, tumor microenvironment, and metabolic reprogramming: a diabolic liaison. *Int J Cell Biol, 2012*, 762825. doi:10.1155/2012/762825

Fidler, I. J. (1973). Selection of successive tumour lines for metastasis. *Nat New Biol, 242*(118), 148-149. doi:10.1038/newbio242148a0

Fidler, I. J. (1975). Biological behavior of malignant melanoma cells correlated to their survival in vivo. *Cancer Res, 35*(1), 218-224.

Foo, S. S., Turner, C. J., Adams, S., Compagni, A., Aubyn, D., Kogata, N., … Adams, R. H. (2006). Ephrin-B2 controls cell motility and adhesion during blood-vessel-wall assembly. *Cell, 124*(1), 161-173. doi:10.1016/j.cell.2005.10.034

Forstermann, U., & Kleinert, H. (1995). Nitric oxide synthase: expression and expressional control of the three isoforms. *Naunyn Schmiedebergs Arch Pharmacol, 352*(4), 351-364. doi:10.1007/BF00172772

Francis, S. H., & Corbin, J. D. (2005). Phosphodiesterase-5 inhibition: the molecular biology of erectile function and dysfunction. *Urol Clin North Am, 32*(4), 419-429, vi. doi:10.1016/j.ucl.2005.08.001

Frees, A., Assersen, K. B., Jensen, M., Hansen, P. B. L., Vanhoutte, P. M., Madsen, K., … Jensen, B. L. (2021). Natriuretic peptides relax human intrarenal arteries through natriuretic peptide receptor type-A recapitulated by soluble guanylyl cyclase agonists. *Acta Physiol (Oxf), 231*(3), e13565. doi:10.1111/apha.13565

Friebe, A., & Koesling, D. (2009). The function of NO-sensitive guanylyl cyclase: what we can learn from genetic mouse models. *Nitric Oxide, 21*(3-4), 149-156. doi:10.1016/j.niox.2009.07.004

Friebe, A., Mergia, E., Dangel, O., Lange, A., & Koesling, D. (2007). Fatal gastrointestinal obstruction and hypertension in mice lacking nitric oxide-sensitive guanylyl cyclase. *Proc Natl Acad Sci U S A, 104*(18), 7699-7704. doi:10.1073/pnas.0609778104

Friebe, A., Voussen, B., & Groneberg, D. (2018). NO-GC in cells 'off the beaten track'. *Nitric Oxide, 77*, 12-18. doi:10.1016/j.niox.2018.03.020

Furchgott, R. F., & Zawadzki, J. V. (1980). The obligatory role of endothelial cells in the relaxation of arterial smooth muscle by acetylcholine. *Nature, 288*(5789), 373-376. doi:10.1038/288373a0

Gagliardi, A., & Collins, D. C. (1993). Inhibition of angiogenesis by antiestrogens. *Cancer Res, 53*(3), 533-535.

Garthwaite, J., Southam, E., Boulton, C. L., Nielsen, E. B., Schmidt, K., & Mayer, B. (1995). Potent and selective inhibition of nitric oxide-sensitive guanylyl cyclase by 1H-[1,2,4]oxadiazolo[4,3-a]quinoxalin-1-one. *Mol Pharmacol, 48*(2), 184-188.

Gary-Bobo, G., Parlakian, A., Escoubet, B., Franco, C. A., Clement, S., Bruneval, P., … Mericskay, M. (2008). Mosaic inactivation of the serum response factor gene in the myocardium induces focal lesions and heart failure. *Eur J Heart Fail, 10*(7), 635-645. doi:10.1016/j.ejheart.2008.04.014

Goel, S., Duda, D. G., Xu, L., Munn, L. L., Boucher, Y., Fukumura, D., & Jain, R. K. (2011). Normalization of the vasculature for treatment of cancer and other diseases. *Physiol Rev, 91*(3), 1071-1121. doi:10.1152/physrev.00038.2010

Gori, M., Januzzi, J. L., D'Elia, E., Lorini, F. L., & Senni, M. (2021). Rationale for and practical use of sacubitril/valsartan in the patient's journey with heart failure and reduced ejection fraction. *Card Fail Rev, 7*, e06. doi:10.15420/cfr.2020.25

Gotz, K. R., Sprenger, J. U., Perera, R. K., Steinbrecher, J. H., Lehnart, S. E., Kuhn, M., … Nikolaev, V. O. (2014). Transgenic mice for real-time visualization of cGMP in intact adult cardiomyocytes. *Circ Res, 114*(8), 1235-1245. doi:10.1161/CIRCRESAHA.114.302437

Gould, S. E., Junttila, M. R., & de Sauvage, F. J. (2015). Translational value of mouse models in oncology drug development. *Nat Med, 21*(5), 431-439. doi:10.1038/nm.3853

Green, D. F., Duruibe, V. A., Blyden, G., Laskey, R. E., & Bourgoignie, J. J. (1994). Uptake of atrial natriuretic peptide and production of cGMP in cultured human glomerular endothelial cells. *J Am Soc Nephrol, 5*(4), 1091-1098. doi:10.1681/ASN.V541091

Groneberg, D., Konig, P., Wirth, A., Offermanns, S., Koesling, D., & Friebe, A. (2010). Smooth muscle-specific deletion of nitric oxide-sensitive guanylyl cyclase is sufficient to induce hypertension in mice. *Circulation, 121*(3), 401-409. doi:10.1161/CIRCULATIONAHA.109.890962

Hahn, M. G., Lampe, T., El Sheikh, S., Griebenow, N., Woltering, E., Schlemmer, K. H., … Stasch, J. P. (2021). Discovery of the soluble guanylate cyclase activator runcaciguat (BAY 1101042). *J Med Chem, 64*(9), 5323-5344. doi:10.1021/acs.jmedchem.0c02154

Hall, K. C., Bernier, S. G., Jacobson, S., Liu, G., Zhang, P. Y., Sarno, R., … Masferrer, J. L. (2019). sGC stimulator praliciguat suppresses stellate cell fibrotic transformation and inhibits fibrosis and inflammation in models of NASH. *Proc Natl Acad Sci U S A, 116*(22), 11057-11062. doi:10.1073/pnas.1821045116

Halpern, A. C., Marghoob, A. A., & Reiter, O. (2021). Melanoma warning signs. Available from https://www.skincancer.org/skin-cancer-information/melanoma/melanoma-warning-signs-and-images/ (accessed 21 June 2021)

Hammer, C. (1998). Physiological obstacles after xenotransplantation. *Ann N Y Acad Sci, 862*, 19-27. doi:10.1111/j.1749-6632.1998.tb09113.x

Hanahan, D., & Weinberg, R. A. (2000). The hallmarks of cancer. *Cell, 100*(1), 57-70. doi:10.1016/s0092-8674(00)81683-9

He, X. L., Dukkipati, A., & Garcia, K. C. (2006). Structural determinants of natriuretic peptide receptor specificity and degeneracy. *J Mol Biol, 361*(4), 698-714. doi:10.1016/j.jmb.2006.06.060

Hess, D. T., Matsumoto, A., Kim, S. O., Marshall, H. E., & Stamler, J. S. (2005). Protein S-nitrosylation: purview and parameters. *Nat Rev Mol Cell Biol, 6*(2), 150-166. doi:10.1038/nrm1569

Hirata, E., Girotti, M. R., Viros, A., Hooper, S., Spencer-Dene, B., Matsuda, M., … Sahai, E. (2015). Intravital imaging reveals how BRAF inhibition generates drug-tolerant microenvironments with high integrin beta1/FAK signaling. *Cancer Cell, 27*(4), 574-588. doi:10.1016/j.ccell.2015.03.008

Ho, E., Karimi Galougahi, K., Liu, C. C., Bhindi, R., & Figtree, G. A. (2013). Biological markers of oxidative stress: Applications to cardiovascular research and practice. *Redox Biol, 1*, 483-491. doi:10.1016/j.redox.2013.07.006

Hodi, F. S., O'Day, S. J., McDermott, D. F., Weber, R. W., Sosman, J. A., Haanen, J. B., … Urba, W. J. (2010). Improved survival with ipilimumab in patients with metastatic melanoma. *N Engl J Med, 363*(8), 711-723. doi:10.1056/NEJMoa1003466

Hodis, E., Watson, I. R., Kryukov, G. V., Arold, S. T., Imielinski, M., Theurillat, J. P., … Chin, L. (2012). A landscape of driver mutations in melanoma. *Cell, 150*(2), 251-263. doi:10.1016/j.cell.2012.06.024

Hofmann, F. (2020). The cGMP system: components and function. *Biol Chem, 401*(4), 447-469. doi:10.1515/hsz-2019-0386

Holtwick, R., Gotthardt, M., Skryabin, B., Steinmetz, M., Potthast, R., Zetsche, B., … Kuhn, M. (2002). Smooth muscle-selective deletion of guanylyl cyclase-A prevents the acute but not chronic effects of ANP on blood pressure. *Proc Natl Acad Sci U S A, 99*(10), 7142-7147. doi:10.1073/pnas.102650499

Horst, B. G., Yokom, A. L., Rosenberg, D. J., Morris, K. L., Hammel, M., Hurley, J. H., & Marletta, M. A. (2019). Allosteric activation of the nitric oxide receptor soluble guanylate cyclase mapped by cryo-electron microscopy. *Elife, 8*, 1-25. doi:10.7554/eLife.50634

Hsu, S. M., Raine, L., & Fanger, H. (1981). Use of avidin-biotin-peroxidase complex (ABC) in immunoperoxidase techniques: a comparison between ABC and unlabeled antibody (PAP) procedures. *J Histochem Cytochem, 29*(4), 577-580. doi:10.1177/29.4.6166661

Huang, C. L., Ives, H. E., & Cogan, M. G. (1986). In vivo evidence that cGMP is the second messenger for atrial natriuretic factor. *Proc Natl Acad Sci U S A, 83*(20), 8015-8018. doi:10.1073/pnas.83.20.8015

Huang, Y., Yuan, J., Righi, E., Kamoun, W. S., Ancukiewicz, M., Nezivar, J., … Poznansky, M. C. (2012). Vascular normalizing doses of antiangiogenic treatment reprogram the immunosuppressive tumor microenvironment and enhance immunotherapy. *Proc Natl Acad Sci U S A, 109*(43), 17561-17566. doi:10.1073/pnas.1215397109

Huie, R. E., & Padmaja, S. (1993). The reaction of no with superoxide. *Free Radic Res Commun, 18*(4), 195-199. doi:10.3109/10715769309145868

Ignarro, L. J., Buga, G. M., Wood, K. S., Byrns, R. E., & Chaudhuri, G. (1987). Endothelium-derived relaxing factor produced and released from artery and vein is nitric oxide. *Proc Natl Acad Sci U S A, 84*(24), 9265-9269. doi:10.1073/pnas.84.24.9265

Ito, A., Kondo, S., Tada, K., & Kitano, S. (2015). Clinical development of immune checkpoint inhibitors. *Biomed Res Int, 2015*, 605478. doi:10.1155/2015/605478

Ivanova, K., Das, P. K., van den Wijngaard, R. M., Lenz, W., Klockenbring, T., Malcharzyk, V., … Gerzer, R. (2001). Differential expression of functional guanylyl cyclases in melanocytes: absence of nitric-oxide-sensitive isoform in metastatic cells. *J Invest Dermatol, 116*(3), 409-416. doi:10.1046/j.1523-1747.2001.01255.x

Jain, R., Tikoo, S., On, K., Martinez, B., Dervish, S., Cavanagh, L. L., & Weninger, W. (2021). Visualizing murine breast and melanoma tumor microenvironment using intravital multiphoton microscopy. *STAR Protoc, 2*(3), 100722. doi:10.1016/j.xpro.2021.100722

Jain, R. K. (2005). Normalization of tumor vasculature: an emerging concept in antiangiogenic therapy. *Science, 307*(5706), 58-62. doi:10.1126/science.1104819

Jia, T., Olauson, H., Lindberg, K., Amin, R., Edvardsson, K., Lindholm, B., … Larsson, T. E. (2013). A novel model of adenine-induced tubulointerstitial nephropathy in mice. *BMC Nephrol, 14*, 116. doi:10.1186/1471-2369-14-116

Johnson, C. A., Levey, A. S., Coresh, J., Levin, A., Lau, J., & Eknoyan, G. (2004a). Clinical practice guidelines for chronic kidney disease in adults: Part I. Definition, disease stages, evaluation, treatment, and risk factors. *Am Fam Physician, 70*(5), 869-876.

Johnson, C. A., Levey, A. S., Coresh, J., Levin, A., Lau, J., & Eknoyan, G. (2004b). Clinical practice guidelines for chronic kidney disease in adults: Part II. Glomerular filtration rate, proteinuria, and other markers. *Am Fam Physician, 70*(6), 1091-1097.

Kahn, B. M., Lucas, A., Alur, R. G., Wengyn, M. D., Schwartz, G. W., Li, J., … Stanger, B. Z. (2021). The vascular landscape of human cancer. *J Clin Invest, 131*(2)doi:10.1172/JCI136655

Kang, Y., Liu, R., Wu, J. X., & Chen, L. (2019). Structural insights into the mechanism of human soluble guanylate cyclase. *Nature, 574*(7777), 206-210. doi:10.1038/s41586-019-1584-6

Karachaliou, N., Gonzalez-Cao, M., Sosa, A., Berenguer, J., Bracht, J. W. P., Ito, M., & Rosell, R. (2017). The combination of checkpoint immunotherapy and targeted therapy in cancer. *Ann Transl Med, 5*(19), 388. doi:10.21037/atm.2017.06.47

Kashiwagi, S., Izumi, Y., Gohongi, T., Demou, Z. N., Xu, L., Huang, P. L., … Fukumura, D. (2005). NO mediates mural cell recruitment and vessel morphogenesis in murine melanomas and tissue-engineered blood vessels. *J Clin Invest, 115*(7), 1816-1827. doi:10.1172/JCI24015

Kashiwagi, S., Tsukada, K., Xu, L., Miyazaki, J., Kozin, S. V., Tyrrell, J. A., … Fukumura, D. (2008). Perivascular nitric oxide gradients normalize tumor vasculature. *Nat Med, 14*(3), 255-257. doi:10.1038/nm1730

Kisanuki, Y. Y., Hammer, R. E., Miyazaki, J., Williams, S. C., Richardson, J. A., & Yanagisawa, M. (2001). Tie2-Cre transgenic mice: a new model for endothelial cell-lineage analysis in vivo. *Dev Biol, 230*(2), 230-242. doi:10.1006/dbio.2000.0106

Knorr, A., Hirth-Dietrich, C., Alonso-Alija, C., Harter, M., Hahn, M., Keim, Y., … Stasch, J. P. (2008). Nitric oxide-independent activation of soluble guanylate cyclase by BAY 60-2770 in experimental liver fibrosis. *Arzneimittelforschung, 58*(2), 71-80. doi:10.1055/s-0031-1296471

Ko, E. C., & Formenti, S. C. (2018). Radiotherapy and checkpoint inhibitors: a winning new combination? *Ther Adv Med Oncol, 10*, 1758835918768240. doi:10.1177/1758835918768240

Kolarsick, P. A. J., Kolarsick, M. A., & Goodwin, C. (2011). Anatomy and physiology of the skin. *J Dermatol Nurses Assoc, 3*(4), 203-213. doi:10.1097/JDN.0b013e3182274a98

Kramer, M. S., Feil, R., & Schmidt, H. (2021). Analysis of gene expression using lacZ reporter mouse lines. *Methods Mol Biol, 2224*, 29-45. doi:10.1007/978-1-0716-1008-4_2

Krishnan, S. M., Kraehling, J. R., Eitner, F., Benardeau, A., & Sandner, P. (2018). The impact of the nitric oxide (NO)/soluble guanylyl cyclase (sGC) signaling cascade on kidney health and disease: a preclinical perspective. *Int J Mol Sci, 19*(6), 1712. doi:10.3390/ijms19061712

Ku, E., Lee, B. J., Wei, J., & Weir, M. R. (2019). Hypertension in CKD: Core Curriculum 2019. *Am J Kidney Dis, 74*(1), 120-131. doi:10.1053/j.ajkd.2018.12.044

Kuhn, M. (2003). Structure, regulation, and function of mammalian membrane guanylyl cyclase receptors, with a focus on guanylyl cyclase-A. *Circ Res, 93*(8), 700-709. doi:10.1161/01.RES.0000094745.28948.4D

Kuhn, M. (2012). Endothelial actions of atrial and B-type natriuretic peptides. *Br J Pharmacol, 166*(2), 522-531. doi:10.1111/j.1476-5381.2012.01827.x

Kuhn, M. (2016). Molecular physiology of membrane guanylyl cyclase receptors. *Physiol Rev, 96*(2), 751-804. doi:10.1152/physrev.00022.2015

Kumar, P., Gogulamudi, V. R., Periasamy, R., Raghavaraju, G., Subramanian, U., & Pandey, K. N. (2017). Inhibition of HDAC enhances STAT acetylation, blocks NF-kappaB, and suppresses the renal inflammation and fibrosis in Npr1 haplotype male mice. *Am J Physiol Renal Physiol, 313*(3), F781-F795. doi:10.1152/ajprenal.00166.2017

Kurtz, A., Gotz, K. H., Hamann, M., & Wagner, C. (1998). Stimulation of renin secretion by nitric oxide is mediated by phosphodiesterase 3. *Proc Natl Acad Sci U S A, 95*(8), 4743-4747. doi:10.1073/pnas.95.8.4743

Laemmli, U. K. (1970). Cleavage of structural proteins during the assembly of the head of bacteriophage T4. *Nature, 227*(5259), 680-685. doi:10.1038/227680a0

LeBleu, V. S., Taduri, G., O'Connell, J., Teng, Y., Cooke, V. G., Woda, C., … Kalluri, R. (2013). Origin and function of myofibroblasts in kidney fibrosis. *Nat Med, 19*(8), 1047-1053. doi:10.1038/nm.3218

Lees, M. B., & Paxman, S. (1972). Modification of the Lowry procedure for the analysis of proteolipid protein. *Anal Biochem, 47*(1), 184-192. doi:10.1016/0003-2697(72)90291-6

Li, W., Mital, S., Ojaimi, C., Csiszar, A., Kaley, G., & Hintze, T. H. (2004). Premature death and age-related cardiac dysfunction in male eNOS-knockout mice. *J Mol Cell Cardiol, 37*(3), 671-680. doi:10.1016/j.yjmcc.2004.05.005

Li, W. Q., Qureshi, A. A., Robinson, K. C., & Han, J. (2014). Sildenafil use and increased risk of incident melanoma in US men: a prospective cohort study. *JAMA Intern Med, 174*(6), 964-970. doi:10.1001/jamainternmed.2014.594

Li, Y., Choi, P. S., Casey, S. C., & Felsher, D. W. (2014). Activation of Cre recombinase alone can induce complete tumor regression. *PLoS One, 9*(9), e107589. doi:10.1371/journal.pone.0107589

Lin, Y. H., Huang, Y. Y., Hsieh, S. H., Sun, J. H., Chen, S. T., & Lin, C. H. (2019). Renal and glucose-lowering effects of empagliflozin and dapagliflozin in different chronic kidney disease stages. *Front Endocrinol (Lausanne), 10*, 820. doi:10.3389/fendo.2019.00820

Lincoln, T. M., Dey, N., & Sellak, H. (2001). Invited review: cGMP-dependent protein kinase signaling mechanisms in smooth muscle: from the regulation of tone to gene expression. *J Appl Physiol (1985), 91*(3), 1421-1430. doi:10.1152/jappl.2001.91.3.1421

Liu, R., Kang, Y., & Chen, L. (2021). Activation mechanism of human soluble guanylate cyclase by stimulators and activators. *Nat Commun, 12*(1), 5492. doi:10.1038/s41467-021-25617-0

Livet, J., Weissman, T. A., Kang, H., Draft, R. W., Lu, J., Bennis, R. A., … Lichtman, J. W. (2007). Transgenic strategies for combinatorial expression of fluorescent proteins in the nervous system. *Nature, 450*(7166), 56-62. doi:10.1038/nature06293

Loeb, S., Ventimiglia, E., Salonia, A., Folkvaljon, Y., & Stattin, P. (2017). Meta-analysis of the association between phosphodiesterase inhibitors (PDE5Is) and risk of melanoma. *J Natl Cancer Inst, 109*(8), djx086. doi:10.1093/jnci/djx086

Lopez, M. J., Wong, S. K., Kishimoto, I., Dubois, S., Mach, V., Friesen, J., … Beuve, A. (1995). Salt-resistant hypertension in mice lacking the guanylyl cyclase-A receptor for atrial natriuretic peptide. *Nature, 378*(6552), 65-68. doi:10.1038/378065a0

Lowry, O. H., Rosebrough, N. J., Farr, A. L., & Randall, R. J. (1951). Protein measurement with the Folin phenol reagent. *J Biol Chem, 193*(1), 265-275.

Madisen, L., Zwingman, T. A., Sunkin, S. M., Oh, S. W., Zariwala, H. A., Gu, H., … Zeng, H. (2010). A robust and high-throughput Cre reporting and characterization system for the whole mouse brain. *Nat Neurosci, 13*(1), 133-140. doi:10.1038/nn.2467

Marsh, N., & Marsh, A. (2000). A short history of nitroglycerine and nitric oxide in pharmacology and physiology. *Clin Exp Pharmacol Physiol, 27*(4), 313-319. doi:10.1046/j.1440-1681.2000.03240.x

Matulef, K., & Zagotta, W. N. (2003). Cyclic nucleotide-gated ion channels. *Annu Rev Cell Dev Biol, 19*, 23-44. doi:10.1146/annurev.cellbio.19.110701.154854

McMurray, J. J., Packer, M., Desai, A. S., Gong, J., Lefkowitz, M. P., Rizkala, A. R., … PARADIGM-HF Investigators and Committees. (2014). Angiotensin-neprilysin inhibition versus enalapril in heart failure. *N Engl J Med, 371*(11), 993-1004. doi:10.1056/NEJMoa1409077

Meyer, C., Sevko, A., Ramacher, M., Bazhin, A. V., Falk, C. S., Osen, W., … Umansky, V. (2011). Chronic inflammation promotes myeloid-derived suppressor cell activation blocking antitumor immunity in transgenic mouse melanoma model. *Proc Natl Acad Sci U S A, 108*(41), 17111-17116. doi:10.1073/pnas.1108121108

Miller, A. A., Hislop, A. A., Vallance, P. J., & Haworth, S. G. (2005). Deletion of the eNOS gene has a greater impact on the pulmonary circulation of male than female mice. *Am J Physiol Lung Cell Mol Physiol, 289*(2), L299-306. doi:10.1152/ajplung.00022.2005

Mintz, J., Vedenko, A., Rosete, O., Shah, K., Goldstein, G., Hare, J. M., … Arora, H. (2021). Current advances of nitric oxide in cancer and anticancer therapeutics. *Vaccines (Basel), 9*(2)doi:10.3390/vaccines9020094

Murrell, W. (1879). Nitro-glycerin as a remedy for angina pectoris. *The Lancet, 113*(2890), 80-81. doi:10.1016/S0140-6736(02)46032-1

Muskiet, M. H. A., Heerspink, H. J. L., & van Raalte, D. H. (2017). SGLT2 inhibition: a new era in renoprotective medicine? *Lancet Diabetes Endocrinol, 5*(8), 569-571. doi:10.1016/S2213-8587(17)30222-X

Niino, Y., Hotta, K., & Oka, K. (2009). Simultaneous live cell imaging using dual FRET sensors with a single excitation light. *PLoS One, 4*(6), e6036. doi:10.1371/journal.pone.0006036

Opgenorth, T. J., Burnett, J. C., Jr., Granger, J. P., & Scriven, T. A. (1986). Effects of atrial natriuretic peptide on renin secretion in nonfiltering kidney. *Am J Physiol, 250*(5 Pt 2), F798-801. doi:10.1152/ajprenal.1986.250.5.F798

Overwijk, W. W., & Restifo, N. P. (2001). B16 as a mouse model for human melanoma. *Curr Protoc Immunol, Chapter 20*, Unit 20 21. doi:10.1002/0471142735.im2001s39

Parola, M., & Robino, G. (2001). Oxidative stress-related molecules and liver fibrosis. *J Hepatol, 35*(2), 297-306. doi:10.1016/s0168-8278(01)00142-8

Peterson, G. L. (1977). A simplification of the protein assay method of Lowry et al. which is more generally applicable. *Anal Biochem, 83*(2), 346-356. doi:10.1016/0003-2697(77)90043-4

Piggott, L. A., Hassell, K. A., Berkova, Z., Morris, A. P., Silberbach, M., & Rich, T. C. (2006). Natriuretic peptides and nitric oxide stimulate cGMP synthesis in different cellular compartments. *J Gen Physiol, 128*(1), 3-14. doi:10.1085/jgp.200509403

Polson, J. B., & Strada, S. J. (1996). Cyclic nucleotide phosphodiesterases and vascular smooth muscle. *Annu Rev Pharmacol Toxicol, 36*, 403-427. doi:10.1146/annurev.pa.36.040196.002155

Potter, L. R. (2011a). Guanylyl cyclase structure, function and regulation. *Cell Signal, 23*(12), 1921-1926. doi:10.1016/j.cellsig.2011.09.001

Potter, L. R. (2011b). Natriuretic peptide metabolism, clearance and degradation. *FEBS J, 278*(11), 1808-1817. doi:10.1111/j.1742-4658.2011.08082.x

Rensen, S. S., Doevendans, P. A., & van Eys, G. J. (2007). Regulation and characteristics of vascular smooth muscle cell phenotypic diversity. *Neth Heart J, 15*(3), 100-108. doi:10.1007/BF03085963

Ritchie, H., & Roser, M. (2018). Causes of death. Available from https://ourworldindata.org/causes-of-death#what-do-people-die-from (accessed 03 January 2022)

Robert, C., Thomas, L., Bondarenko, I., O'Day, S., Weber, J., Garbe, C., … Wolchok, J. D. (2011). Ipilimumab plus dacarbazine for previously untreated metastatic melanoma. *N Engl J Med, 364*(26), 2517-2526. doi:10.1056/NEJMoa1104621

Roche Pharma AG (2009). Avastin : EPAR - Product information. Available from https://www.ema.europa.eu/en/documents/product-information/avastin-epar-product-information_en.pdf (accessed 22 June 2021)

Roche Pharma AG (2012). Zelboraf : EPAR - Product information. Available from https://www.ema.europa.eu/en/documents/product-information/zelboraf-epar-product-information_en.pdf (accessed 21 June 2021)

Romero-Graillet, C., Aberdam, E., Biagoli, N., Massabni, W., Ortonne, J. P., & Ballotti, R. (1996). Ultraviolet B radiation acts through the nitric oxide and cGMP signal transduction pathway to stimulate melanogenesis in human melanocytes. *J Biol Chem, 271*(45), 28052-28056. doi:10.1074/jbc.271.45.28052

Rothermund, L., Friebe, A., Paul, M., Koesling, D., & Kreutz, R. (2000). Acute blood pressure effects of YC-1-induced activation of soluble guanylyl cyclase in normotensive and hypertensive rats. *Br J Pharmacol, 130*(2), 205-208. doi:10.1038/sj.bjp.0703320

Rueden, C. T., Schindelin, J., Hiner, M. C., DeZonia, B. E., Walter, A. E., Arena, E. T., & Eliceiri, K. W. (2017). ImageJ2: ImageJ for the next generation of scientific image data. *BMC Bioinformatics, 18*(1), 529. doi:10.1186/s12859-017-1934-z

Rühle, A., Elgert, C., Hahn, M. G., Sandner, P., & Behrends, S. (2020). Tyrosine 135 of the beta1 subunit as binding site of BAY-543: Importance of the Y-x-S-x-R motif for binding and activation by sGC activator drugs. *Eur J Pharmacol, 881*, 173203. doi:10.1016/j.ejphar.2020.173203

Russwurm, M., Mullershausen, F., Friebe, A., Jager, R., Russwurm, C., & Koesling, D. (2007). Design of fluorescence resonance energy transfer (FRET)-based cGMP indicators: a systematic approach. *Biochem J, 407*(1), 69-77. doi:10.1042/BJ20070348

Sabrane, K., Kruse, M. N., Fabritz, L., Zetsche, B., Mitko, D., Skryabin, B. V., … Kuhn, M. (2005). Vascular endothelium is critically involved in the hypotensive and hypovolemic actions of atrial natriuretic peptide. *J Clin Invest, 115*(6), 1666-1674. doi:10.1172/JCI23360

Samarghandian, S., Azimi-Nezhad, M., Farkhondeh, T., & Samini, F. (2017). Anti-oxidative effects of curcumin on immobilization-induced oxidative stress in rat brain, liver and kidney. *Biomed Pharmacother, 87*, 223-229. doi:10.1016/j.biopha.2016.12.105

Sandner, P. (2018). From molecules to patients: exploring the therapeutic role of soluble guanylate cyclase stimulators. *Biol Chem, 399*(7), 679-690. doi:10.1515/hsz-2018-0155

Sandner, P., Zimmer, D. P., Milne, G. T., Follmann, M., Hobbs, A., & Stasch, J. P. (2021). Soluble guanylate cyclase stimulators and activators. *Handb Exp Pharmacol, 264*, 355-394. doi:10.1007/164_2018_197

Savarirayan, R., Irving, M., Bacino, C. A., Bostwick, B., Charrow, J., Cormier-Daire, V., … Hoover-Fong, J. (2019). C-type natriuretic peptide analogue therapy in children with achondroplasia. *N Engl J Med, 381*(1), 25-35. doi:10.1056/NEJMoa1813446

Savarirayan, R., Tofts, L., Irving, M., Wilcox, W., Bacino, C. A., Hoover-Fong, J., … Day, J. (2020). Once-daily, subcutaneous vosoritide therapy in children with achondroplasia: a randomised, double-blind, phase 3, placebo-controlled, multicentre trial. *Lancet, 396*(10252), 684-692. doi:10.1016/S0140-6736(20)31541-5

Schievink, B., Kropelin, T., Mulder, S., Parving, H. H., Remuzzi, G., Dwyer, J., … Lambers Heerspink, H. J. (2016). Early renin-angiotensin system intervention is more beneficial than late intervention in delaying end-stage renal disease in patients with type 2 diabetes. *Diabetes Obes Metab, 18*(1), 64-71. doi:10.1111/dom.12583

Schindelin, J., Arganda-Carreras, I., Frise, E., Kaynig, V., Longair, M., Pietzsch, T., … Cardona, A. (2012). Fiji: an open-source platform for biological-image analysis. *Nat Methods, 9*(7), 676-682. doi:10.1038/nmeth.2019

Schinner, E., Wetzl, V., Schramm, A., Kees, F., Sandner, P., Stasch, J. P., … Schlossmann, J. (2017). Inhibition of the TGFbeta signalling pathway by cGMP and cGMP-dependent kinase I in renal fibrosis. *FEBS Open Bio, 7*(4), 550-561. doi:10.1002/2211-5463.12202

Schlossmann, J., & Schinner, E. (2012). cGMP becomes a drug target. *Naunyn Schmiedebergs Arch Pharmacol, 385*(3), 243-252. doi:10.1007/s00210-012-0730-6

Schmidt, H., Stonkute, A., Juttner, R., Koesling, D., Friebe, A., & Rathjen, F. G. (2009). C-type natriuretic peptide (CNP) is a bifurcation factor for sensory neurons. *Proc Natl Acad Sci U S A, 106*(39), 16847-16852. doi:10.1073/pnas.0906571106

Sefton, B. M. (2001). Labeling cultured cells with 32P(i) and preparing cell lysates for immunoprecipitation. *Curr Protoc Mol Biol, Chapter 18*, Unit 18 12. doi:10.1002/0471142727.mb1802s40

Serafini, P., Meckel, K., Kelso, M., Noonan, K., Califano, J., Koch, W., … Borrello, I. (2006). Phosphodiesterase-5 inhibition augments endogenous antitumor immunity by reducing myeloid-derived suppressor cell function. *J Exp Med, 203*(12), 2691-2702. doi:10.1084/jem.20061104

Sharman, S. K., Islam, B. N., Hou, Y., Singh, N., Berger, F. G., Sridhar, S., … Browning, D. D. (2018). Cyclic-GMP-elevating agents suppress polyposis in Apc(Min) mice by targeting the preneoplastic epithelium. *Cancer Prev Res (Phila), 11*(2), 81-92. doi:10.1158/1940-6207.CAPR-17-0267

Shea, C. M., Price, G. M., Liu, G., Sarno, R., Buys, E. S., Currie, M. G., & Masferrer, J. L. (2020). Soluble guanylate cyclase stimulator praliciguat attenuates inflammation, fibrosis, and end-organ damage in the Dahl model of cardiorenal failure. *Am J Physiol Renal Physiol, 318*(1), F148-F159. doi:10.1152/ajprenal.00247.2019

Shen, K., Johnson, D. W., & Gobe, G. C. (2016). The role of cGMP and its signaling pathways in kidney disease. *Am J Physiol Renal Physiol, 311*(4), F671-F681. doi:10.1152/ajprenal.00042.2016

Shi, L. Z., Goswami, S., Fu, T., Guan, B., Chen, J., Xiong, L., … Sharma, P. (2019). Blockade of CTLA-4 and PD-1 enhances adoptive T-cell therapy efficacy in an ICOS-mediated manner. *Cancer Immunol Res, 7*(11), 1803-1812. doi:10.1158/2326-6066.CIR-18-0873

Silbernagl, S. (2005). Die Funktion der Nieren. In R. Klinke, H.-C. Pape, & S. Silbernagl (Eds.), *Physiologie*, (pp. 326-376): Georg Thieme Verlag.

Sinha, N., & Dabla, P. K. (2015). Oxidative stress and antioxidants in hypertension-a current review. *Curr Hypertens Rev, 11*(2), 132-142. doi:10.2174/1573402111666150529130922

Snippert, H. J., van der Flier, L. G., Sato, T., van Es, J. H., van den Born, M., Kroon-Veenboer, C., … Clevers, H. (2010). Intestinal crypt homeostasis results from neutral competition between symmetrically dividing Lgr5 stem cells. *Cell, 143*(1), 134-144. doi:10.1016/j.cell.2010.09.016

Sorensen, I., Adams, R. H., & Gossler, A. (2009). DLL1-mediated Notch activation regulates endothelial identity in mouse fetal arteries. *Blood, 113*(22), 5680-5688. doi:10.1182/blood-2008-08-174508

Stasch, J. P., Becker, E. M., Alonso-Alija, C., Apeler, H., Dembowsky, K., Feurer, A., … Schramm, M. (2001). NO-independent regulatory site on soluble guanylate cyclase. *Nature, 410*(6825), 212-215. doi:10.1038/35065611

Stasch, J. P., Schmidt, P., Alonso-Alija, C., Apeler, H., Dembowsky, K., Haerter, M., … Wunder, F. (2002). NO- and haem-independent activation of soluble guanylyl cyclase: molecular basis and cardiovascular implications of a new pharmacological principle. *Br J Pharmacol, 136*(5), 773-783. doi:10.1038/sj.bjp.0704778

Stasch, J. P., Schmidt, P. M., Nedvetsky, P. I., Nedvetskaya, T. Y., H, S. A., Meurer, S., … Schmidt, H. H. (2006). Targeting the heme-oxidized nitric oxide receptor for selective vasodilatation of diseased blood vessels. *J Clin Invest, 116*(9), 2552-2561. doi:10.1172/JCI28371

Stehle, D., Xu, M. Z., Schomber, T., Hahn, M. G., Schweda, F., Feil, S., … Benardeau, A. (2021). Novel sGC activators increase glomerular cGMP, induce vasodilation, and improve blood flow in the murine kidney. *Br J Pharmacol, 10.1111/bph.15586*, 1-14. doi:10.1111/bph.15586

Stout, M. B., Scalzo, R. L., & Wellberg, E. A. (2021). Persistent metabolic effects of tamoxifen: considerations for an experimental tool and clinical breast cancer treatment. *Endocrinology, 162*(9)doi:10.1210/endocr/bqab126

Su, H., Wan, C., Song, A., Qiu, Y., Xiong, W., & Zhang, C. (2019). Oxidative stress and renal fibrosis: mechanisms and therapies. *Adv Exp Med Biol, 1165*, 585-604. doi:10.1007/978-981-13-8871-2_29

Sugiyama, S., Yoshida, A., Hieshima, K., Kurinami, N., Jinnouchi, K., Tanaka, M., … Jinnouchi, H. (2020). Initial acute decline in estimated glomerular filtration rate after sodium-glucose cotransporter-2 Inhibitor in patients with chronic kidney disease. *J Clin Med Res, 12*(11), 724-733. doi:10.14740/jocmr4351

Sun, Y., Chen, W., Torphy, R. J., Yao, S., Zhu, G., Lin, R., … Zhu, Y. (2021). Blockade of the CD93 pathway normalizes tumor vasculature to facilitate drug delivery and immunotherapy. *Sci Transl Med, 13*(604)doi:10.1126/scitranslmed.abc8922

Surmeli, N. B., & Marletta, M. A. (2012). Insight into the rescue of oxidized soluble guanylate cyclase by the activator cinaciguat. *Chembiochem, 13*(7), 977-981. doi:10.1002/cbic.201100809

Szalat, A., Perlman, A., Muszkat, M., Khamaisi, M., Abassi, Z., & Heyman, S. N. (2018). Can SGLT2 inhibitors cause acute renal failure? Plausible role for altered glomerular hemodynamics and medullary hypoxia. *Drug Saf, 41*(3), 239-252. doi:10.1007/s40264-017-0602-6

Ter-Avetisyan, G., Rathjen, F. G., & Schmidt, H. (2014). Bifurcation of axons from cranial sensory neurons is disabled in the absence of Npr2-induced cGMP signaling. *J Neurosci, 34*(3), 737-747. doi:10.1523/JNEUROSCI.4183-13.2014

The American Cancer Society (2019). Melanoma skin cancer stages. Available from https://www.cancer.org/cancer/melanoma-skin-cancer/detection-diagnosis-staging/melanoma-skin-cancer-stages.html (accessed 21 June 2021)

Theilig, F., Bostanjoglo, M., Pavenstadt, H., Grupp, C., Holland, G., Slosarek, I., … Bachmann, S. (2001). Cellular distribution and function of soluble guanylyl cyclase in rat kidney and liver. *J Am Soc Nephrol, 12*(11), 2209-2220. doi:10.1681/ASN.V12112209

Thunemann, M., Fomin, N., Krawutschke, C., Russwurm, M., & Feil, R. (2013). Visualization of cGMP with cGi biosensors. *Methods Mol Biol, 1020*, 89-120. doi:10.1007/978-1-62703-459-3_6

Thunemann, M., Wen, L., Hillenbrand, M., Vachaviolos, A., Feil, S., Ott, T., … Feil, R. (2013). Transgenic mice for cGMP imaging. *Circ Res, 113*(4), 365-371. doi:10.1161/CIRCRESAHA.113.301063

Tian, X., & Zhou, B. (2021). Strategies for site-specific recombination with high efficiency and precise spatiotemporal resolution. *J Biol Chem, 296*, 100509. doi:10.1016/j.jbc.2021.100509

Tikoo, S., Jain, R., Tomasetig, F., On, K., Martinez, B., Heu, C., … Weninger, W. (2021). Amelanotic B16-F10 melanoma compatible with advanced three-dimensional imaging modalities. *J Invest Dermatol, 141*(8), 2090-2094. doi:10.1016/j.jid.2021.01.025

Tobin, D. J. (2011). The anatomy and physiology of the skin. In M. J. Hertenstein & S. J. Weiss (Eds.), *The Handbook of Touch*, (pp. 3-32): Springer Publishing Co Inc.

Tobin, J. V., Zimmer, D. P., Shea, C., Germano, P., Bernier, S. G., Liu, G., … Masferrer, J. L. (2018). Pharmacological characterization of IW-1973, a novel soluble guanylate cyclase stimulator with extensive tissue distribution, antihypertensive, anti-inflammatory, and antifibrotic effects in preclinical models of disease. *J Pharmacol Exp Ther, 365*(3), 664-675. doi:10.1124/jpet.117.247429

Topalian, S. L., Drake, C. G., & Pardoll, D. M. (2015). Immune checkpoint blockade: a common denominator approach to cancer therapy. *Cancer Cell, 27*(4), 450-461. doi:10.1016/j.ccell.2015.03.001

Towbin, H., Staehelin, T., & Gordon, J. (1979). Electrophoretic transfer of proteins from polyacrylamide gels to nitrocellulose sheets: procedure and some applications. *Proc Natl Acad Sci U S A, 76*(9), 4350-4354. doi:10.1073/pnas.76.9.4350

Umansky, V., & Sevko, A. (2012). Melanoma-induced immunosuppression and its neutralization. *Semin Cancer Biol, 22*(4), 319-326. doi:10.1016/j.semcancer.2012.02.003

Vallon, V., & Thomson, S. C. (2017). Targeting renal glucose reabsorption to treat hyperglycaemia: the pleiotropic effects of SGLT2 inhibition. *Diabetologia, 60*(2), 215-225. doi:10.1007/s00125-016-4157-3

Valtcheva, N., Nestorov, P., Beck, A., Russwurm, M., Hillenbrand, M., Weinmeister, P., & Feil, R. (2009). The commonly used cGMP-dependent protein kinase type I (cGKI) inhibitor Rp-8-Br-PET-cGMPS can activate cGKI in vitro and in intact cells. *J Biol Chem, 284*(1), 556-562. doi:10.1074/jbc.M806161200

Vasudev, N. S., & Reynolds, A. R. (2014). Anti-angiogenic therapy for cancer: current progress, unresolved questions and future directions. *Angiogenesis, 17*(3), 471-494. doi:10.1007/s10456-014-9420-y

Venus, M., Waterman, J., & McNab, I. (2011). Basic physiology of the skin. *Surgery (Oxford), 29*(10), 471-474. doi:10.1016/j.mpsur.2011.06.010

Vermeersch, P., Buys, E., Sips, P., Pokreisz, P., Marsboom, G., Gillijns, H., … Janssens, S. (2009). Gender-specific modulation of the response to arterial injury by soluble guanylate cyclase alpha1. *Open Cardiovasc Med J, 3*, 98-104. doi:10.2174/1874192400903010098

Versmissen, J., Mirabito Colafella, K. M., Koolen, S. L. W., & Danser, A. H. J. (2019). Vascular cardio-oncology: vascular endothelial growth factor inhibitors and hypertension. *Cardiovasc Res, 115*(5), 904-914. doi:10.1093/cvr/cvz022

Vinay, D. S., Ryan, E. P., Pawelec, G., Talib, W. H., Stagg, J., Elkord, E., … Kwon, B. S. (2015). Immune evasion in cancer: Mechanistic basis and therapeutic strategies. *Semin Cancer Biol, 35 Suppl*, S185-S198. doi:10.1016/j.semcancer.2015.03.004

Vogelstein, B., & Kinzler, K. W. (1993). The multistep nature of cancer. *Trends in Genetics, 9*(4), 138-141. doi:10.1016/0168-9525(93)90209-Z

Weidmann, P., Hasler, L., Gnadinger, M. P., Lang, R. E., Uehlinger, D. E., Shaw, S., … Reubi, F. C. (1986). Blood levels and renal effects of atrial natriuretic peptide in normal man. *J Clin Invest, 77*(3), 734-742. doi:10.1172/JCI112368

Weinmeister, P., Lukowski, R., Linder, S., Traidl-Hoffmann, C., Hengst, L., Hofmann, F., & Feil, R. (2008). Cyclic guanosine monophosphate-dependent protein kinase I promotes adhesion of primary vascular smooth muscle cells. *Mol Biol Cell, 19*(10), 4434-4441. doi:10.1091/mbc.E08-04-0370

Wendling, O., Bornert, J. M., Chambon, P., & Metzger, D. (2009). Efficient temporally-controlled targeted mutagenesis in smooth muscle cells of the adult mouse. *Genesis, 47*(1), 14-18. doi:10.1002/dvg.20448

Wennysia, I. C., Zhao, L., Schomber, T., Braun, D., Golz, S., Summer, H., … Patzak, A. (2021). Role of soluble guanylyl cyclase in renal afferent and efferent arterioles. *Am J Physiol Renal Physiol, 320*(2), F193-F202. doi:10.1152/ajprenal.00272.2020

Wolfsgruber, W., Feil, S., Brummer, S., Kuppinger, O., Hofmann, F., & Feil, R. (2003). A proatherogenic role for cGMP-dependent protein kinase in vascular smooth muscle cells. *Proc Natl Acad Sci U S A, 100*(23), 13519-13524. doi:10.1073/pnas.1936024100

Yamahara, K., Itoh, H., Chun, T. H., Ogawa, Y., Yamashita, J., Sawada, N., … Nakao, K. (2003). Significance and therapeutic potential of the natriuretic peptides/cGMP/cGMP-dependent protein kinase pathway in vascular regeneration. *Proc Natl Acad Sci U S A, 100*(6), 3404-3409. doi:10.1073/pnas.0538059100

Yamazaki, N., Uhara, H., Fukushima, S., Uchi, H., Shibagaki, N., Kiyohara, Y., … Tokudome, T. (2015). Phase II study of the immune-checkpoint inhibitor ipilimumab plus dacarbazine in Japanese patients with previously untreated, unresectable or metastatic melanoma. *Cancer Chemother Pharmacol, 76*(5), 969-975. doi:10.1007/s00280-015-2870-0

Yoshihara, F., Tokudome, T., Kishimoto, I., Otani, K., Kuwabara, A., Horio, T., … Kangawa, K. (2015). Aggravated renal tubular damage and interstitial fibrosis in mice lacking guanylyl cyclase-A (GC-A), a receptor for atrial and B-type natriuretic peptides. *Clin Exp Nephrol, 19*(2), 197-207. doi:10.1007/s10157-014-0982-1

Zahreddine, R., Davezac, M., Smirnova, N., Buscato, M., Lhuillier, E., Lupieri, A., … Fontaine, C. (2020). Tamoxifen accelerates endothelial healing by targeting ERalpha in smooth muscle cells. *Circ Res, 127*(12), 1473-1487. doi:10.1161/CIRCRESAHA.120.317062

Zeiser, R., Andrlova, H., & Meiss, F. (2018). Trametinib (GSK1120212). *Recent Results Cancer Res, 211*, 91-100. doi:10.1007/978-3-319-91442-8_7

Zhang, J. Q. J., Saravanabavan, S., Cheng, K. M., Raghubanshi, A., Chandra, A. N., Munt, A., … Rangan, G. K. (2021). Long-term dietary nitrate supplementation does not reduce renal cyst growth in experimental autosomal dominant polycystic kidney disease. *PLoS One, 16*(4), e0248400. doi:10.1371/journal.pone.0248400

Zhao, L., Wang, B., Gomez, N. A., de Avila, J. M., Zhu, M. J., & Du, M. (2020). Even a low dose of tamoxifen profoundly induces adipose tissue browning in female mice. *Int J Obes (Lond), 44*(1), 226-234. doi:10.1038/s41366-019-0330-3

Zhao, Y., Brandish, P. E., Di Valentin, M., Schelvis, J. P., Babcock, G. T., & Marletta, M. A. (2000). Inhibition of soluble guanylate cyclase by ODQ. *Biochemistry, 39*(35), 10848-10854. doi:10.1021/bi9929296

Zhu, X., Hill, R. A., Dietrich, D., Komitova, M., Suzuki, R., & Nishiyama, A. (2011). Age-dependent fate and lineage restriction of single NG2 cells. *Development, 138*(4), 745-753. doi:10.1242/dev.047951

6 Publications by the author

The presented work has contributed to the following publications:

Stehle, D., Schulz, J., Stotz, A., Glöckner, H., Kaesler, S., Feil, S., Schmidt, H., & Feil, R. In situ cGMP imaging uncovers the role of NO/NO-GC/cGMP signaling in the melanoma microenvironment. *In preparation*.

Stehle, D., Xu, M. Z., Schomber, T., Hahn, M. G., Schweda, F., Feil, S., Kraehling, J. R., Eitner, F., Patzak, A., Sandner, P., Feil, R., & Benardeau, A. (2021). Novel sGC activators increase glomerular cGMP, induce vasodilation, and improve blood flow in the murine kidney. *Br J Pharmacol, 10.1111/bph.15586*, 1-14. doi:10.1111/bph.15586

Feil, R., Lehners, M., **Stehle, D.**, & Feil, S. (2021). Visualising and understanding cGMP signals in the cardiovascular system. *Br J Pharmacol, 10.1111/bph.15500*, 1-19. doi:10.1111/bph.15500

Tikoo, S., Jain, R., Tomasetig, F., On, K., Martinez, B., Heu, C., **Stehle, D.**, Obeidy, P., Guo, D., Vincent, J. N., Cook, A. J. L., Roediger, B., Feil, R., Whan, R. M., & Weninger, W. (2021). Amelanotic B16-F10 melanoma compatible with advanced three-dimensional imaging modalities. *J Invest Dermatol, 141*(8), 2090-2094. doi:10.1016/j.jid.2021.01.025

Zhang, Y., Benz, P., **Stehle, D.**, Yang, S., Kurz, H., Feil, S., Nagel, G., Feil, R., Gao, S., & Bender, M. (2021). Optogenetic manipulation of cGMP highlights PDE5 as the predominant cGMP-hydrolyzing PDE in megakaryocytes. *bioRxiv*, 2021.2011.2012.468375. doi:10.1101/2021.11.12.468375

In addition, the author has contributed to the following unrelated publications:

Stehle, D., Grimm, M., Einsele-Scholz, S., Ladwig, F., Johanning, J., Fischer, G., Gillissen, B., Schulze-Osthoff, K., & Essmann, F. (2018). Contribution of BH3-domain and Transmembrane-domain to the Activity and Interaction of the Pore-forming Bcl-2 Proteins Bok, Bak, and Bax. *Sci Rep, 8*(1), 12434. doi:10.1038/s41598-018-30603-6

Einsele-Scholz, S., Malmsheimer, S., Bertram, K., **Stehle, D.**, Johanning, J., Manz, M., Daniel, P. T., Gillissen, B. F., Schulze-Osthoff, K., & Essmann, F. (2016). Bok is a genuine multi-BH-domain protein that triggers apoptosis in the absence of Bax and Bak. *J Cell Sci, 129*(11), 2213-2223. doi:10.1242/jcs.181727

The author has also presented his work on the following conferences:

Stehle, D., Stotz, A., Schulz, J., & Feil, R. (2022). Heterogeneity and therapeutic potential of cGMP signaling in melanoma cells and the tumor microenvironment. In *10th International Conference on cGMP Generators, Effectors and Therapeutic Implications*. Augsburg, Germany.

Stehle, D., Schulz, J., Fukumura, D., & Feil, R. (2021). NO-GC in the tumour microenvironment represents a potential drug target for melanoma treatment. In *The 1st PhD Student Conference of the GRK 2381 on Cancer, Cardiovascular diseases & Neurological disorders*. Tübingen, Germany.

Stehle, D., Lehners, M., Feil, S., & Feil, R. (2020). *In situ* cGMP imaging reveals NO-GC as a potential drug target for melanoma treatment. In *5th German Pharm-Tox Summit*. Leipzig, Germany.

Stehle, D., Feil, S., & Bénardeau, A. (2019). Real-time cGMP imaging reveals the spatiotemporal activity of sGC modulators in the kidney. In *4th German Pharm-Tox Summit*. Stuttgart, Germany.

Bénardeau, A., **Stehle, D.**, Feil, R., Patzak, A., Griffin, K., Bidani, A., Sandner, P., & Eitner, F. (2019). sGC activator (sGCact) effects in kidney pathophysiology. In *9th International Conference on cGMP Generators, Effectors and Therapeutic Implications*. Mainz, Germany.

Stehle, D., & Feil, R. (2019). Novel imaging techniques to study the role of cGMP in cancer progression. In *High-resoluation imaging of cells and molecules*. Mosbach, Germany.

Stehle, D., & Feil, R. (2018). Novel imaging tools to study the role of cGMP in melanoma. In *Imaging of Cancer Dynamics*. Turin, Italy.

Supplement

Table S1: Brand names with their related companies and headquarters.

Brand name	Company and headquarter
A. Hartenstein	A. Hartenstein GmbH, Würzburg, Germany
abcam	Abcam plc, Cambridge, MA, USA
abs-online	abtibodies-online GmbH, Aachen, Germany
Applichem	AppliChem GmbH, Darmstadt, Germany
Axxora	Enzo Biochem Inc., Farmingdale, NY, USA
B. Braun	B. Braun Melsungen AG, Melsungen, Germany
Bayer	Bayer AG, Wuppertal, Germany
BD Pharmingen	Becton, Dickinson and Company, San Jose, CA, USA
BiOLOG	Biolog Inc., Hayward, CA, USA
BIOLOGIX	Biologix Group Ltd., Jinan, Shandong, China
Biometra	Analytik Jena AG, Jena, Germany
Bio-Rad	Bio-Rad Laboratories Inc., Hercules, CA, USA
BIORON	BIORON GmbH, Römerberg, Germany
Biozym	Biozym Scientific GmbH, Hessisch Oldendorf, Germany
Cell Signaling	Cell Signaling Technology Inc., Danvers, MA, USA
charles river	Charles River Laboratories International Inc., Wilmington, MA, USA
CHEMSOLUTE	Th. Geyer GmbH & Co. KG, Renningen, Germany
CHROMA	Chroma Technology Corp., Bellows Falls, VT, USA
cp-pharma	CP-Pharma GmbH, Burgdorf, Germany
Eickemeyer	Eickemeyer – Medizintechnik für Tierärzte KG, Tuttlingen, Germany
Eppendorf	Eppendorf AG, Hamburg, Germany
eurofins	Eurofins Scientific SE, Luxembourg, Luxembourg
F·S·T	Fine Science Tools Inc., Foster City, CA, USA
Fisher	Thermo Fisher Scientific Inc., Waltham, MA, USA
GE Healthcare	General Electric Corp., Chicago, IL, USA
GENAXXON	GENAXXON bioscience GmbH, Ulm, Germany
GIBCO	Thermo Fisher Scientific Inc., Waltham, MA, USA
Honeywell	Honeywell International Inc., Charlotte, NC, USA
invitrogen	Thermo Fisher Scientific Inc., Waltham, MA, USA
Jackson	Jackson ImmunoResearch Europe Ltd, Ely, UK
KNF Neuberger	KNF Neuberger GmbH, Freiburg im Breisgau, Germany
Kodak	Eastman Kodak Co., Rochester, NY, USA
Leica	Leica Biosystems GmbH, Wetzlar, Germany
MARIENFELD	Paul Marienfeld GmbH & Co. KG, Lauda-Königshofen, Germany
Mast	Hans Mast GmbH, Tübingen, Germany
memmert	Memmert GmbH + Co. KG, Schwabach, Germany
Merck	Merck KGaA, Darmstadt, Germany
MICROM	PHC Holding Corp., Dreieich, Germany
Microsoft	Microsoft Corp., Redmond, WA, USA
Millipore	Merck KGaA, Burlington, MA, USA
MP Biomedicals	MP Biomedicals LLC, Santa Ana, CA, USA
NEB	New England Biolabs Inc., Ipswich, MA, USA
neoLab	neoLab Migge GmbH, Heidelberg, Germany
NIPPON Genetics	Nippon Genetics Co. Ltd., Bunkyo-ku, Tokyo, Japan
OriginLab	OriginLab Corp., Northampton, MA, USA
Pattex	Henkel AG & KGaA, Düsseldorf, Germany
PEQLAB	Avantor Inc., Radnor, PA, USA
Photometrics	Teledyne Photometrics Inc., Tucson, AZ, USA

Brand name	Company and headquarter
QImaging	QImaging Corp., Surrey, BC, Canada
R&D Systems	Bio-Techne Corp., Minneapolis, MN, USA
Roche	F. Hoffmann-La Roche AG, Basel, Switzerland
Roth	Carl Roth GmbH + Co. KG, Karlsruhe, Germany
Sakura	Sakura Finetek Japan Co. Ltd, Koto-Ku, Tokyo, Japan
Santa Cruz	Santa Cruz Biotechnology Inc., Dallas, TX, USA
SARTORIUS	Sartorius AG, Göttingen, Germany
Sigma-Aldrich	Merck KGaA, Burlington, MA, USA
SONY	Sony Group Corp., Minato, Tokyo, Japan
SPOT Imaging	Diagnostic Instruments Inc., Sterling Heights, MI, USA
ssniff	ssniff Spezialdiäten GmbH, Soest, Germany
Systec	Systec GmbH, Nürnberg, Germany
Thermo	Thermo Fisher Scientific Inc., Waltham, MA, USA
THOMY	Nestlé S.A., Vevey, Switzerland
TILL Photonics	TILL Photonics GmbH, Gräfeling, Germany
Tocris	Bio-Techne Corp., Minneapolis, MN, USA
Vector Labs	Vector Laboratories Inc., Burlingame, CA, USA
Veet	Reckitt Benckiser Group plc, Slough, UK
Visitron	Visitron Systems GmbH, Puchheim, Germany
Warner Instruments	Harvard Bioscience Inc., Hamden, CT, USA
YOKOGAWA	Yokogawa Electric Corp., Musashino, Tokyo, Japan
ZEISS	Carl Zeiss AG, Oberkochen, Germany

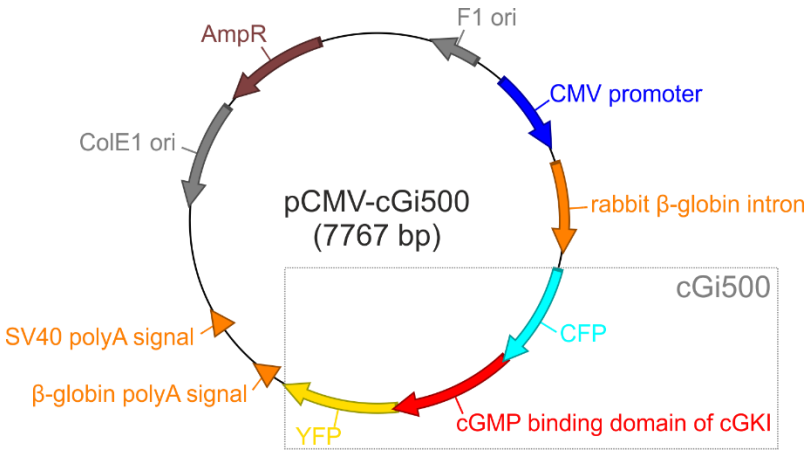

Figure S1: Vector card of pCMV-cGi500. The pCMV-cGi500 vector contains a gene encoding the cGMP sensor cGi500 (gray box), which consists of CFP (cyan) and YFP (yellow) linked by the tandem cGMP binding domain of bovine cGKI (red). cGi500 gene expression is controlled by the strong ubiquitous cytomegalovirus (CMV) promoter (blue), as well as a rabbit β-globin intron and polyadenylation (polyA) signals from SV40 and β-globin (orange). ColE1 and F1 origins of replication (ori; gray) as well as an ampicillin resistance gene (AmpR; brown) allow plasmid amplification in bacterial hosts.

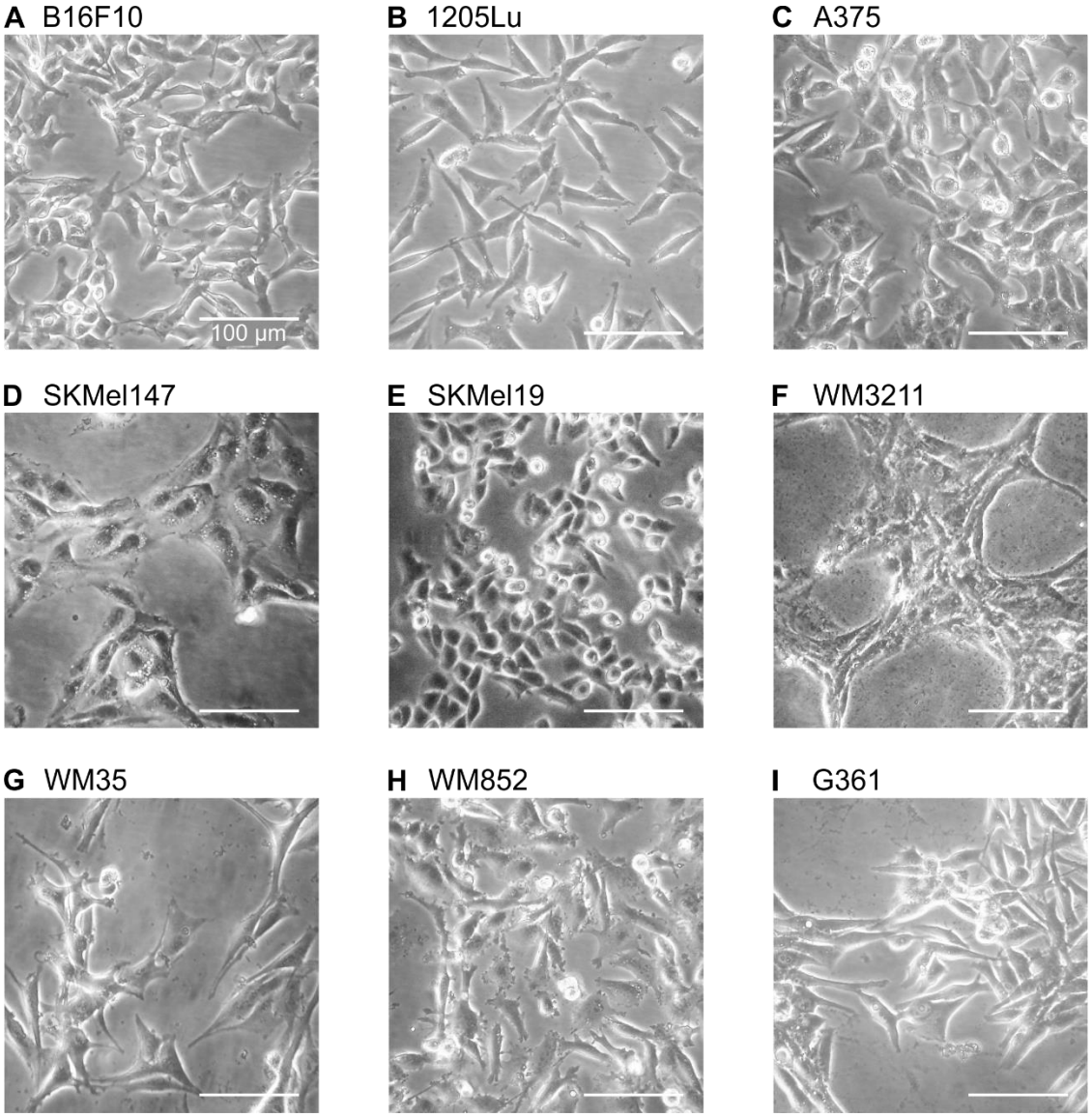

Figure S2: Phase contrast pictures of the melanoma cell lines characterized herein. Melanoma cells were thawed and cultured as described in 2.2. Every two days, cells either received fresh medium (≤ 50 % confluence) or were passaged in the following splitting ratios: **(A)** B16F10, 1/10 to 1/15; **(B)** 1205Lu, 1/3 to 1/6; **(C)** A375, 1/9 to 1/12; **(D)** SKMel147, 1/5; **(E)** SKMel19, 1/5; **(F)** WM3211, 1/3; **(G)** WM35, 1/3; **(H)** WM852, 1/3; **(I)** G361, 1/3. Shown are phase contrast pictures that were taken every few weeks before passaging. Pictures are representative for n ≥ 2 independent cell cultures. Scale bars, 100 µm.

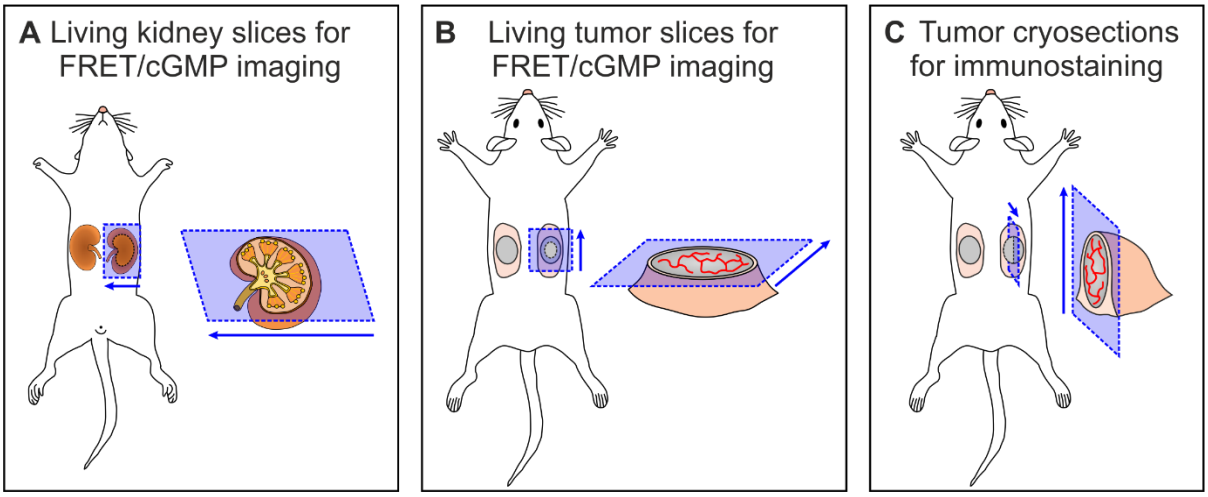

Figure S3: Cutting planes of tissue sections in the present study. Shown are the cutting planes (transparent blue rectangles) for the preparation of **(A)** acute kidney slices (2.5.2.1), **(B)** acute tumor slices (2.5.2.2), and **(C)** tumor cryosections (2.7.1) in relation to the whole mice as well as the respective tissues. Blue arrows indicate the cutting direction.

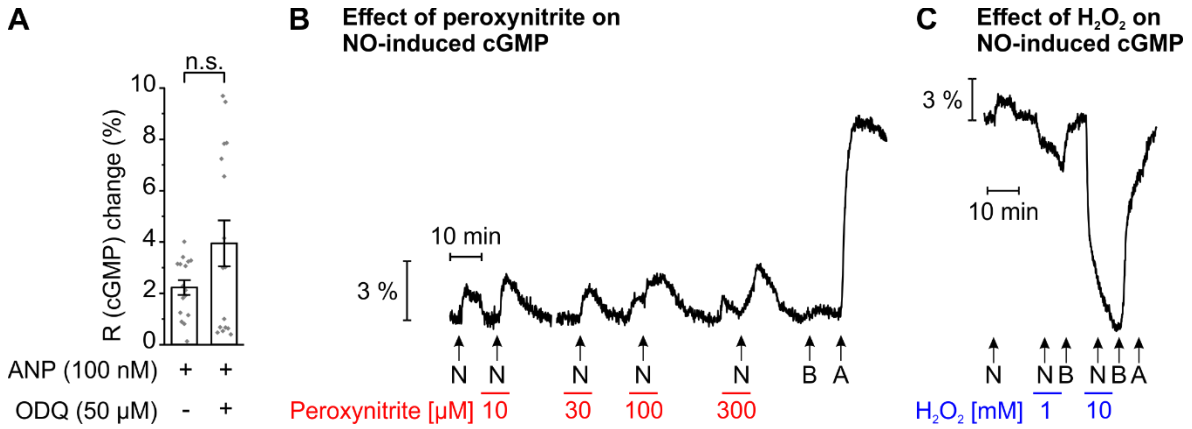

Figure S4: Effect of different oxidizing agents on NO- and ANP-induced cGMP generation in glomeruli. FRET-based cGMP imaging was performed in glomeruli of kidney slices from cGi-L1 mice. **(A)** During the measurements, slices were superfused with ANP (100 nM) for 2 min, either with or without 5 min pre-incubation with ODQ (50 µM). Statistical analysis was performed with the relative R (cGMP) change of cGMP signals. Data represent mean ± SEM (n ≥ 16 glomeruli in ≥ 5 kidney slices from ≥ 2 mice). **(B)** Representative measurement of a glomerulus with peroxynitrite application. During the recording, DEA/NO (N; 10 µM), BAY-543 (B; 10 µM), or ANP (A; 100 nM) were applied to the slices for 2 min with or without 5 min pre-incubation with peroxynitrite in the indicated concentrations. Black trace represents R (cGMP), which indicates cGMP concentration changes. **(C)** Representative measurement of a glomerulus with H_2O_2 application. Similarly, DEA/NO (N; 10 µM), BAY-543 (B; 10 µM), or ANP (A; 100 nM) were applied to the slices for 2 min with or without 5 min pre-incubation with H_2O_2 in the indicated concentrations. Graphs are representative for 3 independent experiments. Part of these results was published in Stehle et al. (2021).

Figure S5: PDE5 inhibition amplifies CNP-induced cGMP increases in both melanin-producing and amelanotic B16F10 cells. Different melanin-producing and amelanotic B16F10 clones were compared with regard to cGMP-induced VASP (Ser239) phosphorylation. Cultured **(A)** B16F10, **(B)** B16F10-R, **(C)** B16F10-A and **(D)** B16F10-AR were incubated for 10 min at 37 °C and 6 % CO_2 with the cell-permeable cGMP analog 8-Br-cGMP (100 µM), CNP (100 nM, if not specified) or the PDE5 inhibitors sildenafil (30 µM) or tadalafil (100 nM), before protein was extracted. Protein was analyzed via SDS-PAGE followed by Western Blot. Immunostaining for phospho(Ser239)-VASP (p-VASP) and GAPDH (as reference protein) was performed. Graphs are representative for n = 2 Western Blots. cG, 8-Br-cGMP; C, CNP; PDE5i, PDE5 inhibitor; SIL, sildenafil; TAD, tadalafil. Note that for reasons of clarity, some columns are duplicated from **Figure 4D**.

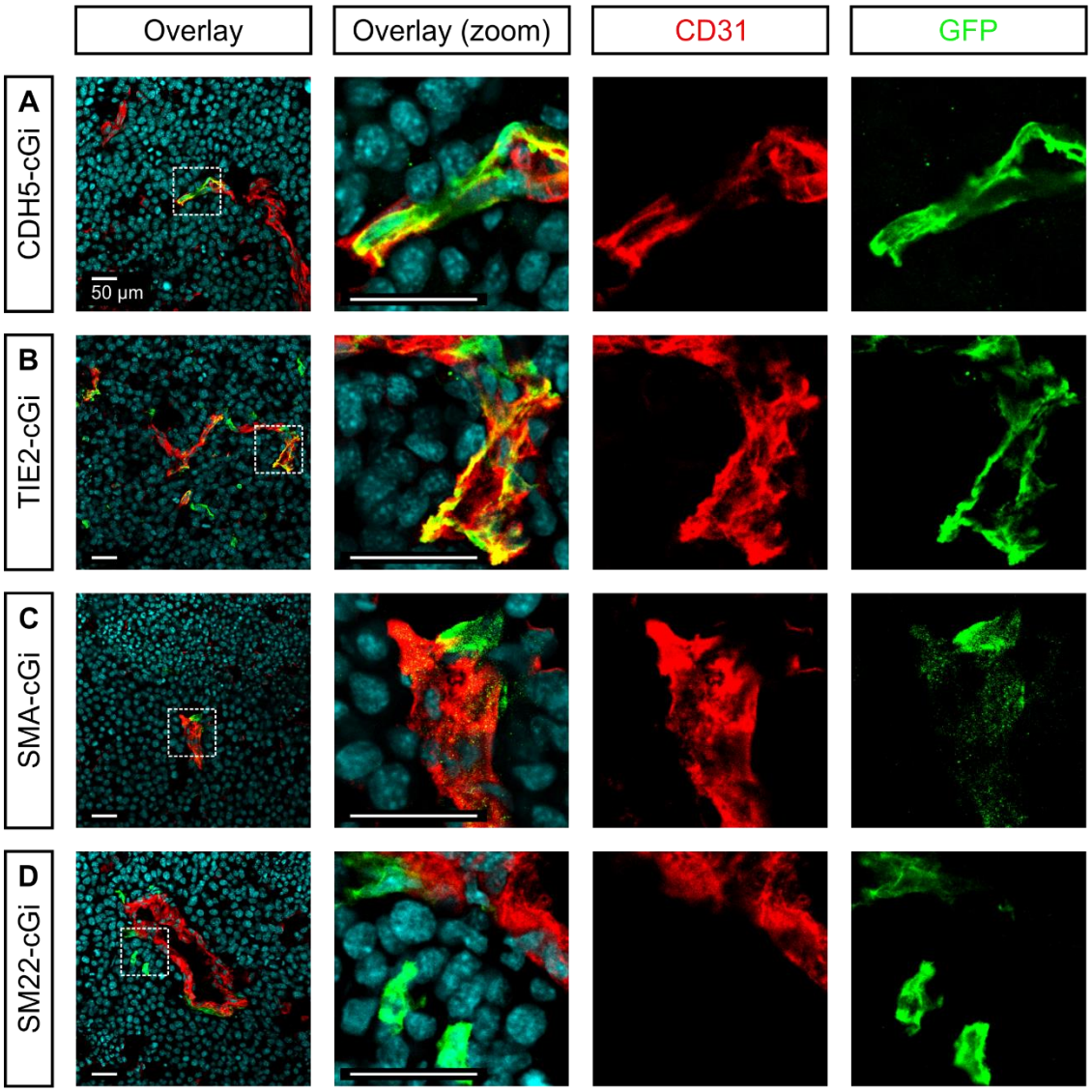

Figure S6: IF staining demonstrates recombination in the endothelium of tumor blood vessels of TIE2-cGi and CDH5-cGi mice. B16F10-A cells were administered by intradermal injection into **(A)** endothelial cell-specific CDH5-cGi or **(B)** TIE2-cGi mice, or into **(C)** smooth muscle/pericyte-specific SMA-cGi or **(D)** SM22-cGi mice. The tumors were allowed to grow for 10-14 days. Experimental animals were sacrificed and the tumors were dissected, fixed and cryosectioned. Frozen sections were stained via IF for the cGMP sensor (using an α-GFP antibody) and for CD31 as endothelial marker protein. CDH5- and TIE2-cGi-positive cells as expected co-expressed the endothelial marker CD31. In contrast, SMA- and SM22-cGi-positive cells were found in close proximity to the CD31-positive endothelium, but the staining did not overlap. Note that cytosolic proteins (i.e., cGi500 (GFP), SMA and SM22) and membrane proteins (i.e., CD31, CDH5 and TIE2) have different subcellular distributions. Graphs are representative for 3 tumors dissected from 3 mice. Scale bars, 50 µm.

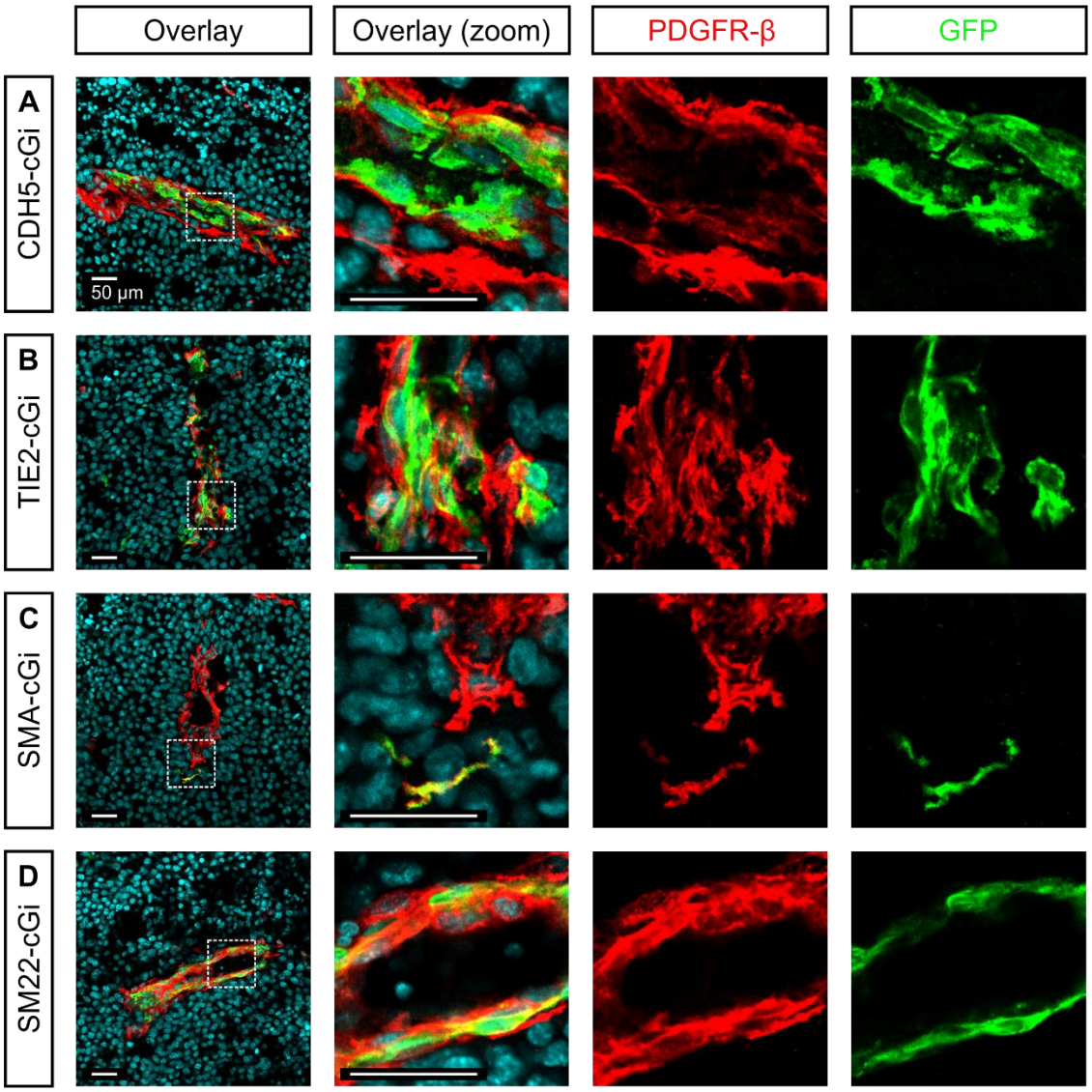

Figure S7: IF staining demonstrates recombination in tumor pericytes of SMA-cGi and SM22-cGi mice. B16F10-A cells were administered by intradermal injection into **(A)** endothelial cell-specific CDH5-cGi or **(B)** TIE2-cGi mice, or into **(C)** smooth muscle/pericyte-specific SMA-cGi or **(D)** SM22-cGi mice. Tumors were allowed to grow for 10-14 days. Experimental animals were sacrificed and the tumors were dissected, fixed and cryosectioned. Frozen sections were stained via IF for the cGMP sensor (using an α-GFP antibody) and for PDGFR-β as pericyte marker protein. A subpopulation of the PDGFR-β-positive cells was found to be recombined in SMA- and SM22-cGi mice. In contrast, CDH5- and TIE2-cGi-positive cells were found in close proximity to PDGFR-β-expressing pericytes, but the staining did not overlap. Note that cytosolic proteins (i.e., cGi500 (GFP), SMA and SM22) and membrane proteins (i.e., CD31, CDH5 and TIE2) have different subcellular distributions. Graphs are representative for 3 tumors dissected from 3 mice. Scale bars, 50 µm.

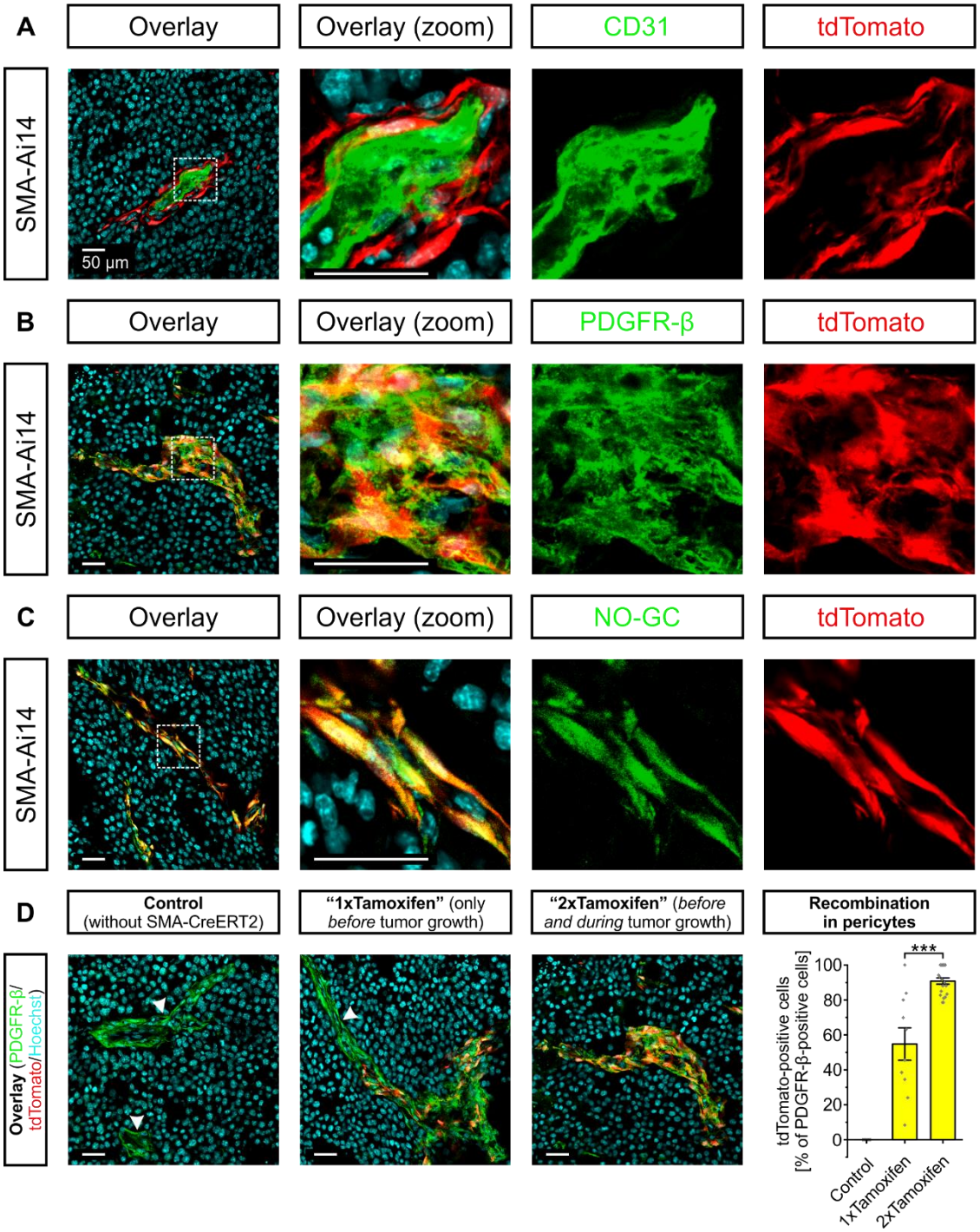

Figure S8: SMA-CreERT2-mediated recombination efficiently covers NO-GC- and PDGFR-β-positive tumor pericytes. B16F10-A cells were administered by intradermal injection into smooth muscle/pericyte-specific SMA-Ai14 mice. Tumors were allowed to grow for 10-14 days. Experimental animals were sacrificed and the tumors were dissected, fixed and cryosectioned. Frozen sections were stained for **(A)** CD31 as endothelial cell marker protein, **(B)** PDGFR-β as pericyte marker protein or **(C)** NO-GC. Immunostaining as well as tdTomato fluorescence caused by the Ai14-L2 transgene were detected by confocal microscopy. tdTomato was not co-expressed in CD31-positive endothelial cells, but in PDGFR-β- and NO-GC-positive pericytes. Note that cytosolic proteins (i.e., tdTomato and NO-GC) and membrane

proteins (i.e., CD31 and PDGFR-β) have different subcellular distributions. Graphs are representative for ≥ 2 tumors dissected from ≥ 2 mice. **(D)** Mice in the experiment were divided into three groups. The control group did not carry the SMA-CreERT2 transgene, one group of SMA-Ai14 mice only received tamoxifen before B16F10 cell injection ("1xTamoxifen"), and a second group of SMA-Ai14 mice received tamoxifen before and during tumor growth ("2xTamoxifen"; note that the latter treatment is identical to the treatment of SMA-cGi, NO-GCsmko and SMA-Ai14 mice in the other experiments described herein (**Figures 8, 9 and S8A**)). Frozen tumor sections were stained for PDGFR-β as pericyte marker. As expected, no recombination was found in the control group lacking the Cre enzyme. Furthermore, the efficiency of SMA-Ai14-mediated recombination appeared to be higher in 2xTamoxifen animals as compared to 1xTamoxifen animals. Arrowheads point towards vessel regions bare of recombination. Practically no recombined, tdTomato-positive cells were PDGFR-β-negative (1xTamoxifen: 0.6 % and 2xTamoxifen: 0.7 % of all tdTomato-positive cells). Cells co-expressing PDGFR-β and tdTomato were quantified, and the percentage of double-positive relative to all PDGFR-β-positive cells was used as an indicator for recombination efficiency (bar graph on the right). Data represent mean ± SEM (n ≥ 6 sections of ≥ 2 tumors dissected from ≥ 2 mice per group). Scale bars, 50 µm.

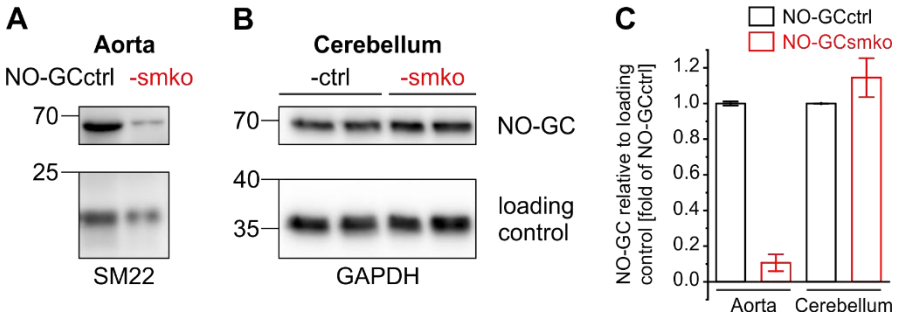

Figure S9: Western Blot confirms smooth muscle/pericyte-specific NO-GC depletion in NO-GCsmko mice. B16F10-A cells were administered by intradermal injection into cell type-specific cGMP sensor mice. The tumors were allowed to grow for 10-14 days. Experimental animals were sacrificed, **(A)** aorta (as VSMC-rich tissue) and **(B)** cerebellum (as tissue with high VSMC- and pericyte-unrelated NO-GC expression) were dissected, and protein was extracted from these tissues. Protein samples were analyzed via SDS-PAGE followed by Western Blot, and immunostaining of NO-GC as well as appropriate loading controls for the two tissues (aorta: SM22 and cerebellum: GAPDH) was performed. **(C)** Band intensities of NO-GC and the respective loading controls were quantified. In aorta samples of NO-GCsmko mice, NO-GC protein was markedly reduced. In contrast, the NO-GC content of cerebellum samples was not obviously affected by NO-GCsmko. Data represent mean ± minimum/maximum (n = 2 Western Blots).

Acknowledgments

First and foremost, I'd like to thank Prof. Dr. Robert Feil for the opportunity to perform my PhD in his laboratory, as well as for his and PD Dr. Hannes Schmidt's excellent supervision, advice and support during the process.

I am very grateful for all contributions to the presented work from inside and outside the laboratory. This includes the lab rotations of Katharina Hartman, Hannah Glöckner and Annemarie Stotz, who helped me with the analysis of melanoma cells and tissue sections. In addition, I want to highlight the support from Dr. Susanne Kaesler (Technische Universität München), Philipp Knopf and Dr. Manfred Kneiling (Werner Siemens Imaging Center, Tübingen), as well as Rohit Jain PhD, Shweta Tikoo PhD and Prof. Dr. Wolfgang Weninger (Centenary Institute, Sydney) with establishing the *ex vivo* and *in vivo* melanoma models.

Thank you, Dr. Peter Sandner and Dr. Agnès Bénardeau (Bayer), Prof. Dr. Andreas Friebe (Julius-Maximilians-Universität Würzburg), PD Dr. Hannes Schmidt (Eberhard Karls Universität Tübingen), as well as Dr. Tobias Sinnberg and Prof. Dr. Birgit Schittek (Universitätsklinikum Tübingen), for providing drugs, antibodies, cells and other materials.

Many thanks go to the past and present members of the Feil lab for all the work-related support, but also for the warm and pleasant working atmosphere as well as the numerous evening activities together. This especially applies to Michael Krämer and Moritz Lehners who helped me with experiments and lively discussions, to Maria T. Kristina Zaldivia PhD for proofreading the first draft, and to Barbara Birk for her technical assistance.

Thanks to Dr. Susanne Feil, Dr. Ulf Scheurlen (representative for the veterinary service of the Eberhard Karls Universität Tübingen), and all animal caretakers of the IFIB animal facility for their support with the *in vivo* experiments.

Last, I want to thank all my friends and family for making the PhD such a pleasant and joyful phase in my life. Thank you very much!